UNIVERSITY OF MIAMI

EXPERIMENTAL INVESTIGATIONS OF BASE DRAG REDUCTION USING PASSIVE JET FLOW CONTROL

By

William Bartow

A THESIS

Submitted to the Faculty
of the University of Miami
in partial fulfillment of the requirements for
the degree of Master of Science

Coral Gables, Florida

August 2014

UNIVERSITY OF MIAMI

A thesis submitted in partial fulfillment of
the requirements for the degree of
Master of Science

EXPERIMENTAL INVESTIGATIONS OF BASE DRAG REDUCTION USING PASSIVE JET FLOW CONTROL

William Bartow

Approved:

_____
Gecheng Zha, Ph.D.
Associate Professor of Mechanical
and Aerospace Engineering

_____
M. Brian Blake, Ph.D.
Dean of the Graduate School

_____
Na Li, Ph.D.
Assistant Professor of
Mechanical and Aerospace Engineering

_____
Wangda Zuo, Ph.D.
Assistant Professor of Civil, Architectural
and Environmental Engineering

BARTOW, WILLIAM (M.S., Mechanical Engineering)
Experimental of Base Drag Reduction (August 2014)
Using Passive Jet Flow Control.

Abstract of a thesis at the University of Miami.

Thesis supervised by Professor Gecheng Zha.
No. of pages in text. (118)

This study is focused on the experimental investigation of and extended rear view mirror and the development of near-wake flow in an effort to reduce the overall base pressure drag of the model. The passive flow control technique was employed through a circumferential slot of the rearward facing edge of a bluff body to deliver a passive jet in the direction of the free stream. The passive jet employs the surrounding high energy free stream air through an intake slot in the front of the model in order to enhance the mixing layer of the immediate wake region in addition to energizing the wake area flow through entrainment. These effects subsequently caused a reduction of the effects of adverse pressure gradients that are associated with separation of the free stream shear layer over the over the passive jet model surface. The jet produced along the rear surface not only increased the turbulence of the mixing layer, but can also be directly tied to the coherent nature of the wake area flow. Using Two Dimensional Two Component (2D2C) in addition to Two Dimensional Three component (2D3C) Particle Image Velocimetry applied to our model in an open circuit wind tunnel, results show a substantial reduction in the overall wake area for which we attribute to the enhancements due to mixing effects of the passive jet interacting with the free stream shear layer. Flow entrainment from enhanced vorticity through the production coherent structures are believed to initiate the

mixing layer earlier, in addition to increase the growth rate of the mixing layer while also attributing to the increase in the overall shear layer thickness as well. Particle Image Velocimetry (PIV) was carried out on an automobile mirror model with three configurations in order to investigate the effects of a baseline model including the absence of a passive jet mixing, a modified model including a small area circumferential jet and a heavily modified model including a large circumferential slot area jet. In combination with PIV, Partial Orthogonal Decomposition (POD) also referred to as the Karhunen Loeve expansion, was also applied in order to analyze the underlying large scale structures and dominant behaviors that would otherwise be hard to identify in the immediate wake flow structure.

The mirror models used for testing was designed and produced to provide three specific testing configurations, baseline, Jet 1 and Jet 2. In order to proceed with the testing of the mirror models, the design and manufacturing of a reinforced force balance mounting apparatus was necessary in order to provide a more rigid and secure platform to measure aerodynamic loads of the mirror and future designs. The nature of the new design includes multiple support location in order to more equally distribute the loading in addition to bearings to assist in experiments that require a rotation of the model in order to increase the angle with respect to the free steam flow.

Acknowledgment

I would like to express my deepest gratitude to my professor and advisor, Dr. Gecheng Zha for the guidance and direction throughout the course of my work.

I would like to thank my colleagues in the CFD and Wind Tunnel laboratories for all the assistance and guidance received as well as the machinists in the Engineering Machine Shop for the countless hours of guidance throughout my research.

For their unwavering love, support and patience, I would like to thank my family.

For all their love and encouragement throughout my research, I would like to thank my girlfriend, Lauren, and her family.

Contents

List of Figures

List of Tables

List of Symbols

α	Magnification factor
λ	Eigenvalues
ρ	Density
τ_ω	Surface Shear Stress
θ	Perspective Angle
ϕ	POD Modes
b	Eigen Vectors
C	Correlation Tensor
CCD	Charged Coupled Device
$I_1(x, y)$	Image Intensities of the 1st interrogation window
$I_2(x, y)$	Image Intensities of the 2nd interrogation window
L_r	Distance of reference imgae
l_r	Distance of reference points
l_t	Distance from target
Nd:Yag	Neodymium-doped Yttrium Aluminium Garnet
PIV	Particle Image Velocimitry
p_∞	Free Stream Pressure
TKE	Turbulent Kinetic Energy
TSS	Turbulent Shear Stress
u_∞	Free Stream Velocity
u	Flow Velocity
u'	Fluctuating component of Velocity
U,V,W	velocity components in the x, y, z direction
U_i	Instantaneious U component of velocity
U_i	Measure velocity including out of plane component of velocity
U_{median}	Median value of all U components fo the neighboring vectors

U_{rms}	Deviation of U components of the neighbor vectos
V_{median}	Median value of all U components fo the neighboring vectors
V_{rms}	Deviation of V components of the neighbor vectos
W_{median}	Median value of all U components fo the neighboring vectors
W_{rms}	Deviation of W components of the neighbor vectos

Chapter 1

Introduction

1.1 Aerodynamics of Automobile Mirrors

Aerodynamics of road vehicles continue to play a crucial role in automobile design and are currently the focus of numerous research topics. In general, we can consider the aerodynamics of a road vehicle and their extensions to be very similar to the aerodynamics of a bluff body close to the ground [1]. Due to the unsteady and turbulent nature and the complex three dimensional flow field around typical road vehicles, flow optimization through wind tunnel experimentation and Computational Fluid Dynamics using Large Eddie Simulation (LES) are performed regularly throughout design phases. Both techniques are utilized in an effort to design a quieter and more fuel efficient automobile for consumers. For aerodynamicists optimizing bluff bodies, reducing the pressure drag is usually the main focus of design enhancements. Its estimated that 70% - 90% of the total bluff body vehicle drag can be attributed to the influence of pressure drag [2]. Much of previous research efforts have striven to curb the main parasitic losses of bluff bodies such as flow separation and base pressure recovery in the wake region. J. HA et al. (2010) presented both the experimental and computational work on reducing the drag of a pickup truck body by extending a flap on the trailing edge of the cabin roof angled downward toward the tailgate. This method was successful at increasing the surface pressure coefficient on

the cabin rear surface and eliminated the attachment of the bed flow to the tailgate [3]. Additional experimentation that has proven to be an effective measure at reducing the base pressure and increasing the wake region stability have been accomplished through active flow control techniques, vehicle geometry alterations and by installing new aerodynamic features such as flaps in order to impart flow control on the free stream. Beaudoin et al (2007) proved that flow control methods implemented on an Ahmed bluff body could yield highly favorable results in reducing the drag and lift coefficients depending on the flap configuration and applied angles to the mean flow direction. This was achieved by increasing the angle of flaps along the rear trailing edges of the geometry relative to the slanted rear surface of the body[4]. Todays efforts to continuously increase aerodynamics efficiency in order to comply with governmental regulations drives us towards new and innovative designs that not only ensure a more environmentally friendly automobile for consumers but also an increasing role in aerodynamics in vehicle design for years to follow.

Despite our desire to optimize a vehicles aerodynamics, the final design of an automobile is usually the result of contributions from various design teams with unique optimization criteria to satisfy. While it may be the task of the exterior design specialist to enhance the aesthetic character of the automobile [5], the requirements for passenger saftey may inhibit and influence the visual styling away from the original concept. The end product of such a design can be seen as the successful refinement of all the contributions and recomendations integrated into a final product [5]. While meeting the design specifications of multiple performance criteria can prove to be quite challenging, incorporating such changes affordably across a fleet platforms can prove to be just as challenging as well. Its commonly known today that auto manufactures regularly use the concept of shared platforms as a strategy maintain a low development cost between the models they produce. In 2006, Volkswagen's A5/6 platform was reported to have been the highest shared platform by volume with over 2.3 million cars from auto manufacturers such as Volkswagen, Audi, Seat, and Skoda. With reported figures as large as 25% of the total cost to develop new vehicles being

attributed to development alone, an evolutionary, low cost and low drag aerodynamic solution that does not require the complete redesign of existing automobile assemblies will not only aid automobile manufacturers in meeting the stringent fuel economy regulations of the future but also do so while preserving development cost as well [5]. In the face of global competition and strict regulations, any small advantage could prove to serve large competitive gains.

Certain vehicle parameters such as vehicle emissions, fuel economy and maximum speed can be directly influenced by a vehicle's aerodynamic performance [2]. While automobile external rear view mirrors may seem small enough to consider their drag essentially negligible, it is reported that 2% - 4% of the total aerodynamic drag for automobiles is attributed to the rear view mirror design while 2% - 10% is attributed to the total drag of heavy duty trucks. These numbers show a large potential to increasing the overall efficiency of automobiles in general and in turn reduce the CO_2 emissions that are a byproduct of energy consumption. According to a recent study by the U.S.Energy Information Admininistration, projected total transportation energy consumption for the U.S. in the quadrillion BTU's is expected to decrease despite an increase in the millions of miles driven by both light and heavy duty vehicles. It is also estimated that despite the projected gains in efficiency for both classes of transportation over the 28 year period, heavy duty vechile energy consumption is expected to increase by nearly 8.5% of the 2012 total energy consumed where as light duty vehicles would decrease by nearly 15% of the 2012 total energy consumed [6]. This data not only stresses the importance in addressing the inefficiency of the heavy-duty class of transportations but also illuminates the significant potential savings that can be acomplished by reductions through base drag reductions.

1.2 Regulatory Background

Fuel economy standards have been enforced since the enactment of 1975 Energy Policy and Conservation Act (EPCA) in an effort to ebb Green House Gas

emissions while establishing an economy with greater energy independence. In the wake of the 1970s oil crisis, the National Highway Transportation and Safety Administration was tasked to create a national regulatory program aimed at motor vehicle fuel economy in order to ensure these goals could be met. Starting in 1978 for passenger cars and progressing to include light duty trucks under the 8500lb Gross Vehicle Weight criteria in 1980, CAFE standards have served as the national fuel efficiency regulatory standard that have encompassed not only fuel consumption but also the amount of products of combustion as well. Up until 2010, emission controls in conjunction with fuel economy regulations implemented through the Environmental Protection Agencys Corporate Average Fleet Economy (CAFE) standards only applied to certain classes of vehicles that operate on our roads today which include Passenger Cars and Light Trucks. According to the 2010 Light-Duty Vehicle Greenhouse Gas Emission Standards and Corporate Average Fuel Economy Standard Final Rule, it was reported in 2007 that 28% of our nations fuel consumption was accounted for by transportation sources [7]. In February of 2014, a White House published document, Improving the Fuel Efficiency of American Trucks, stating that by 2010 25% of on-road energy use and GHG emissions could be accounted from heavy-duty trucks which represented only 4% of the total on road vehicles at the time [8]. This class of transportation was second in emission of GHGs to only passenger car and light duty trucks. Heavy duty trucks accounted for a quarter of the national total transportation fuel consumption but was only subjected to restrictions relating to their byproducts of combustion. This inevitably led to new directives for the EPA and the National Highway Traffic Safety Administration to produce new stricter fuel regulations in order to increase the efficiencies of these vehicles which came in the form of the Presidential Climate Action Plan (CAP) of June 2013.

In accordance with requirements for the new regulations called upon in the CAP of 2013, Medium-Duty and Heavy-Duty trucks for the model years of 2014 through 2018 were now considered under the regulation provided for under the CAFE standards pertaining to not only more stringent emission controls including CO_2 but

for the first time an additional fuel efficiency restriction as well. These vehicles include heavy duty pickup trucks and vans, combination tractors also known as semi-trucks and vocational vehicles such as busses and garbage trucks [7,8]. Due to the direct nature of the relationship in reducing CO_2 emissions and increasing fuel economy, any increase in the fuel economy of a vehicle would essentially decrease the amount of CO_2 produced. Although current emission control technologies do exist to aid the reduction of certain byproducts of combustion, increasing the fuel economy through aerodynamic efficiency could provide substantial reductions as well. As mentioned by the Rule and Regulations pertaining the CAFE standards of 2010, enhancements to improve efficiency and reduce the emissions from products of combustion will have an impact in the per unit cost of the vehicles and in turn will be more expensive to the consumers [7]. Thus, low cost improvements to existing vehicle designs that aid in bridging the gap between the capabilities of todays vehicles and the standards for tomorrow could present a solution for manufacturers whose fleets are dominated by inefficient heavy duty vehicles. As a low drag aerodynamic solution, the Jet Boat Tail mirror design has the potential to provide improved aerodynamic efficiency of existing fleets while preserving development costs for auto manufactures.

1.3 Benefits of Passive Flow Control Incorporated In an Automotive Mirror for Drag Reduction

Reductions in the dominant contributor to the drag force of bluff bodies can be achieved through the passive flow control implementation on extended rear view mirrors in addition to similar geometries. Based on the drag equation for the net force acting parallel to the freestream flow direction

$$D = i \dot{\oint} [-(p - p_\infty)n + \tau_(\omega)t)\mathrm{d}x \tag{1.1}$$

The drag force effectively has two components. The pressure component

corresponding to the influence on the total drag imparted by the base pressure and the friction drag. Friction drag is the component that is attributed to the skin friction of the body from the resulting shear stress distribution across the surface of the mirror. Effectively, by implementing a passive flow control jet in the rear mirror surface of the wake region, an increase in the pressure of the wake region will reduce the overall pressure delta for the enclosed area of the surface integral. These effects are produced through the vorticity enhancements in the shear layer that aid in the flow entrainment and energizing of the wake region. These phenomena are observed to produce a reduction of the of the wake region documented by mean velocity streamlines for each model in addition to reduced velocity profiles at multiple downstream locations.

$$D = \int_{\delta} \rho u(u_{\infty} - u)\mathrm{d}y \tag{1.2}$$

Equation 1.2 shows that a reduction in the difference between the measured velocity in the recirculation region and the free stream will result in a reduction of the drag force measured. Figure 1.1 below displays the typical wake area for a cylinder in a free stream flow. As described by equation 1.2, the overall magnitude of the drag force can be reduced through the reduction in the area of the wake in addition to the velocity profile [9].

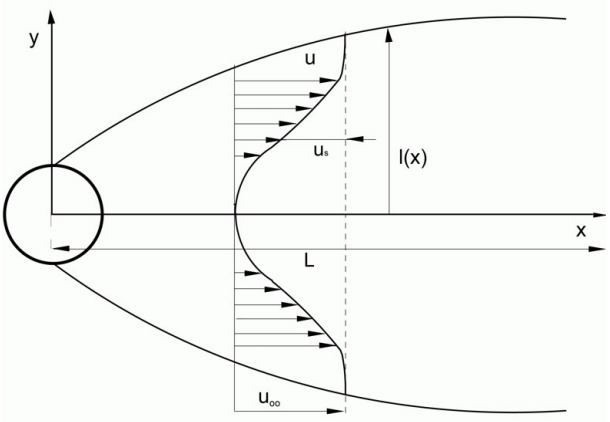

Figure 1.1: Diagram of the wake region beind a cylinder.

Roshko was also able to derive a relation evaluating the base suction in terms of the free stream pressure and the shear stress around the zero streamline of the wake

region [10]. By considering the shear stress along the zero streamline, the force balance equation can be described as

$$(P_b - P_\infty)d + 2\tau L = 0 \tag{1.3}$$

where P_∞d is the force contribution from the reattachment region. Rearranging the equation, the relation shows that reducing the shear stress will result in a reduction of the base pressure. For Reynolds numbers high in value, the wake shear stress can be observed as the Reynolds stress represented by $\overline{\rho u' v'}$. The following relation displays the dependency of the base pressure P_b and the shear stress of the wake region as

$$P_b = P_\infty - 2\tau \frac{L}{d} \tag{1.4}$$

where τ is recognized as

$$\tau = \overline{\rho u' v'} \tag{1.5}$$

To achieve the reduction in the wake area and base pressure, flow entrainment from the high kinetic energy free stream air is incorporated into base region thus reducing the recirculation region velocity as well. Flow entrianment can be described from the following equations assuming a two dimension flow for an incompressible fluid. If we assume n_e to be the entrainment unit vector normal to the boundary layer to be defined by the equation

$$n_e = j - i\frac{d\delta}{dx} \tag{1.6}$$

and u to be the free stream velocity, the relation for the entrainment velocity along the surface of the of the boundary layer can be observed as $u \cdot n_\mathrm{e}$

$$u \cdot n_e = v_e - u_e \frac{d\delta}{dx} \tag{1.7}$$

where the representative equation for a two dimensional, incompressible boundary

layer can be viewed as

$$\frac{d}{dx}\int_0^{\delta} \rho u dy + \rho(v_e - u_e \frac{d\delta}{dx}) = 0 \tag{1.8}$$

Equation 1.8 can be interpreted to show that the rate of change in mass flux through the boundary layer is equal the rate at which fluid is entrainted into the recirculation region from the high kinetic energy free steam. When conditions are such that the entrainment velocity show in equation 1.7 is negative, the mass flux component will incrase and cause the boundary layer thickness to increase as well [11].

In addition to decreasing the wake area through increased entrainment and mixing layer thickness, the passive flow control mirror also reduces the large scale flow separation of the shear layer in the unsteady wake region as a result of incorporating a passive jet into the base area. Its commonly believed that one of the sources of aerodynamically induced noise is from unsteady flow separation. A recent study by Kozlov presents results that indicate reducing the unsteady flow separation from cylindrical bodies through active flow control can lead to a reduction in the large sale vortex shedding [12]. Utilizing streamwise oriented plasma jet actuators, a cross stream momentum transfer aided in inhibiting Karman vortex shedding and in turn turbulence levels in the wake region. Through experimental investigations, aerodynamic noise reductions were found to be in the range of 11-14 dB [12]. These finding suggest that potential benefits in noise reduction could be obtained from the passive the passive flow control design.

When considering a flow control method design, certain design factors should be considered to ensure the gain in efficiencies do not cause any additional penalties on the system as well [13,14]. Factors such as the effectiveness of the design, the energy efficiency of the system and the ease of implementation should all be evaluated [15]. Although this implementation of flow control is not in the traditional sense where its applied to airfoils and lifting bodies, the parameters still apply and can be used to validate the design. Through the implementation of a passive flow control extended rear view mirror, a reduction of the overall base pressure drag and wake area should be

achieved for the new design. Additionally, these gains should be obtained at a minimal cost to the manufacturing process that is involved in producing the existing automobile mirrors while requiring little redesigning or mirror surface reduction in order to eliminate compliance of existing designs with safety regulations. Since this method of flow control relies on the free stream air in order to energize the wake region, its passive jet ensures there very little dependence on the vehicle's engine other than to produce the required force to drive the car. As a low cost modification where its design can be seen to be evolutionary in nature, the flow control automobile mirror proves to be an effective means of improving the aerodynamics of an existing automobile mirror.

The typical automtive mirror design can be seen below along with the expected wake region behavior due to viscous forces.

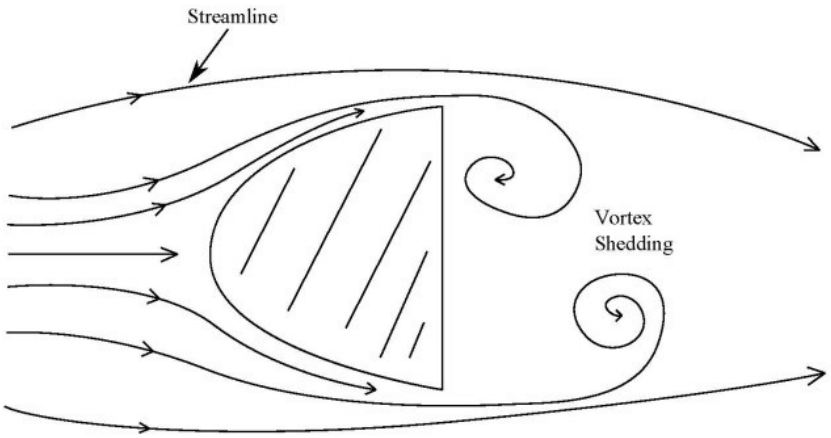

Figure 1.2: Diagram of an automobile mirror without passive flow control incorporated into its design.

The passive flow control design incorporates a free stream air inlet at the leading edge of the mirror body in order to allow high kinetic energy flow to pass through a channel and be ducted out the rearward surface of the mirror. As the flow enters the ducted inlet, it's channeled through a converging nozzle to where it directed out the injection slot of the rear body surface. The injection slot delivering the high energy jet is accomplished via a circumferential diverging slot along the rear body surface at trailing edge of the mirror.

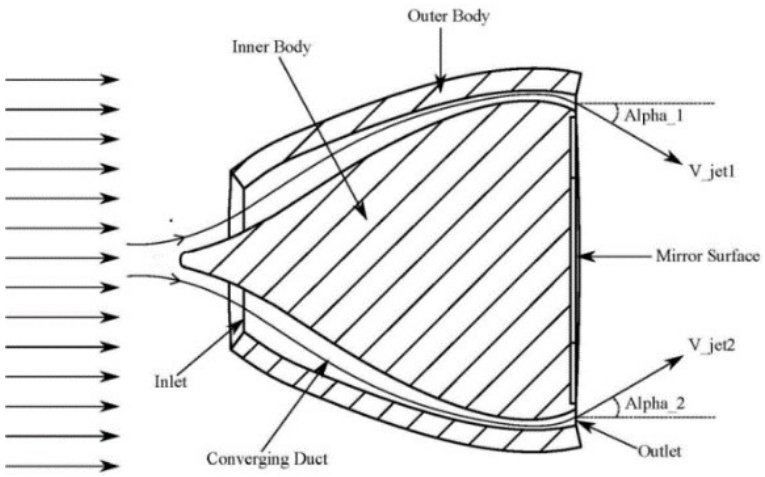

Figure 1.3: Diagram of flow control mirror design.

The jet along the rear of the mirror surface is angled towards the center at a slight angle (alpha) and allows for enhanced vorticity production from the jet mixing the surround air. This mixing effect due to the interaction of the jet causes a noticeable change in the coherent structures produced due to the enhanced vorticity and noticeable circumferential contraction in the wake profile where the jet mixes with the free stream shear layer. The mixing of the jet with the free shear layer of the flow over the mirror body not only produces an immediate wake area reduction but also mitigates the adverse pressure gradients that would otherwise force the free shear layer to diverge from the mirror surface.

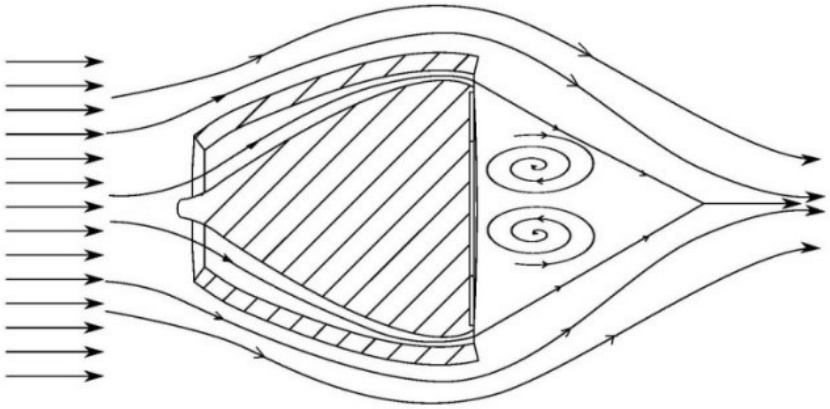

Figure 1.4: Expected wake region of flow control enhanced mirror deisgn.

Although it cannot be experimentally measured, it is estimated with the inherent elimination of flow separation from the body surface, aerodynamically induced noise

in attenuated as well. Through flow entrainment and enhanced vorticity, the energized wake region is significantly reduced and thus the base pressure drag of the model should be as well.

1.4 Objective

The purpose of this research is to experimentally investigate and validate the application of passive Jet Boat Tail on a bluff body extended rear view mirror design in order to analyze the effects of the applied passive flow control and its enhancements. The research included the design and manufacturing a reinforced force balance mounting apparatus to secure the models inside the wind tunnel test section in addition of an aerodynamic mounting extension to position the extended rear view mirror in the center of the test section as well. The experimental investigation includes PIV analysis of three configurations with the laser plane at the center line of the models in addition to three additional locations in the spanwise direction. Due to the complex three dimensional flow associated with the body geometry in addition to the JBT effects on the wake region, spanwise slices were acquired to evaluate the flow at different locations along mirror semi major axis for Reynolds number of $Re=2.55x10^5$ for all three configurations. Configurations of baseline, Jet1 and Jet2. Reynolds numbers from $Re =8.5x10^3$ to $Re=3.83x10^6$ were measured using the University of Miamis PIV instrumentation system resulting in measurements for the u, v, w components of velocity, corresponding Reynolds Stress values in addition to the Turbulent Kinetic Energy as well. The results from this experimentation is used to generate a more thorough understanding of the fluid dynamic mechanisms that are at work and to provide a detailed analysis to the major contributing factors in the design performance. All experimentation was performed at the University of Miami Wind Tunnel Laboratory.

Chapter 2

Experimentation and Data Analysis

2.1 Wind Tunnel Laboratory

The experiments were conducted at the Mechanical and Aerospace Department Co-Flow Jet Wind Tunnel Facility of the University of Miami. The wind tunnel used is an Engineering Laboratory Design Inc. closed working section, Open Circuit wind tunnel rated to a maximum wind tunnel velocity of 45.7 m/s with minimal blockage. The tunnel test section is 48in (121.0cm) with a test cross sectional area of 2in x 24in (61.0cm x 61.0cm). The test section of the wind tunnel has been heavily modified with aluminum sidewalls to support loadings of a Co-Flow Jet NACA 6415 airfoil with a 12in (30.48cm) chord. The test section sides comprise of 0.75in (1.90cm) acrylic walls on all four sides in order to provide optimum optical analysis from multiple perspectives. Before the commencement of the mirror testing, the force balance mounting apparatus for the wind tunnel was redesigned in order to provide a more secure attachment location of the AMTI six axis balance. Previous experimentation using the wind tunnel resulted in the support for the force balance to plastically deform and shift the center line of the sting extension off center. This resulted in the force balance and the connecting high pressure injection pipe for the CFJ configuration to no longer being in proper alignment with the wind tunnel test section and thus resulted in the force balance to be at an angled offset in addition to the

airfoil model not being normal to the air flow direction.

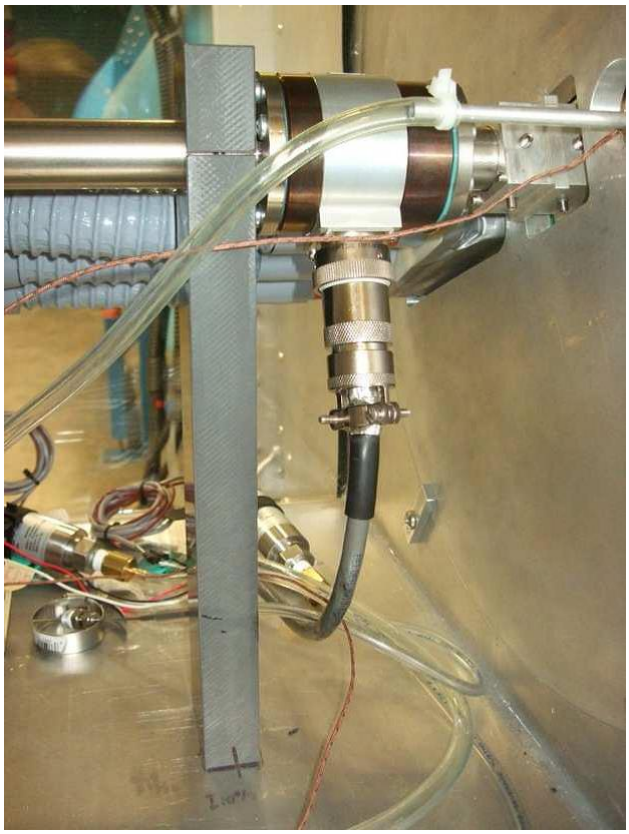

Figure 2.1: Original wind tunnel load cell support column that was redesigned and replaced.

This deflection in the orientation of the force balance caused components of the lift and drag force from wind tunnel experimentations to be projected at in the X, Y and Z directions at complex angles and different magnitudes depending on the angle of rotation or attack of the model. The plastic deformation of the PVC support also caused the stainless steel High Pressure Injection pipe to deform as well after being subjected to loadings while in various positions. Due to the deflection of the high pressure injection pipe/sting extender, a new system was designed to ensure that force balance orientation would always be in the correct position and to facilitate the ease of rotating the model in wind tunnel test section. This redesign of the force balance support was also made to accommodate any future work including pitching airfoil experimentation as well. All CAD modeling was performed using SolidWorks 2013. In order to facilitate the production of a new support system, Solidworks drawings for various off the shelf parts were use in addition to their dimensions to ensure clearances were correct.

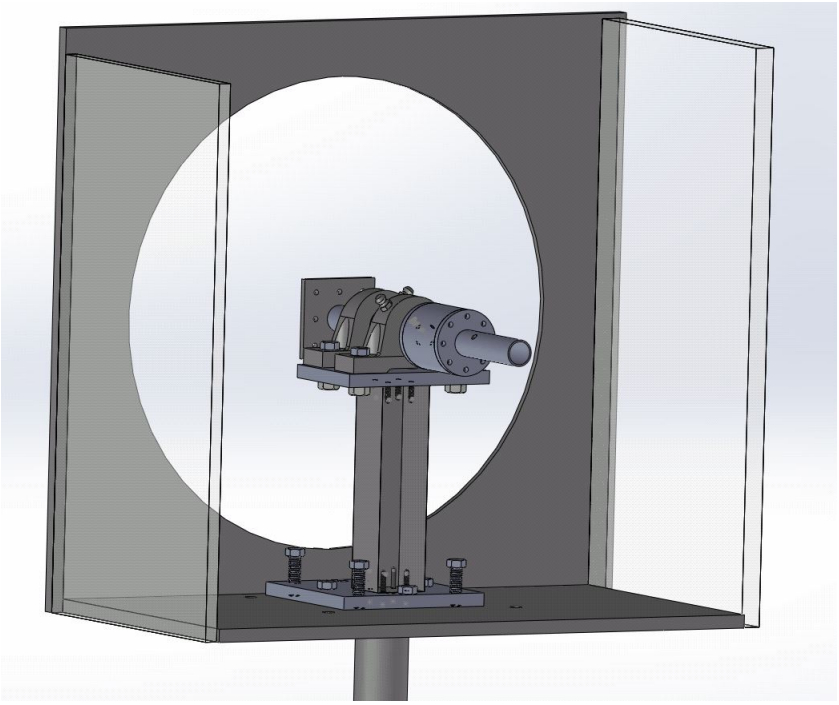

Figure 2.2: Solidworks modeling of the sting/force ballance support

The new balance support consist of two .25in (.0635cm) Aluminum plates attached to a 2inx2in (5.08cm x 5.08cm) Aluminum 6061 bar stock that has been cut to the height of 7.8in (19.96 cm). Four stainless steel #10-32 x 1in screws on each end were used to secure the top and bottom plates to the aluminum support member. The total height for the support assembly including the top plate and base is 8.86in (22.50cm) which is shorter than the measured centerline to the mounting plate for the sting extension. This was intentionally done to allow for clearance in the required height and for the use of shims in order to achieve the actual final height for the assembly.

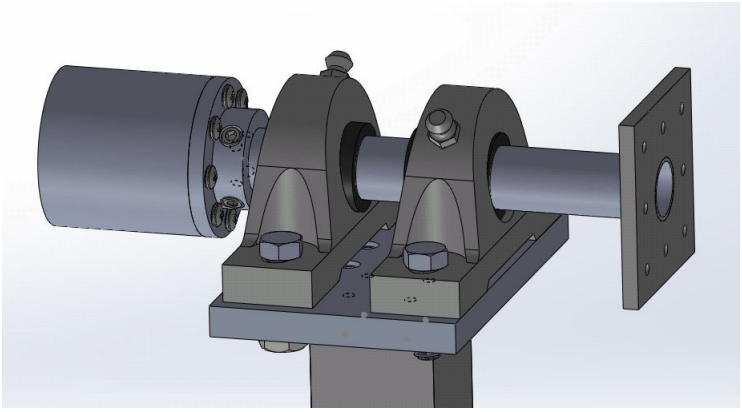

Figure 2.3: Solidworks modeling of the bearing support for the sting/force balance extender.

The dimension of the base plate is 6in x 6in (15.24cm x 15.24cm) and the top mounting plate is 6in x 4in (15.24cm x 10.16cm). In order to support the sting extender, two mounted bearings were used with an inner race diameter of 1.0in (2.54cm) and placed 3 inches apart as shown in Figure 2.2. Due to the proximity of the bearing and their location on the top plate, four holes were counterbored .25in deep in order to recess the #10-32 cap screws used to secure the top plate to the aluminum bar support. This gave the cap screws the clearance of .08in between the surface of the top plate and the top surface of the cap screw.

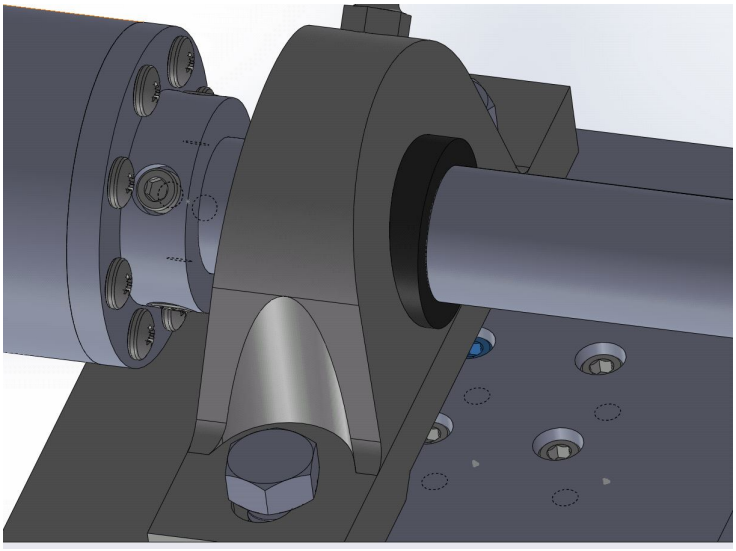

Figure 2.4: Solidworks modeling of the bearing support for the sting/force balance extender.

The main design goal for the new balance mount was to create a system that would ultimately be modular and easily repaired. With this in mind all parts for the assembly can be purchased through hardware distributors and easily replaced if needed. Keeping the assembly modular also allowed for minimal welding and the use of fasteners where possible which make disassembly possible should items need to be repaired.

The new high pressure injection tube/balance extender was fabricated using a stainless 304 pipe with an outer diameter of 1in (2.54cm) and a final length of 7.362in (18.67 cm). The concentricity of the pipe was compromised by the seam where it was welded making the pipe not perfectly round with roughly .008in run out. The inner diameter of the pipe is .760 giving it a wall thickness of .120in. In order to correct the run out and allow the new stainless sting extension to clear the bearing races, the OD

needed to be turned down in order to get the correct diameter for fitment. This was done at the machine shop for the college of Engineering at the University of Miami. Using a Lathe, the stainless steel sting extension was reduced to an overall final diameter of .995in giving it enough clearance to fit properly through the bearing races. Once turned down, the pipe was welded to ta 3in x 3in x .125in (7.62cm x 7.62cm x .3175cm) flange plate at one end. On the opposite end of the sting extension pipe, four #10-32 taped holes were machined 90 degrees apart in order to fasten the collar flange to pipe end. The collar is made of 304 Stainless Steel and was machined from round bar stock. Four #10-32 x .25in cap screws were used to secure the collar to the pipe shaft thorough counter bored holes which made the screws almost flush with the face of the collar.

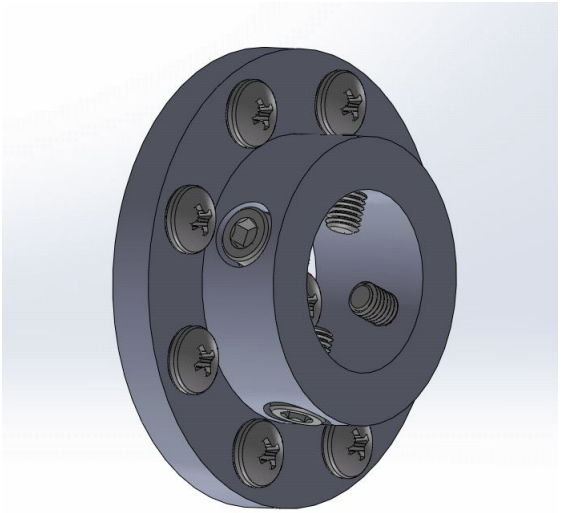

Figure 2.5: Solidworks modeling of the collar for the sting/force balance extender.

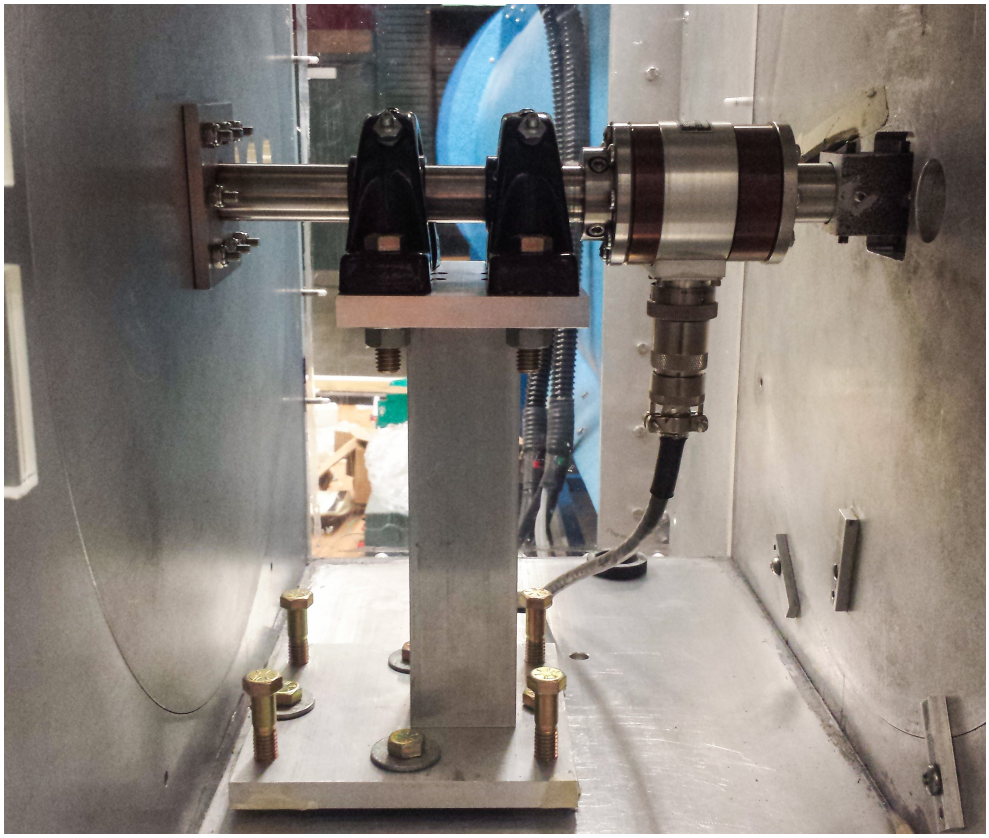

Figure 2.6: Assembled support including sting/force balance extender installed in the University of Miami Wind Tunnel Facility.

2.2 Particle Image Velocimetry Analysis of Jet Boat Tail Mirror Deisgn

Over the years there has been many improvements in experimental techniques utilized to collect and analyze flow field data. From single/multi-point solutions such as hot wire anemometry and including nonintrusive planar techniques such as PIV. Our abilities to measure and acquire complex data from fluid flow is becoming more sophisticated as our computational power increases over time. The PIV measurement technique has benefited from advancements in computational capabilities, evolving from double exposure single frame measurements, stereoscopic multi-camera configurations to even Light Field Optic cameras. One of the many benefits of PIV is its nonintrusive nature in measuring the flow fields of interest. Without the need of placing interfering equipment the field of interest, PIV allows the optical collection of information through single or multiple cameras in stereo configurations where the undisturbed, natural flow field behavior can be observed in 2 or 3 dimensions. The principle goals of this experiment was to investigate the flow field behavior due to the addition of a passive jet in two configurations when applied to bluff body geometries. To measure such effects, the u, v, w components of velocity, corresponding Reynolds Stress, Vorticity and Turbulent Kinetic Energy were used to evaluate the behavior of the models and the influence of the jet on the immediate wake region of flow.

2.3 Mirror Geometries

All Particle Image Velocimetry was performed at the University of Miami Co-Flow Jet Wind Tunnel Laboratory. The experimental geometries were manufactured using Selective Laser Sintering 3D printing. The three configurations presented are referred to as Baseline, Jet1 and Jet2. The baseline test model has a length of 129.30 mm, a semi minor axis length of 115.12mm and a semi major axis length of 178.62 mm measured at the inside surface of the housing. The baseline

geometry serves as the model to which all alterations were subsequently made. In order to incorporate the passive flow control for the Jet1 design, the baseline configuration was designed with a removable inlet cap and interior ducting in order to channel the high energy free stream flow through shell cavity and allow it to exit via a rear circumferential slot as seen in Figure 2.8. Figure 2.7 is an exploded view of the assembly for the baseline model including the inlet cap and its M1/M2 fasteners. The Jet1 inlet dimensions consists of a 56.23mm semi major axis length and 37.13mm semi minor axis length which produces an inlet area 2139.95 mm^2 and a rear circumferential slot area of 725.38mm^2 with a uniform slot height of 1.44mm. The rear jet of the Jet1 configuration is angled slightly towards the centerline of the recirculation region at 7° and has an inlet to outlet slot area ratio of 2.95. The Jet2 configuration consists of larger inlet and outlet circumferential slot area in addition to a shortened outer shell assembly as can be observed in the figures 2.9 and 2.10. Although the overall length of the outer shell for the Jet2 configuration was altered, the profile was kept consistent between the models. The shape was intentionally kept consistent to allow for the analysis between the higher mass flow rate of the larger jet and increased inlet area. The length of the Jet2 geometry was reduced to 87.77 mm, 41.26mm shorter than the baseline configuration. The new inlet geometry consists of a semi major and semi minor axis length of 135.03mm and 89.33mm which facilitated the larger inlet area of 8,854.87 mm^2 for the higher duct mass flow rate. The outlet area for the Jet2 configuration consists of a semi major length of 180.64mm and semi minor length of 116.65mm which allow for an outlet area of outlet area of 2,017.7mm^2. The overall ratio of the inlet area to outlet slot area is 4.39 for the Jet2 configuration, which is significantly larger than the inlet to outlet ratio of the Jet1 configuration. Unlike the Jet1 configuration, the duct angle is not uniform throughout the model's minor and major axis and is measured at 6.71° and 3.34° towards the recirculation centerline.

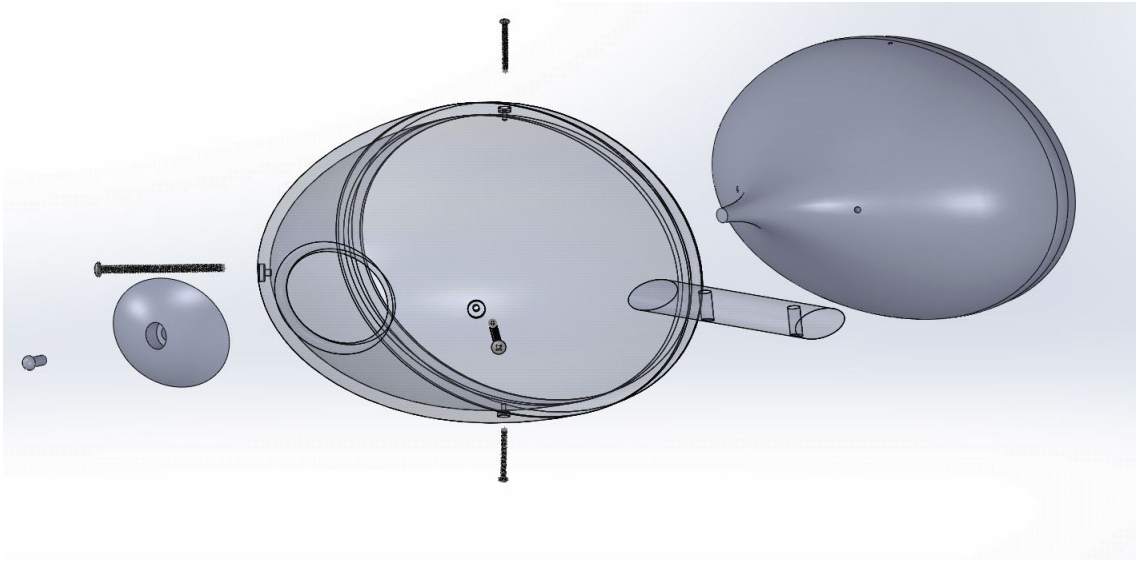

Figure 2.7: Baseline/ Jet1 Configuration exploded view of assembly

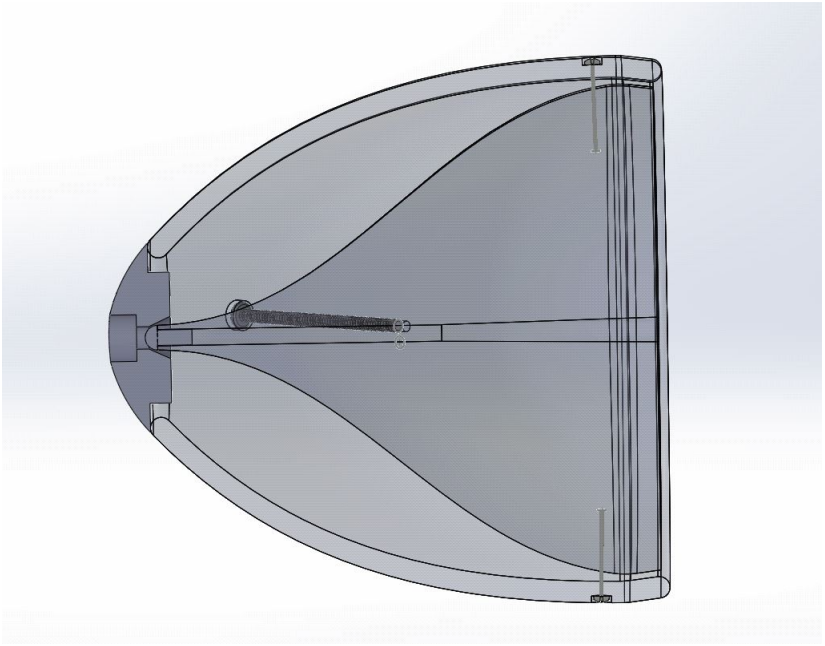

Figure 2.8: Jet1 Mirror assembly cross sectional view

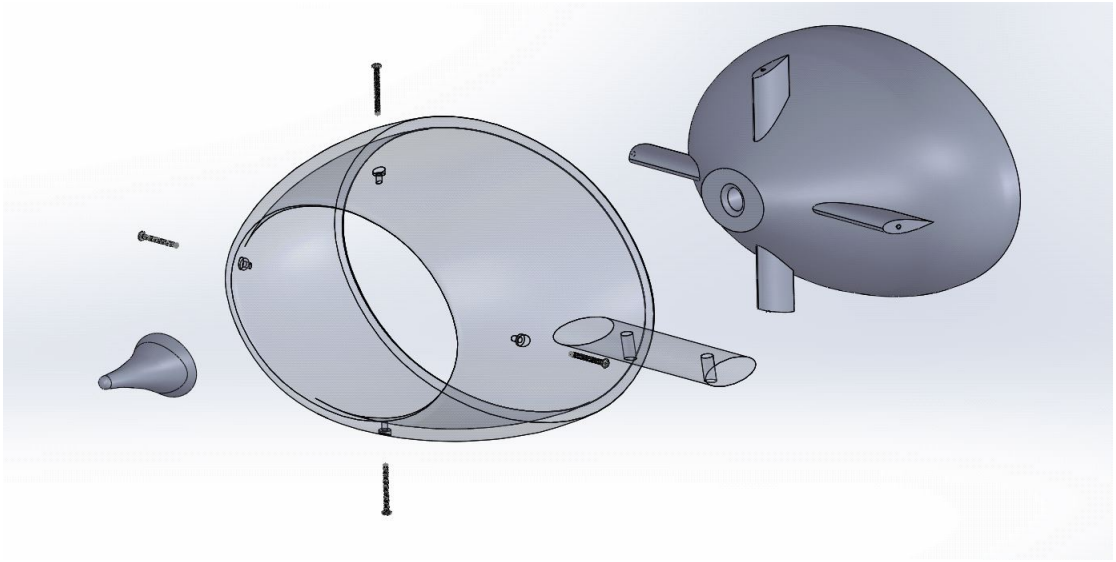

Figure 2.9: Jet2 Mirror assembly exploded view

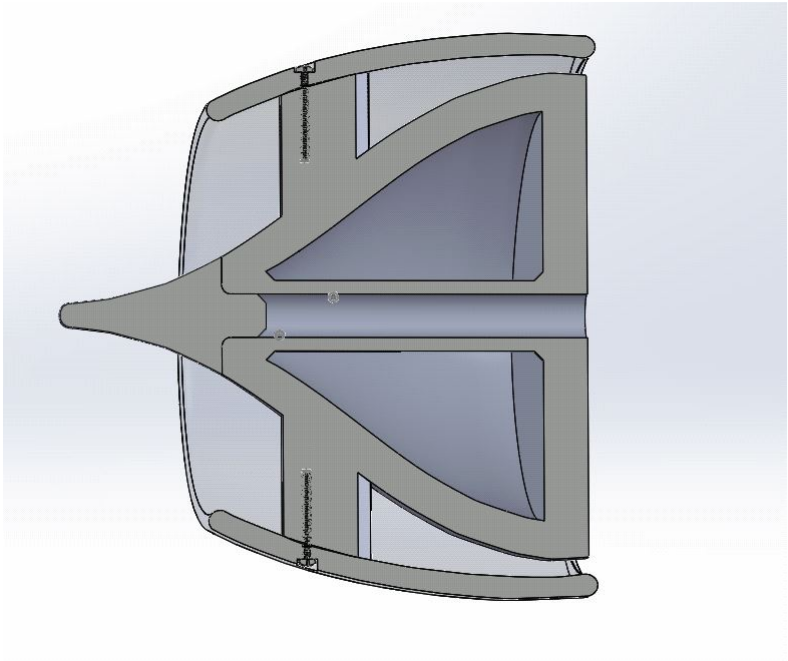

Figure 2.10: Jet2 Mirror assembly cross-sectional view.

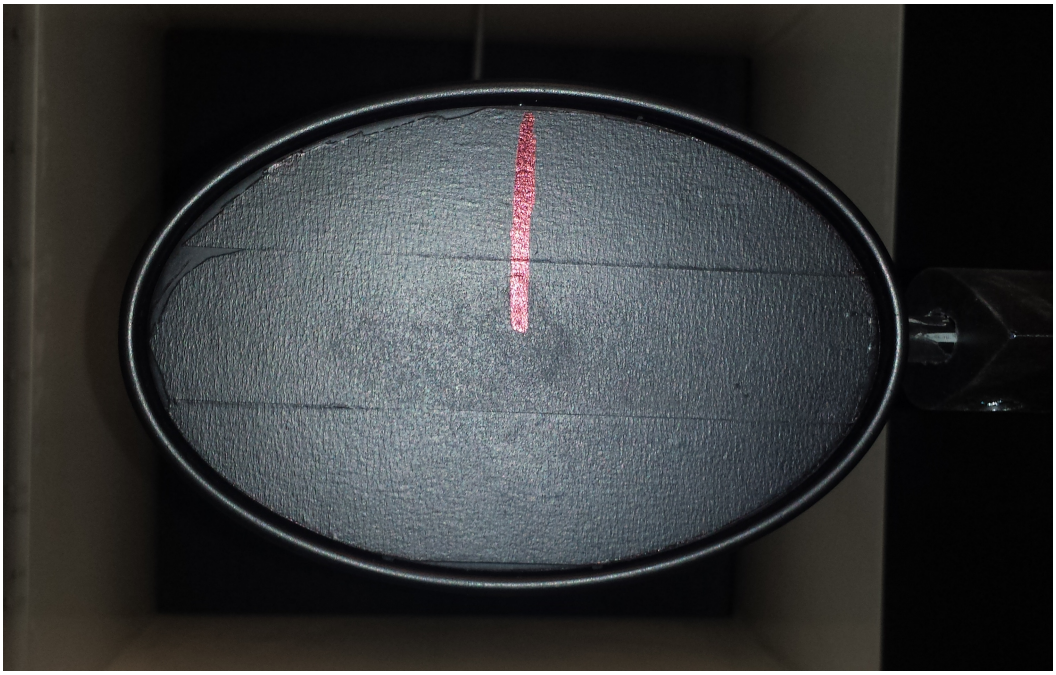

Figure 2.11: Jet1 Mirror Circumfrential Jet

Figure 2.12: Jet2 Mirror Circumfrential Jet

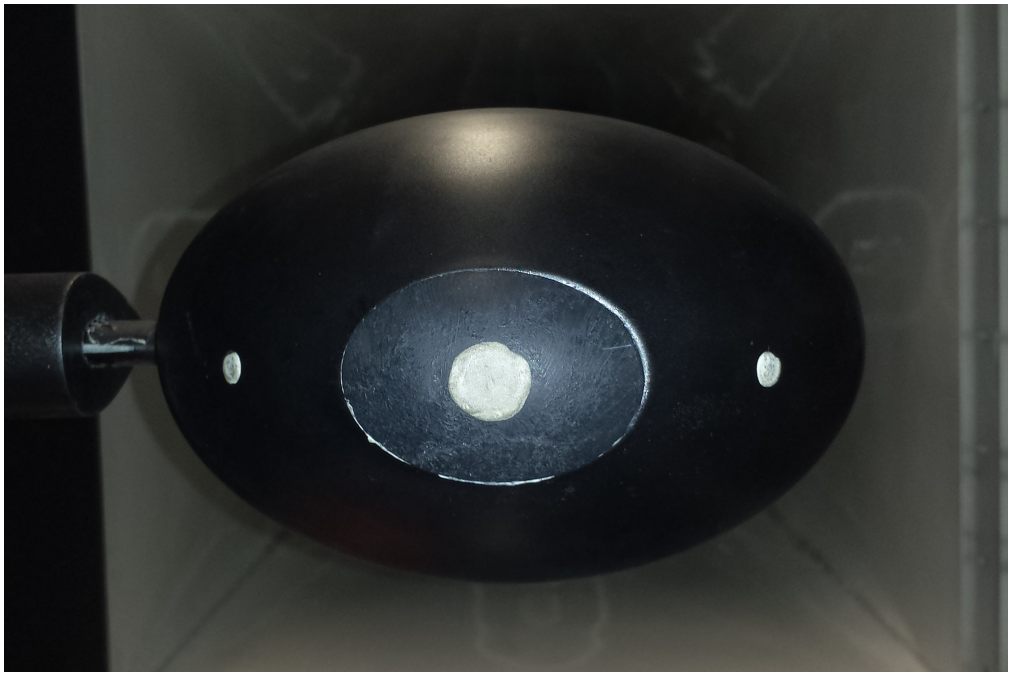

Figure 2.13: Baseline Mirror with the center cap applied.

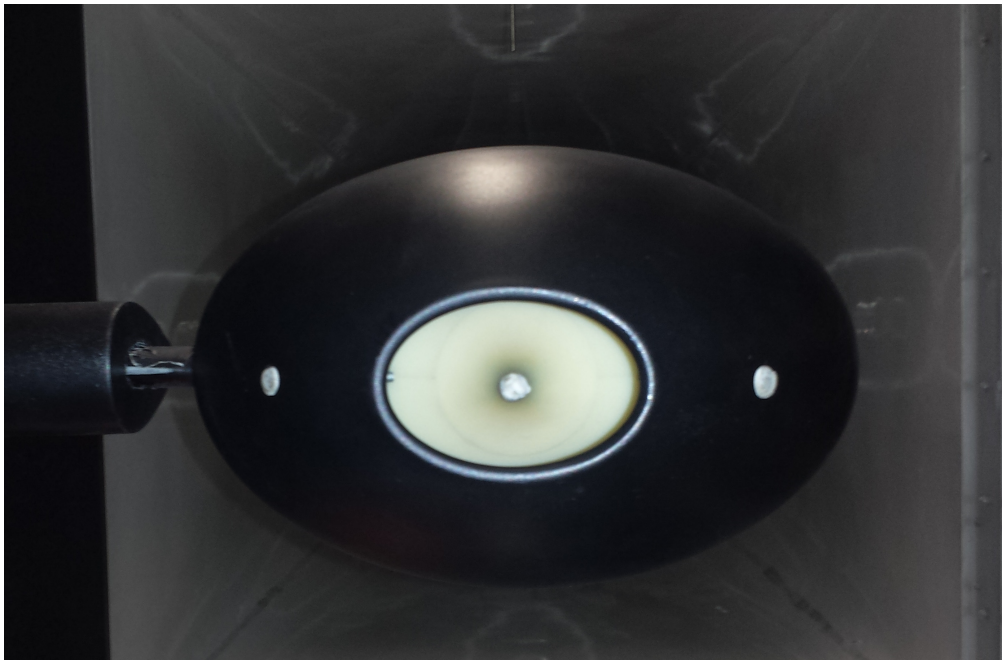

Figure 2.14: Jet1 Mirror without the center cap applied.

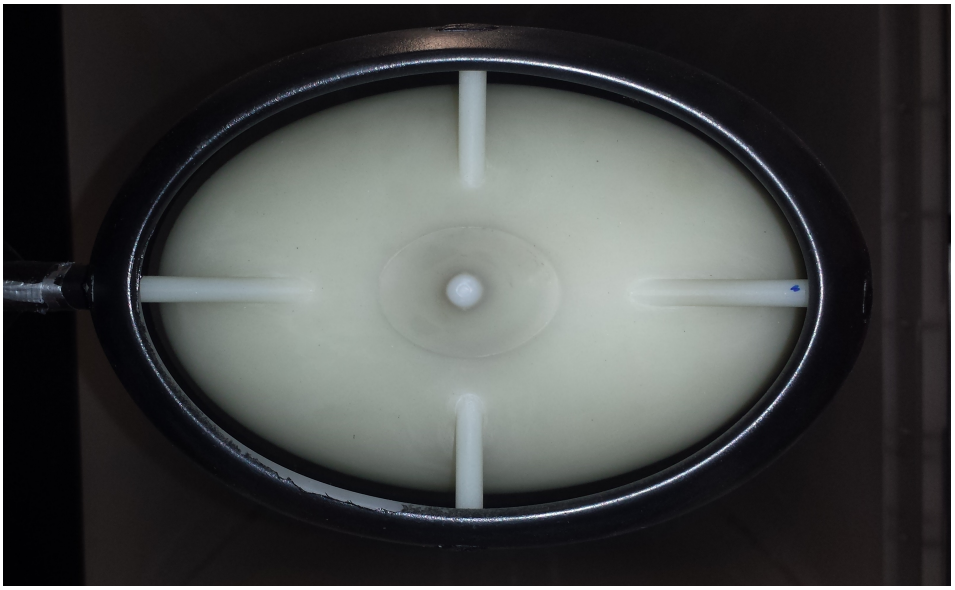

Figure 2.15: Jet2 Mirror Inlet View

Model	Baseline	Jet1	Jet2
Height	129.30	120.0	87.77
Inlet Area		2139.95	8854.87
Base Area	18535.50	725.38	2017.71
I/O Ratio		2.95	4.39

Table 2.1: Table of Mirror Geometries

	Jet1		Jet2	
Duct Height	1.4	1.4	5.00	3.83
Outlet Angle	7°	7°	6.71°	3.34°

Table 2.2: Table of Mirror Duct Height for Jet1 and Jet2 models. Outlet angles for both JBT models are given as well.

	Jet1	Jet2
Inlet Area	12%	48%
Outlet Area	4%	11%

Table 2.3: Table of Mirror Inlet and Outlet Areas vs Base Area as percent

2.4 PIV Experimental Parameters

For these particular models, results from Reynolds numbers of Re =85,203 and Re = 298,212 are presented. The PIV system designed by LaVision was utilized in the EDL

inc. wind tunnel with the modified test section. The PIV system hardware includes two cameras, laser, laser power supply, PTUs or power timing units, and the post processing computer. All components are specifically designed to integrate together and be controlled by the post processing computer in order to correctly record the corresponding particle displacements during the time interval between frames. The planar light sheet is made from a 135mJ, dual cavity Nd:Yag laser with wave lengths of 532nm and 1064 nm directed into the test section by a mirror.

Before any data acquisition can be performed a calibration of the PIV system is required in order to create a mapping of the spatial domain of interest to the CCD camera sensor. This allows for the translation of the particle displacement in the spatial domain to be converted to a scale of pixel shifts. Ultimately, the particle displacement recorded will be a results of the pixel shift measured by the CCD sensor of the camera that is translated according the image calibration to the correct distance in the spatial domain. For a two camera stereoscopic configuration, both cameras are required to be calibrated simultaneously in order to ensure the mapping is done correctly. In this step, two images are created for each calibration image acquired and the image of camera 2 is dewarped and mapped to the calibration of camera 1. This is performed with the aid of the Lavision PIV software DaVis by running the calibration batch process. In this calibration batch process, the number of views must be selected that is appropriate for the experimentation in order to correctly set the parameters for the calibration. At this time, options to include more than one view can be selected in order to define the coordinate system. If the intention is to include N views, N images of the calibration block for both cameras will have to be included in the calibration process in order to correctly find a dewarping function to correct of the distortions in the camera images. One view was used in the experiments performed and is sufficient at providing the dewarping function needed for the pixel shift translation to spatial units. In multiple view configuration, the first view is always used to define the x-y axis and in turn the z as well. Certain mapping functions do require multiple views, but the pinhole calibration function that was utilized in the experimentation only required one view in

the plane of the laser sheet. For the stereoscopic images that were collected, the 2 Camera Mapped option was utilized in addition to the Type 11 3D calibration block to facilitate the mapping of the two cameras on two planes.

Images need to be collected of the coplanar views from each camera in order to define the positions of the CCD sensors in relation to each other. The calibration block utilized in the calibration procedure is a 3D calibration block with two planes in order to satisfy the requirements of the pinhole mapping function and can be seen in Figure 2.16. The configuration of the calibration block can be observed for this experiment.

Figure 2.16: Type11 3D Calibration Block used for Stereo PIV and Single Camera PIV measurements

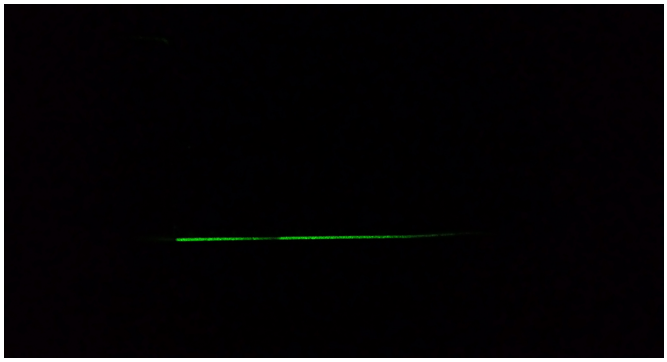

Figure 2.17: Image of the laser reflecting off the calibration surface. This figure shows what the laser would appear to look like to the naked eye in a dark environment.

As can be seen in Figure 2.16, the laser is currently located in the midpoint of the semi-major access in order to measure the flow in the mid-plane of the test geometry. Since the particles of interest will be at the plane perpendicular to the midpoint of the semi-major access, the calibration block was aligned to the required planar position parallel to the flow direction. This position of the calibration block allows us to focus on the particular plane and hence the particles that will be in the plane of flow. Once the position for the calibration block was secured, adjustments for the laser were made to ensure the plane of focus is coplanar to the plane of the laser. Due to the harmful intensities of the light emitted by the laser, when performing the calibration procedure, it is mandatory to use safety goggles designed to specifically filter wavelengths of light that are produced by the Nd:YAG laser emissions. This makes performing the steps above rather challenging as the majority of the laser emissions is blocked by the glasses. In order to prevent reflections and indirect exposure, it is recommended that they do not be removed during periods of emissions and that all participants face away from the laser emissions during the experiment. While performing the calibration procedure, using an orange surface will reflect the laser emission in the wave length that can be safely visible with the safety glasses on. This allowed for the easy viewing of the laser plane and the translations made while moving the laser into the correct location.

The images used in calibration procedure are taken from both cameras at their current orientation to the calibration block in the laser plane. In order to acquire these images, the cameras must be set to single frame/single exposure mode or the expose time will be too short to create an image of the configuration. Its import to place the calibration block in the same respective position to the camera viewing area. This was adjusted and optimized by performing multiple high frequency image ”grabs”. This process continuously refreshes the viewing area of the camera field of view and presents the images as a movie in real time which allows for any changes to be recognized as they are being made to the camera’s orientation. After the calibration images have been acquired, it is required that the marks on the calibration plate be

marked in the field of view in order to establish the dewarpping function. This is performed on all views for each camera being used. In the stereoscopic configuration using two camera and one 3D calibration plate, this requires running the mark definition batch process twice, one on each image of the calibration block for the images taken by each camera. In order to perform this procedure, three marks are selected in order to establish the position and spacing between each mark. Once three marks have been selected on each calibration image, another batch process is run to find the remaining marks in the image area. It is recommended that at least 20-30 marks be identified in the calibration of the cameras and more is encouraged. Due to the nature of the pinhole dewarping function selected, it is not required to identify calibration marks in the entire viewing area.

After identifying the remaining marks of the calibration plate, a dewarping mapping function is performed to the marks of the calibration block identified in each image from both cameras. In this step, the mapping function for the calibration was selected to be the camera pinhole model. After the mapping was completed a table displaying the average deviation of the positions of the dewarped marks to the ideal grid are displayed for both cameras. This allows for adjustments and recalibration if the values are out side of the acceptable range. Any values reported under 1 are acceptable and under .3 are regarded as excellent. Values higher than 2 pixels are considered questionable and should be reevaluated. The last step of the calibration procedure is the evaluation of the corrected images from the fit mapping. Once the fit mapping procedure is complete, the images from both cameras are overlaid in order to visually inspect if the views of the corrected images coordinate systems coincide. Additionally, the grid marks are overlaid as well in order to inspect whether the grid marks align with the regular grid created.

2.5 PIV Vector Field Analysis

2.5.1 Image Preprocessing

In order to translate the digital images into vector maps, preliminary image preprocessing is required in order to ensure the best results can be achieved. Calculations of stress and strain in the field of flow its a two-step process that ultimately relies on the quality of the vector calculation, or the displacement of a particle between two images. Any subsequent flaws in the vector analysis will propagate to the corresponding analysis that relies on such data. Image preprocessing allows for the manipulation of the collected images before the vector analysis is performed. In this experiment, several preprocessing techniques were initially tried but only two yielded the most favorable results. Similar to a high pass filter where large intensity fluctuations of the background are removed from the images, high pass filter is accounted for using all 400 images and applied to each one individually during the vector calculation procedure.

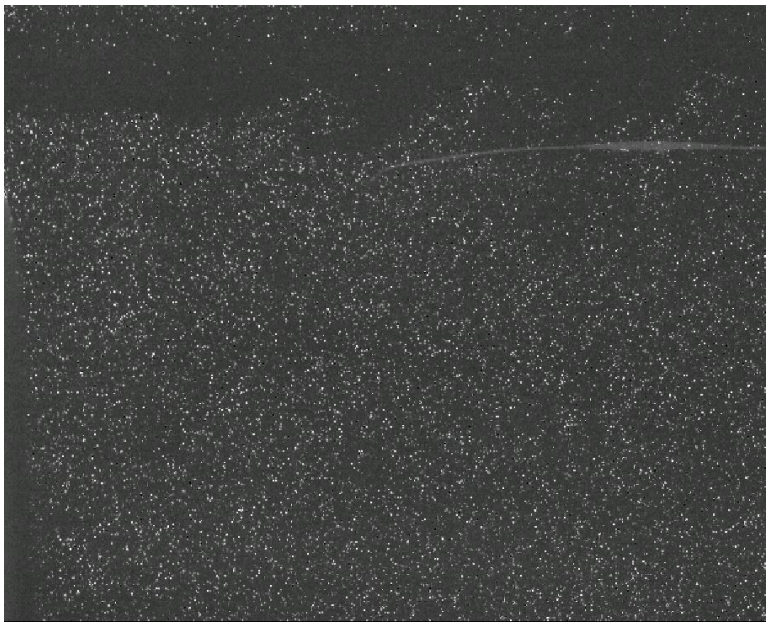

Figure 2.18: PIV of the Jet Boat Tail Mirror without any image preprocessing.

This particular filter focused on the removal of the local background intensity level by creating an image representing the average of background intensities of which the instantaneous images would then subtract to form the final PIV image. This allowed

the smaller particles which otherwise would have been overpowered by the high intensity backgrounds to be observed more clearly and used in the vector field calculation. Figure 2.18 shows a typical image collected through the PIV. Although the particles in the image appear to be seen clearly, there is a noticeable hue to the background when compared to Figure 2.19. It can be observed that background intensities have been removed and the intensities from the particles are more easily and clearly defined in the image.

Additionally, particle intensity normalization is performed in order to correct for localized intensity fluctuations. This preprocessing function was found to work the most optimally with the subtract feature in providing reliable vector plots.

Figure 2.19: PIV of the Jet Boat Tail Mirror after image preprocessing.

Intensity normalization is also commonly known to be very effective on particle images with a high intensity fluctuation from varying seeding densities during the experiement or the result of multiple reflections. This processing technique relies on a scale length of pixels over which to apply the normalization algorythm. For the experiments performed in the laboratory a scale lenghth of four to eight pixels was observed to provide the best normalization results. Value too high would take into account intensities form neighboring regions and resulted in the particles near the boundary regions of the mirror surface to appear as a lower intensity. Optimization of

the normalization perameter is unique to the experiment that the technique is being applied to. Several pixel scale values were tested and evaluated in order to ensure a proper value had been selected.

2.5.2 Vector Calculation

Vector calculations were performed using a multipass cross-correlation / stereo cross-correlation method using second order correlation with decreasing window size and round Gaussian weighting functions for both interrogation window passes. Whittiker image reconstruction was also used. In each calculation a mask was created to omit regions of interest that were occupied by the mirror body or shadows from the direction of the laser. Figure 2.20 is an example of one mask applied to the PIV data being evaluated.

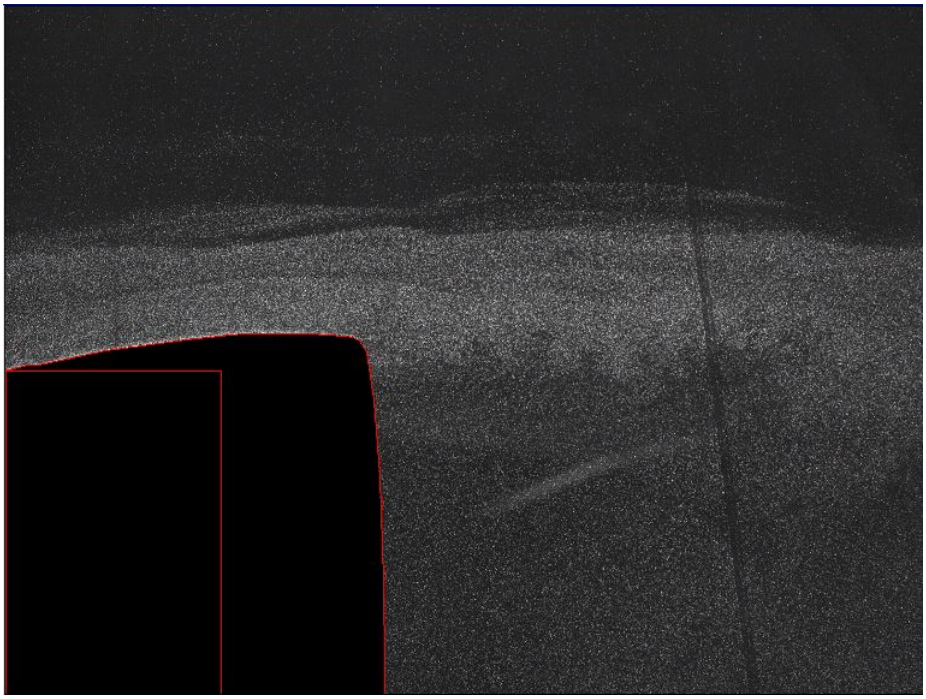

Figure 2.20: An example of a mask used for PIV measurements.

In order to perform the cross-correlation analysis on the digital image acquired from the PIV experiment, each image from both cameras is divided into corresponding interrogation windows in order to identify the particles position and their corresponding displacements. We can determine the instantaneous velocity component

for the interrogation windows under investigation by estimating the spatial averages of the particle displacements. The cross-correlation function evaluates the local intensities inside the windows defined for the multi-pass approach by evaluating the local intensities for the corresponding image pairs. The second image is shifted with respect to the image intensities of the first image so to align the peak intensities and obtain a displacement vector [16]. The corresponding displacement vector is the displacement of the image in order to align the intensities of the region. Once the largest peak is located and it is found that the resulting peaks don't correspond to the same velocity, the average utilized in the vector velocity for the particles within the interrogation area. Such a method is susceptible to false correlation peaks as well which could presents errors in the data shift in the form of noise. False peaks from dissimilar particles overlapping in various location in the viewing area can cause false positives in terms of the correlation analysis. In such a case, the shift calculated is affected and the resulting velocity vector is subjected to higher signal to noise ratio [16]. Additionally, the out of plane displacement component of the flow field can also cause an effect where particle pairs are lost as they exit the laser sheet. Between exposures, this would result in both particles entering and leaving the interrogation windows and will cause the cross correlation of the two images to consist of false peaks as well. This effect can be mitigated by limiting the maximum particle displacement relative to the field of view of the measurement in order to limit the out of plane component associated with the measured displacement.

Once the interrogation windows has been processed, the analysis is shifted across the image domain based on predefined inputs. For the experiments performed in this analysis, the interrogation window shift was kept constant and a 75% overlap was used in order to increase the spatial resolution of the computed vector fields. For the data evaluating the jet region in detail, an initial pass of 64x64 interrogation windows was selected and a final pass of 32x32 was performed as well. This configuration allowed for higher spatial resolution needed to resolve the velocity gradients of the recirculation region without generating noise in the vector plots.

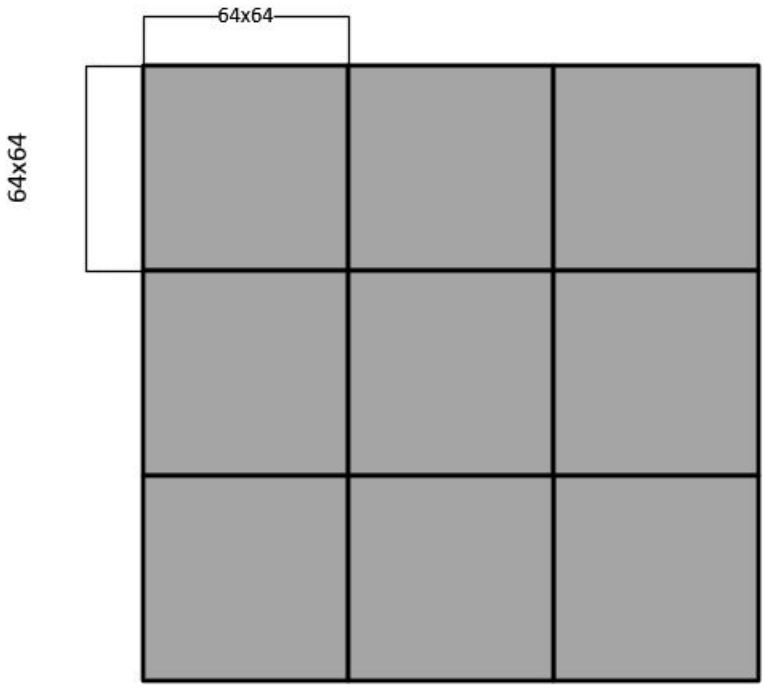

Figure 2.21: Interrogation window size of 64x64.

Figure 2.21 displays the interrogation windows size for the initial pass using 64x64 pixels with 0% overlap. During the vector field evaluation, the correlations only factor the intensities that are within the boundaries of the specified windows size. Each interrogation window is evaluated once and depending on the windows size and overlap, is shifted to the new location. This sequence is repeated until the entire field of view is evaluated and is performed twice in the initial vector calculations. Although performing a decreasing size and multi-pass correlation will increases the computational time, the increase in resolution allows for the better interpretation of the gradient field measured. The overlap is defined as the percentage of the interrogation window area that will overlap its neighboring interrogation windows. A higher interrogation window overlap will decrease the overall window shift for the corresponding pass. With a larger window overlap, a higher percentage of the interrogation window will be shared which results in a closer grid spacing and increased spatial resolution. For a camera with a CCD pixel resolution of 1600 x 1280, 64x64 pixel interrogation windows will result in 475 vectors being calculated. By increasing the region of overlap to 50%, the effective pixel shift is reduced to 32 pixels

and thus the position of the vector location on the grid is shifted over in increments of 32 pixels for subsequent interrogation windows. For an interrogation window size of 64x64, this results in a larger amount of vectors to be calculated and hence an increase in the vector density. By increasing the interrogation window overlap to 50%, the same 1600x 1280 CCD sensor will now be evaluating a vector field consisting of 825 vectors. Utilizing a decreasing multi-pass correlation method with a final interrogation window size of 32x32 with 75% overlap allows for a final vector resolution of 31,262. These two features are the dominating parameters that define the grid size and hence the spatial resolution of a vector field. Although the same vector count could be achieved through smaller interrogation windows, using window overlap instead will provide the spatial resolution desired without negatively affecting the signal to noise ratio commonly associated with reducing the window size to drastically.

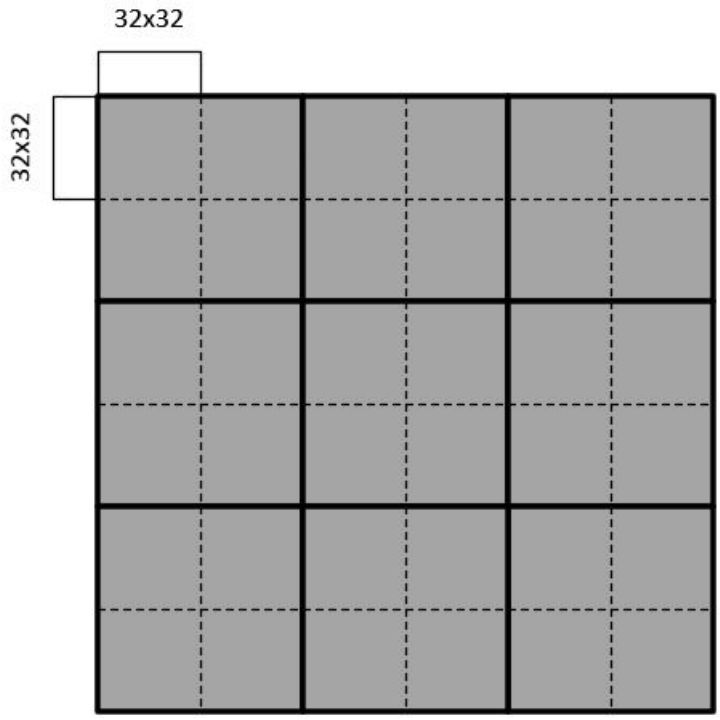

Figure 2.22: Interrogation Window size of 32x32 pixels with 0 percent overlap. This figure displays how spatial resolution can be increased via a multi-pass cross correlation method with decreasing windows size.

For the initial pass of the vector calculation, the ”Standard I1*I2 (via FFT, no zero-padding)” algorithm was chosen. This function uses a standard cyclic Fast

Fourier Transform based algorithm to evaluate the correlation of the interrogation windows of the field of view. The I1 and I2 are the intensities of the two interrogation windows which is applied over a 2D array as can be seen by the equation below by equation 2.1.

$$C((dx, dy) = \sum_{x=0,y=0}^{x<n,y<n} I_1(x, y)I_2(x + dx, y + dy), \frac{n}{2} < dx, dy < \frac{n}{2} \tag{2.1}$$

The 2D array will calculated the strength of the correlations corresponding to the displacements within the two interrogation windows being evaluated. The cyclic nature of the algorithm suggests that the image correlation is evaluated as though the interrogation window is repeated aiding in the vector calculation. In order to perform this calculation of the two interrogation windows, an inverse FFT will be calculated allowing for the correlation function to produce a displacement result. Although faster than the computing the correlation directly, it does come with computational costs. As a result of the cyclic correlation function, a weighting of the correlation coefficients which favors the smaller pixel displacements is introduced to the vector calculation. In order offset these effects larger interrogation windows should be used so that the pixel displacement is not too large relative to the region being interrogated. This is also another reason to support the practice of using larger overlap regions rather than interrogation windows insufficiently sized interrogation windows to increase the spatial resolution. Another byproduct of the cyclic correlation function is its tendency to display a bias towards smaller displacement calculations. This will cause pixel displacements to be observed as smaller than they actually are. Peak locking can also be observed as well. This is a phenomena in which the particle shift will appear to be slightly favoring the next integer. Second Order Correlation is a multi-pass approach that can be used to increase the accuracy of the initial pass for the cross-correlation analysis. The function operates by shifting each window a quarter of the interrogation windows size so that the overlap between the two respective windows is 50% of the viewing area. Once correlations for both shifted windows are calculated, they are

multiplied to increase the correlation peak and filter out the random peaks of the two regions. This method usually leads to more accurate results with less false vectors. Whittaker Image reconstruction is also employed in order accurately measure the correlation peaks with sub pixel accuracy.

During the vector calculation, validation measures can be imposed on the calculated vectors before its used as a reference vector for the following subsequent passes. These measures are very similar to the measure that are performed after the final pass for the vector calculation. Median filters were used to eliminate spurious vectors from the final vector field. This algorithm calculates the median value for each component of flow from the surrounding 8 vectors of a middle vector and compared the values to the vector of interest. The vector of interest is rejected if it is outside the boundaries defined in equation 2.2, 2.3 and 2.4. The standard deviation of each of the components of velocity are used to compute an acceptable range for each components of flow and reject vectors that don't satisfy the criteria imposed on the calculations. The above approach is augmented by the Lavision software to first validate the surrounding vectors before they are used to compute the median for the vector of interest. If one the surrounding vectors is found to be a spurious vector, it is replaced by a vector from one of the three highest correlation peaks and is used instead.

$$U_{median} - U_{rms} <= U <= U_{median} + U_{rms} \tag{2.2}$$

$$V_{median} - V_{rms} <= V <= V_{median} + V_{rms} \tag{2.3}$$

$$W_{median} - W_{rms} <= W <= W_{median} + W_{rms} \tag{2.4}$$

U_{rms} is calculated from the equation 2.5

$$U_{rms} = \sqrt{\frac{1}{N-1}\sum_{i=1}^{N}(U_i - U_{median})^2} \tag{2.5}$$

The median filter will allow the large outliers at either end of the spectrum to be neglected as the median value will be considered instead of the average. Additionally, the two largest outliers are neglected for the standard deviation calculation as well so that their influence will not cause larger value than is necessary for correct results. An additional post processing filter that was employed was the Remove Groups filter. This filter allows for the removal of groups of vectors that fall outside the acceptable range desired and can be useful in vector processing with regions of large overlap. This filter is useful when large groups of vectors are not be removed by the median filter due to its dependency of the surrounding 8 vectors and their corresponding median. This filter allows for the removal of groups of spurious vectors that do not have a number of corresponding similar vectors in the surrounding area. Due to the nature of the flow and the large gradients of the shear layer in the recirculation region, this filter has to be applied carefully to prevent the removal of valid vectors in the interrogation window.

2.5.3 Proper Orthagonal Decomposition

This section gives a thorough description of the Proper Orthogonal Decomposition analysis on data obtained through PIV experimentation. The derivation of the modal decomposition is based on the method developed by Sirovish in 1987 as a means of calculating the corresponding Eigenvalues and spatial Eigenfunctions for the vector fields using a large number of image samples in order to construct a low order model of the flow field. The analysis is used to describe the dominant behaviors of the flow field under investigation[2,14]. Each vector field is used to create the coordinate system in which the velocity field is optimally representing the vector field. Each Eigenvalue has an associated energy value which can be found from the orthonormal basis function

$$\lambda_k = \sum_{i=1}^{M} (u_{ij} a_k)^2 \tag{2.6}$$

in which the function solution is ordered in decreasing value from high to low. The first couple of modes can usually be observed to contain the highest level of energy associated with the vector fields. The POD modes can be considered to capture the deviation of the velocity vector from the mean flow component. This feature will allow us to investigate the evolution of time resolved coherent structures of the PIV data and associate them with the eigenvalue modes associated with the behavior. The Eigen functions in this method are referred to as $\Phi^{n}(X)$ that are evaluated from a sequence of N_t PIV velocity vector fields or snapshots represented by a matrix function: $V(X_{ij},t_k)$, where i = 1 ... n_x, j = 1 ... n_y, k=1 ... N_t.

We are looking to solve for an eigenvalue function for the velocity field that can be decomposed to the form as follows

$$u_n(x) = \overline{u(x,t)} + \sum_{k=1}^{N_t} a_{nk}\Phi_k(x); n = 1, ..N_t \tag{2.7}$$

In this relation, $\overline{u(x,t)}$ is the average velocity component and $\sum_{k=1}^{N_t} a_{nk}\Phi_k(x)$ are the instantaneous values associated with the total velocities which can be considered as

$$u'_n(x) = \sum_{k=1}^{N_t} a_{nk}\Phi_k(x) \tag{2.8}$$

which we can rearrange

$$\Phi_k(x) = \sum_{k=1}^{N_t} b_{nk}u'_n(x) \tag{2.9}$$

where Φ_k are the eigenfunctions that comprise the POD modes and are chosen to be orthonormal as showns by the relation

$$\int_D \Phi k \cdot \Phi(l)dx = \lambda_k\delta_{kl} \tag{2.10}$$

which can also be seen as

$$\Phi^T_{kp}\Phi_{pl} = \lambda_k\delta_{kl} \tag{2.11}$$

Using the PIV vector field we can now calculate the velocity correlation matrix using the velocity field data for each component of flow. The correlation matrix is then used to solve the classic eigenvalue problem represented by the equation

$$Cb = \lambda b \tag{2.12}$$

where λ is the eigenvalue matrix and b are the corresponding eigenvectors for the solution. Once the POD coefficients are solved for, the velocity fluctations relative to the to the POD modes can recontruccted fom the following relation

$$u_n(x) = \overline{u(x,t)} + a_{nk}\Phi_k(x); n = 1, ..N_t \tag{2.13}$$

2.5.4 PIV Uncertainty

This section is dedicated to the procedure used to calculate the relative uncertainty of PIV performed in measuring the flow field. The PIV laboratory system is an ensemble of different sub systems which includes the wind tunnel and the numerous sensors used to calculate the wind tunnel test section speed. The procedure for PIV uncertainty analysis was followed according to the International Towing Tank Conference Recommended Procedures and Guidelines for Particle Image Velocimetry which was proposed by the Visualization Society of Japan [17]. In order to correlate the particle position in the image plane to the true spatial plane, a calibration is performed to translate the measured particle displacements in terms of pixel length units to mm. The uncertainty associated with this procedure consists of an uncertainty of the measured reference points, the uncertainty associated with the calibration board manufacturing, the image distortion of the lens for the camera, the image distortion of the CCD chip, the position of the board in reference to the laser light sheet and the uncertainty associated with the angle of the calibration board to the plane of the laser. The summation of these uncertainties results in the RMS uncertainty for the Magnification factor which will be a component of the combined uncertainty for PIV

velocity measurement.

For the uncertainty of the reference points measured on the image plane, we can assume the total uncertainty to be .7 pixels as recommended by the procedures [17] and guidelines and for which the sensitivity factor can be calculated as

$$\partial/\partial L_r = -l_r/L_r^2 \tag{2.14}$$

The physical distance measured for the length of the reference points will attribute to the uncertainty of the magnification factor as well. The precession calibration board utilized in our experimentation contained less than 20 μm of error [17] with a sensitivity factor found by the equation

$$\partial\alpha/\partial l_r = 1/L_r \tag{2.15}$$

The image distortion by the camera lens was also taken into consideration in the calculations as well as it can affect the calibration results and was recommended to be .5$\%$ of the total length of the image or .005L_r and the sensitivity factor can be calculated by the relation in equation 2.14 [17]. Additionally, the position of the calibration board offset from the actual position of the light sheet was considered and evaluated in terms of a Δz translation of the vertical image plane. There is no accurate way to physically measure this value but it can be assumed that a difference of Δz = .5 mm in direction of the z axis can attribute to the total uncertainty of the measurements [17]. The associated sensitivity coefficient can be calculated by the relation

$$\partial\alpha/\partial l_t = l_r/L_r \cdot l_t \tag{2.16}$$

In addition to error being associated with the parallel position relative laser plane, an error can also be attributed to an offset angle of the calibration board in reference to the laser plane. Although great care was taken to ensure that the calibration board was positioned to be parallel to the laser plane, we can assume that an angle of 2° is present in the measurement deviation from the true plane which

translates to .035 radians from the parallel [17]. The sensitivity factor can be calculated from the relation

$$\partial\alpha/\partial\theta = -l_r \cdot \theta/L_r \tag{2.17}$$

Laser spatial and temporal power fluctuations were also considered in the uncertainty calculations for the PIV measurements of the particle displacement. This uncertainty can evaluated as the distance traversed by the particle over the time interval of the experiment, Δx. The sensitivity factor for the uncertainty attributed by the laser power fluctuation can be calculated as

$$\partial X/\partial x = 1/\alpha \tag{2.18}$$

A particle mismatch error was also taken into consideration for the total uncertainty of the experiment. This occurs from the incorrect pairing of particles in image pairs and can usually be filtered by techniques such as the median filter mentioned in the previous subsection. If the error attributed to the mismatching of particle pairs is relatively small, the error will not be detected by the median filter and can assumed to be .2 pixels. Also, the uncertainty from errors in sub-pixel PIV analysis can be assumed to be.03 pixels [17] and is dependent on many factors such as particle concentration and noise of the image pairs [17]. The sensitivity coefficients for both uncertainties will be considered to be 1.0 as recommended by the guidelines. The delay generator and pulse time uncertainty can be found from the manufacturer of the laser subsystem as this will depend on the Q-switch in addition to the timing hardware of the of the laser system. For the Lavision Nano series PIV laser, the timing jitter is listed to be .5ns and can be used for both delay generator and pulse timing uncertainties.

The particle trajectory will be highly dependent on the buoyancy of the particle in air, flow direction and the particles resistance to the changing directions of the fluid. Since the tracer particle is neutrally buoyant, we can assume that the error from its

resistance to changing directions can be considered less than .01% of total velocity as stated by the guidelines [17]. An additional uncertainty for the three dimensional effect of the viewing perspective should also be taken into account as well. The out of plane component of flow will contribute to the total component measured and can be seen by the relation below, where w is the component of velocity normal to the free stream. The perspective angle can be found from the calibration data for each camera.

$$u_m = u + w \cdot tan\theta \tag{2.19}$$

The uncertainty for the center position of the correlation area has a maximum uncertainty of .5 pixels. The sensitivity coefficient can be calculated by

$$\partial x/\partial X = \alpha \tag{2.20}$$

The correlation of the physical measurement on the image plane can also attribute to uncertainty for the experiment. It can be assumed that the uncertainty can be within the range of 2 pixels and the sensitivity coefficient can be found from the equation 2.18 [17]. The uncertainty values presented here are utilized to calculate the total uncertainty relative to the measurements of the velocity, the displacement and the measured time interval of the PIV experiment independently. Using the above method, the total uncertainty for the PIV experimentation can be seen in Table 2.4.

Wind Tunnel Test	Camera 1	Camera 2
Baseline / Jet1 Wake Profile	3.75%	3.75%
Jet2 Wake Profile	3.74%	3.74%
Baseline / Jet1 Trailing Edge	3.70%	3.71%
Jet2 Trailing Edge	3.74 %	3.74%

Table 2.4: Table of PIV Uncertainties

Chapter 3

Results

3.0.5 Full Wake Velocity Profiles and Streamlines

The effects of the passive jet can be observed in the plots of the full wake profile for the three models tested. Shown below in Figure 3.1 - Figures 3.3, Jet1 and Jet2 effectively reduce the size of the wake region and also truncate the length of the recirculation region as well. The velocity profile plots show a noticeable contraction in the velocity magnitude of the recirculation region for both models using the JBT flow control. Of the two JBT models, the Jet2 configuration displays a larger reduction in the recirculation region area. The velocity profile plots also indicate the Jet2 configuration achieves a smaller velocity profile through a lower velocity delta at 1.5 mirrors lengths from the rear surface of the models. At 1.65 mirror lengths downstream, the Jet1 velocity profile as seen in Figure 3.5 indicates both models have almost identical velocity profiles downstream. This suggest the entrainment efficiency of the Jet1 configuration is higher than that of the Jet2 configuration despite the recirculation region being larger for the Jet1 model. Another observation of the differences in the wake profile is in the convergence behavior of the Jet1 wake when compared to the Jet2 model wake. The Jet1 model has a higher rate of convergence which can be observed by the slope streamlines as they seem to converge at the end of the recirculation region and proceed to flow downstream. It can also be observed that the streamlines converge to a narrow end point region when compared to the Jet2

configuration, which allows for a smaller wake area reduction. This behavior is not as pronounced in the Jet2 profile streamlines which are seen to flow parallel to the downstream direction as it progresses past the end of the recirculation region. These characteristics contribute to the velocity profiles recorded in Figure 3.4 and Figure 3.5.

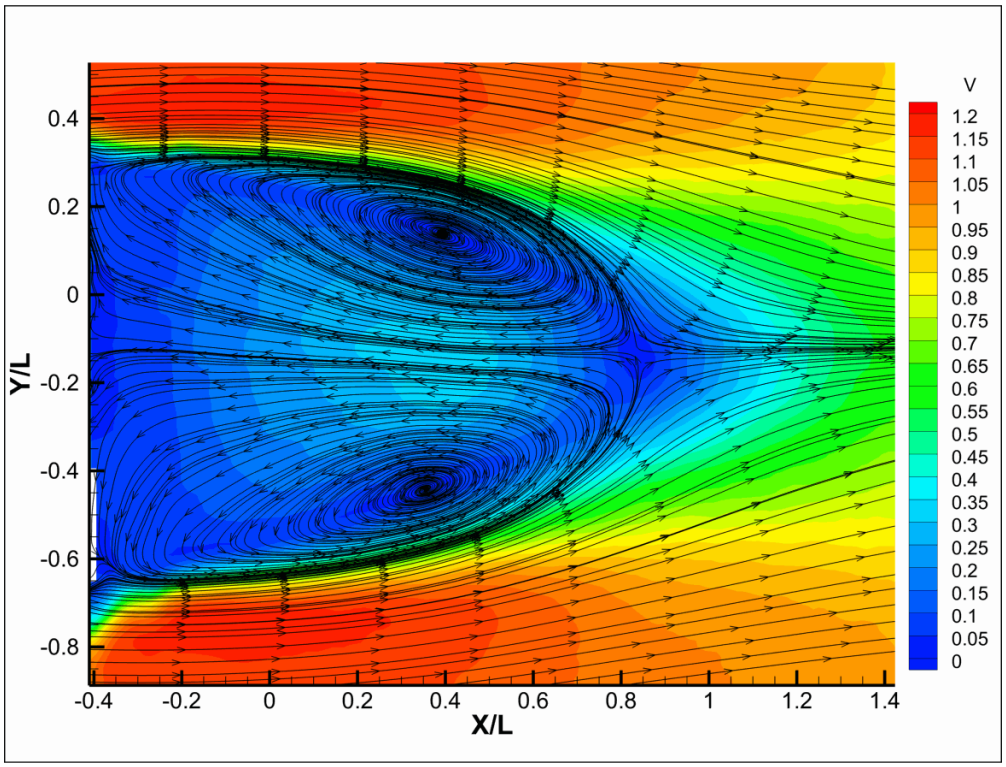

Figure 3.1: Mean velocity streamlines and contours for the Baseline model in the vertical symmetry plane of the wake. V= 30 m/s Re = 2.55×10^5.

The recirculation region also displays noticeable traits from the JBT passive jet interacting with the free stream shear layer. Comparing all three models, the Jet1 design has the largest reduction in the recirculation velocity as can be observed in the velocity contours of the recirculation region. The recirculation region for the Jet1 model displays a contraction of the streamlines along with a reduction of the velocity which can be observed by the velocity magnitude contour of .3V normalized to the free stream velocity recorded. The high velocity area of the recirculation region is not only smaller but also displays a lower magnitude when compared to the baseline model. As can be more clearly observed in the figures of the V_x velocity contours, the regions of high negative velocity in the recirculation region are reduced by the JBT passive flow control application.

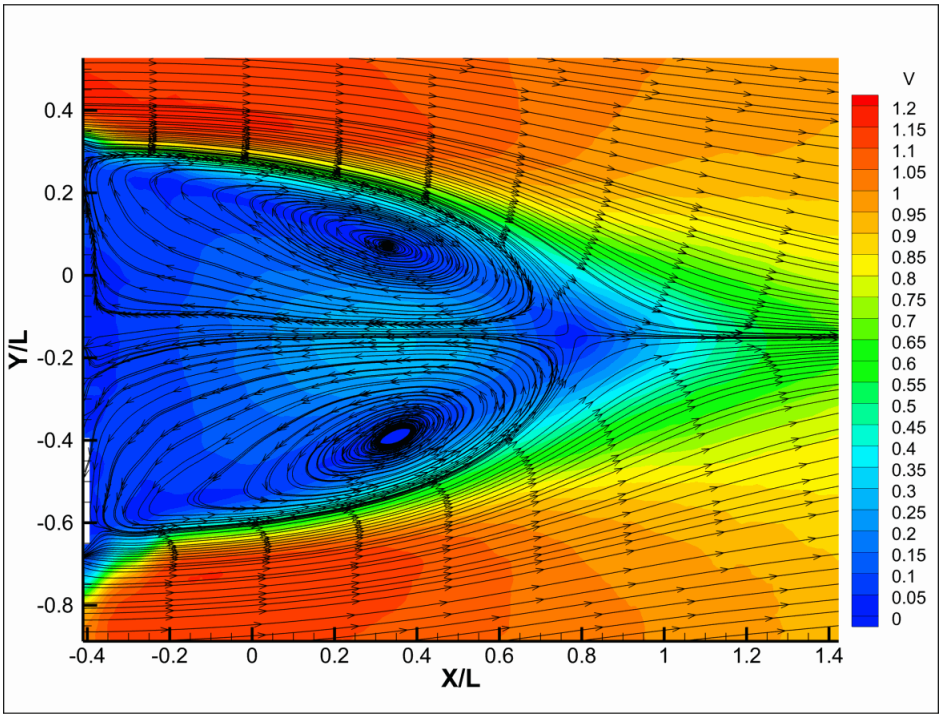

Figure 3.2: Mean velocity streamlines and contours for the Jet1 model in the vertical symmetry plane of the wake. V= 30 m/s Re = 2.55×10^5.

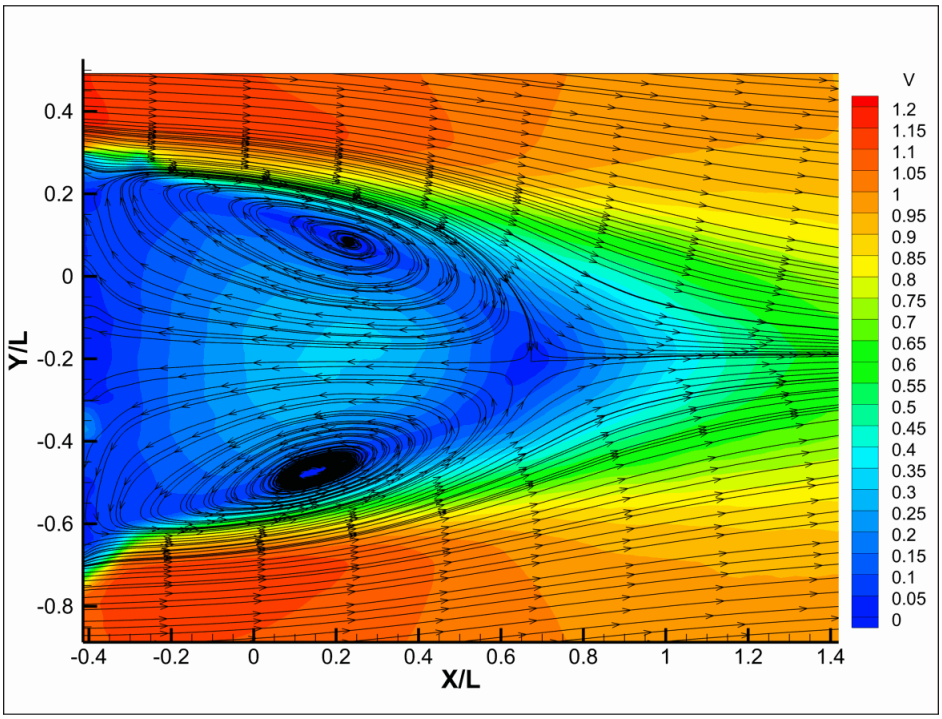

Figure 3.3: Mean velocity streamlines and contours for the Jet2 model in the vertical symmetry plane of the wake. V= 30 m/s Re = 2.55×10^5.

Although the largest magnitude recorded is still relatively large, the area of recorded high magnitude negative velocities in the recirculation region is reduced in both Jet1 and Jet2 models. The Jet1 resulted in the largest reduction of recirculation region velocity. It can also be observed that the converging shear layers downstream of the free stream stagnation point in the transition region of the wake is much narrower for the Jet1 and Jet2 models. The Jet1 model is also seen to have a narrower low velocity region despite the larger reduction in the recirculation region of the Jet2 model. The reduction in the area past the base flow free stream stagnation point displays the effects of the Jet1 model high rate of convergence and its influences in reducing of overall wake profile. The benefits of this characteristic can be seen in the velocity profiles downstream from the base area in Figure refłfig:Velocity Profile 1.5 ML and Figure refłfig:Velocity Profile 1.65 ML. Figure 3.4 displays the velocity profile of all three models at 1.5 mirror lengths and 1.65 mirror lengths downstream of the rear surface. As can be observed, the Jet1 model produces a similar velocity profile at 1.65 mirror lengths downstream, despite having a larger profile at 1.5 mirror lengths downstream when compared to the Jet2 model. This is due to unique mixing effect of the Jet1 passive jet as it interacts with the free stream shear layer. This mixing causes the mean velocity streamlines to converge at a faster rate than when compared to the Jet2 model resulting a reduced velocity profile.

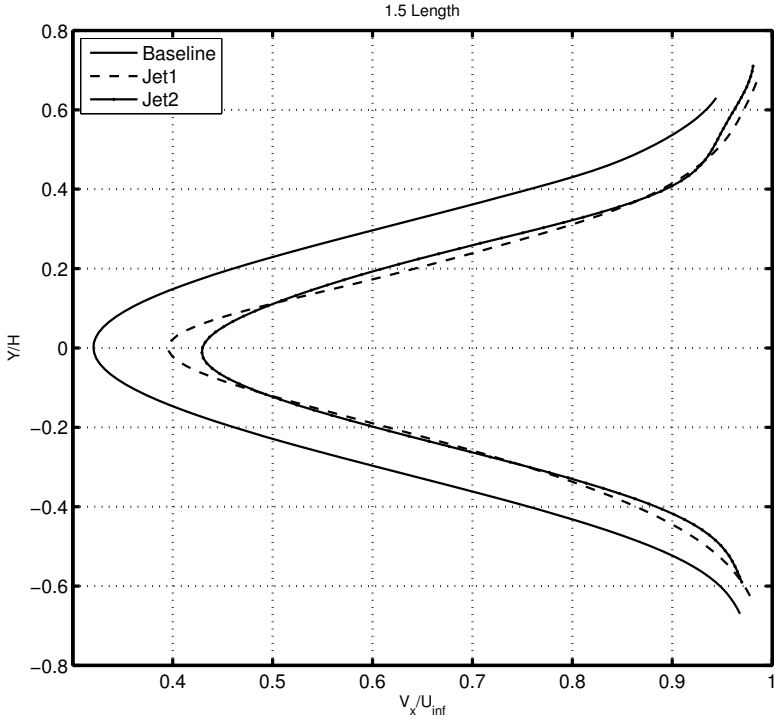

Figure 3.4: Mean velocity profile plots for all all three mirror models 1.5 mirror lengths downstream in the vertical symmetry plane of the wake. V= 30 m/s Re = 2.55x10^5.

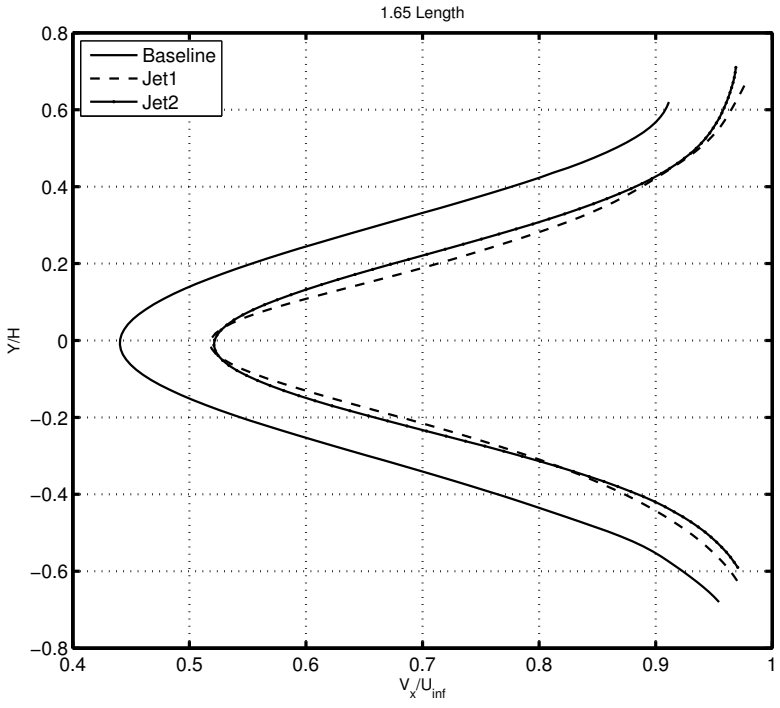

Figure 3.5: Mean velocity profile plots for all all three mirror models 1.65 mirror lengths downstream in the vertical symmetry plane of the wake. V= 30 m/s Re = 2.55x10^5.

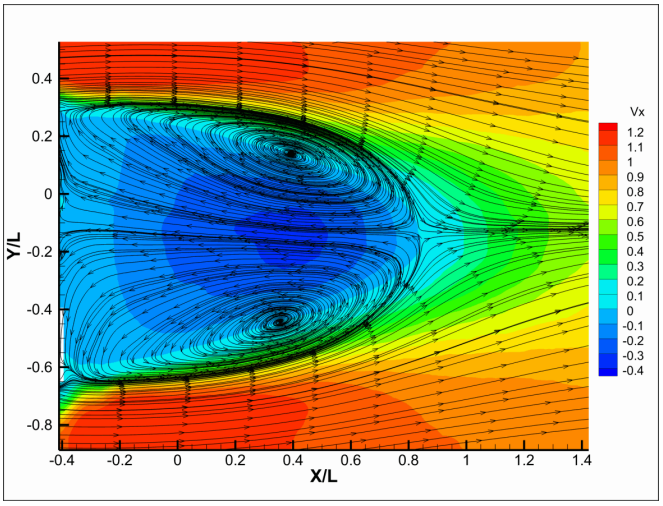

Figure 3.6: Mean Vx velocity contours and streamlines for the Jet1 model in the vertical symmetry plane of the wake. V= 30 m/s Re = 2.55x10^5.

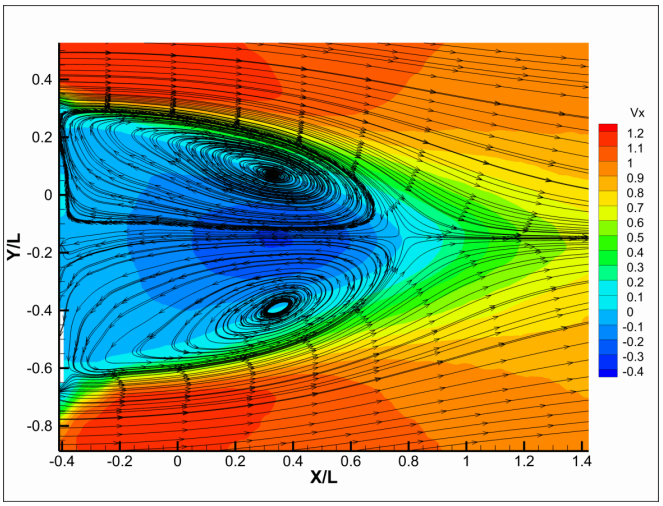

Figure 3.7: Mean Vx velocity contours and streamlines for the Jet1 model in the vertical symmetry plane of the wake. V= 30 m/s Re = 2.55x10^5.

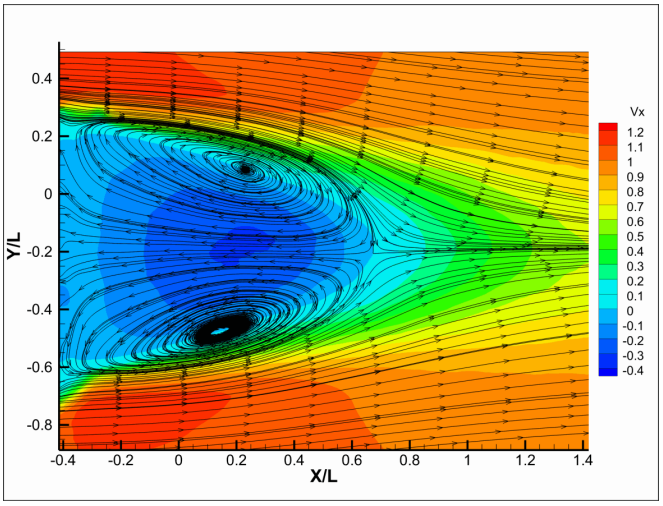

Figure 3.8: Mean Vx velocity contours and streamlines for the Jet2 model in the vertical symmetry plane of the wake. V= 30 m/s Re = 2.55x10^5.

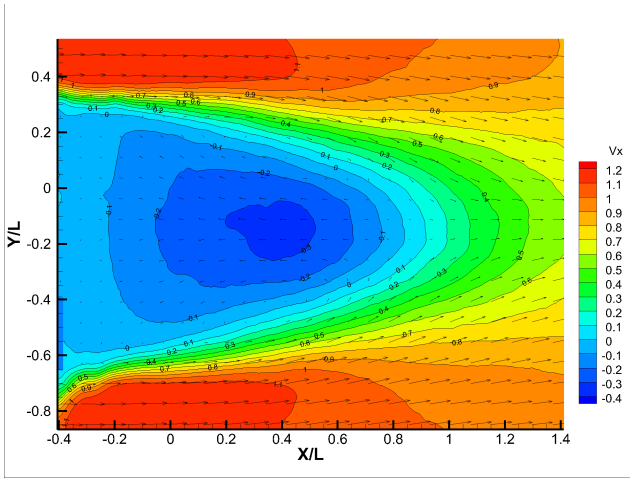

Figure 3.9: Mean Vx velocity contours and vectors for the Baseline model in the vertical symmetry plane of the wake. V= 30 m/s Re = 2.55×10^5.

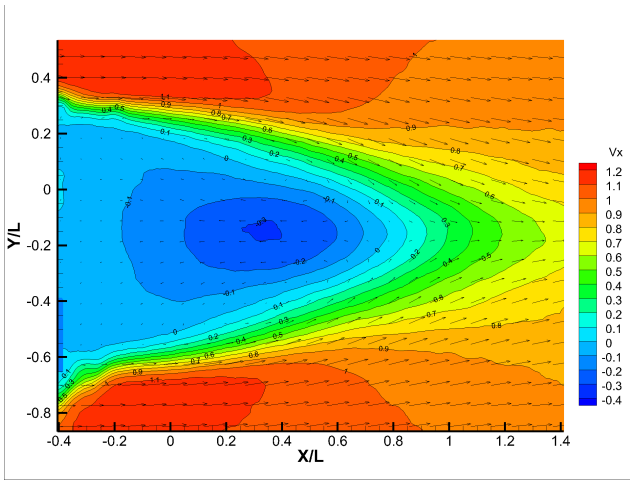

Figure 3.10: Mean Vx velocity contours and vectors for the Jet1 model in the vertical symmetry plane of the wake. V= 30 m/s Re = 2.55×10^5.

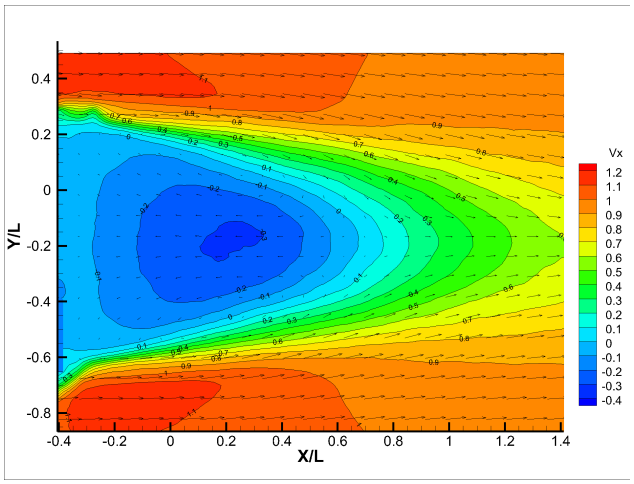

Figure 3.11: Mean Vx velocity contours and vectors for the Jet2 model in the vertical symmetry plane of the wake. V= 30 m/s Re = 2.55×10^5.

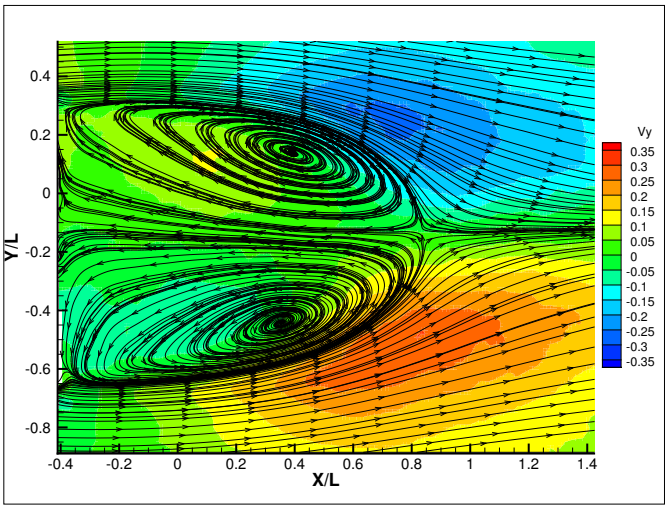

Figure 3.12: Mean Vy velocity contours and streamlines streamlines for the Jet1 model in the vertical symmetry plane of the wake. V= 30 m/s Re = 2.55x10^5.

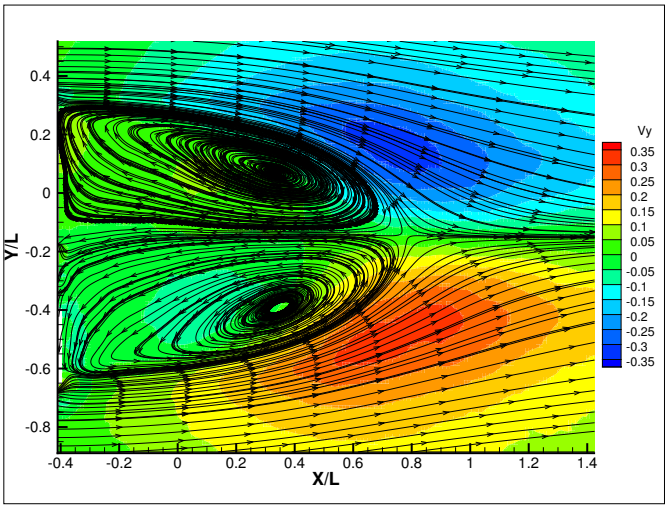

Figure 3.13: Mean Vy velocity contours and streamlines streamlines for the Jet1 model in the vertical symmetry plane of the wake. V= 30 m/s Re = 2.55x10^5.

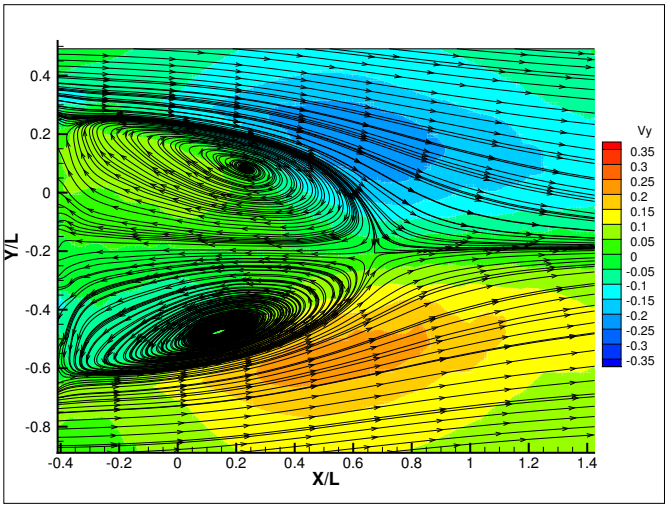

Figure 3.14: Mean Vy velocity contours and streamlines streamlines for the Jet2 model in the vertical symmetry plane of the wake. V= 30 m/s Re = 2.55x10^5.

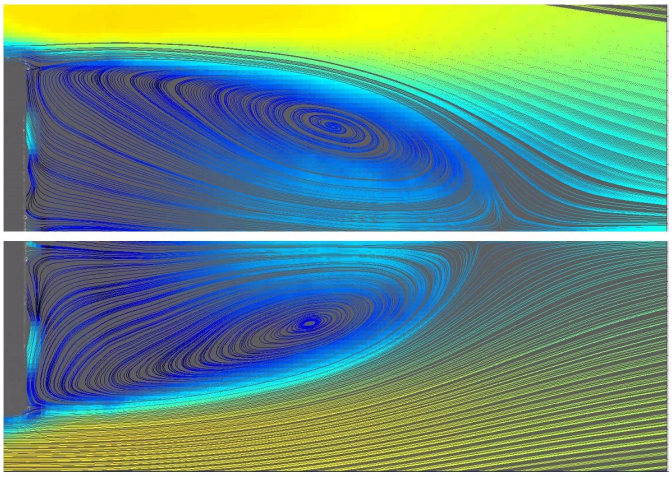

Figure 3.15: Mean Velocity streamlines displaying the difference in recirculation region lengths for both Jet1 and Baseline models. V= 30 m/s Re = 2.55×10^5.

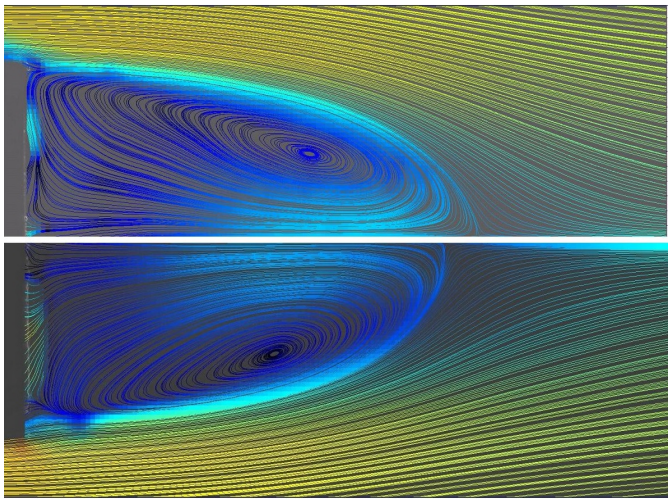

Figure 3.16: Mean Velocity streamlines displaying the difference in recirculation region lengths for both Jet1 and Jet2 models. V= 30 m/s Re = 2.55×10^5.

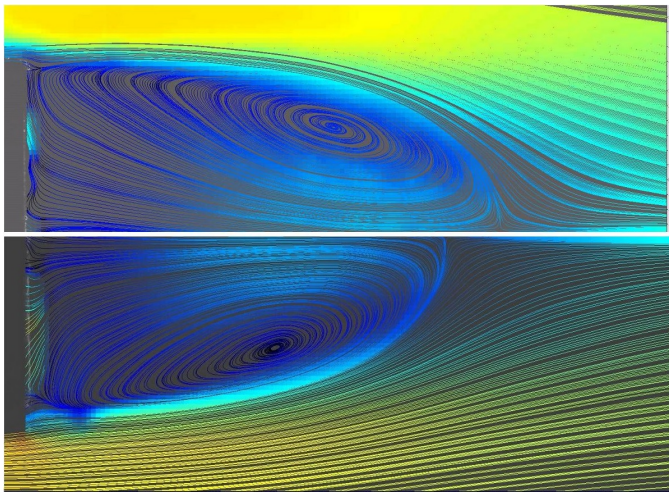

Figure 3.17: Mean Velocity streamlines displaying the difference in recirculation region lengths for both Jet2 and Baseline models. V= 30 m/s Re = 2.55×10^5.

Instantaneous Streamlines of the Recirculation Region

By investigating the streamlines for the flow of the instantaneous velocity measurements, the differences in the flow behavior on smaller scales can be seen, specifically the flow behavior of the base flow region. Coherent structures play a dominant role in the development of the shear layer created when the base region recirculation flow mixes with the free stream at the trailing edge of the mirror. By observing the streamlines of the three models tested, certain distinctions can be made about the augmentation each flow control model has on the baseline base flow region. It is commonly known that streamwise vorticity can be beneficial to the downstream development of a mixing layer due to its ability to enhance the efficiency of the mixing layer. The subsequent enhancement allows for what is regarded as the simultaneously occurring two dominating physical process to occur more effectively, one of which is the cascading of energy from large-scale high energy vortices to subsequently smaller scale vortices [18]. This energy transition will be continued from small scale vortices to random vortices commonly known as eddies and further down until the energy has dissipated into the main flow.

By observing the instantaneous velocity streamlines, a noticeable change in the spanwise vorticity production of the base flow mixing layer can be observed as the presence of vortices is enhanced in the flow control models when compared to the Baseline model. This is evident not only when considering the occurrence of the spanwise vortices but also the structure of the vortices that are recorded in each individual snap shot of the instantaneous flow field. Vorticity production is to be expected across all the models under investigation. Despite their presence, the flow control model enhancements can be attributed to the increased frequency and the organization of the vortices as well. Observing the baseline model instantaneous flow field, regions of vorticity can be seen in the recirculation region of the base area flow field. The vortices are a product of the shear flow in the base area as the free stream high velocity fluid is mixing with the low speed recirculation region. Although the presence of the vorticity in the base recirculation region is similar to the flow of the

Jet1 model, the organization and the development of the vorticity is not as extensive. This can be observed in Figure3.18, The instantaneous streamlines for the baseline model when compared to that of the Jet1 model in Figure3.19 can be described as having less coherent organization despite the vortices being present. Although the streamlines do not suggest direction or magnitude of the flow field for the field of view, they do suggest that the presence of stronger or more clearly defined vortices in the flow region will have a contracting effect on the recirculation region.

In addition to the contraction of the recirculation region, the convergence of the streamlines to the base flow stagnation point is observed to be enhanced with the increased presence of spanwise vorticity due to the mixing layer. The Jet1 model displays more organization and more clearly defined spanwise vortices which can be observed in higher densities within the recirculation region. The center of circulation is also very clearly defined for each vorticity in the base flow region which is noticeably different when compared to the baseline vorticity production. It is believed that this enhancement is one of the driving factors that allows for a higher degree of entrainment, allowing for the high energy free stream flow to reduce the size of the wake region as was displayed earlier by the velocity contour plots for each respective model. By increasing the presence of the vorticity in the base flow region, the cascading transfer of energy from the large scale recirculation of the base flow region into the smaller scale vortices enhanced by the mixing layer are increasing the effect of flow entrainment and energizing the base flow region. This phenomena continues from the spanwise vortices that are present in the instantaneous snapshots of the flow fields into the smaller scale vortices that cannot be rendered by the PIV spatial resolution. As a results, the effect is a smaller recirculation region, high base pressure and reduced drag.

With a higher Inlet:Outlet ratio as presented in Table2.1, the Jet2 model utilizes an increased high velocity and high mass flow passive jet in the flow control implementation, causing distinct behaviors of its own which can be observed in the instantaneous streamline of Figure 3.20. Similar to the Jet1 model, the passive jet of

the Jet2 mirror can be seen to enhance the production of span wise vortices in the base flow recirculation region. Although both models can be seen to enhance the production, the presence of vorticity is quite dissimilar in both models. The Jet2 model span wise vortices appear to be of a smaller scale with a more compact center of circulation and increased density throughout the flow field, where as the Jet1 model has larger and broader center of circulation associated with the spanwise vortices produced. Additionally, the recirculation region appears to have a increased presence of turbulence due to the high flow passive jet. These regions of higher turbulence in the recirculation region suggest the mixing layer and the concentration of vortices present are a product of the increased turbulent flow due to the high velocity passive jet. As observed in the Figure 3.1 - Figure 3.3:, velocity contour and streamline plots suggest the reduction of the mirror base flow region can be attributed to the increase in the turbulence and vorticity concentration in the mixing layer due to the implementation of the passive jet. Common to both passive jet designs, the presence of increased spanwise vortices due to the passive jet seems to reduce the area of the recirculation region with an associated truncation of the base flow stagnation point location relative to the rear surface of the mirror. Additionally, the vertical translation of the wake region in the instantaneous snapshots of the flow field suggest the passive jet improves the stability of the wake region as well.

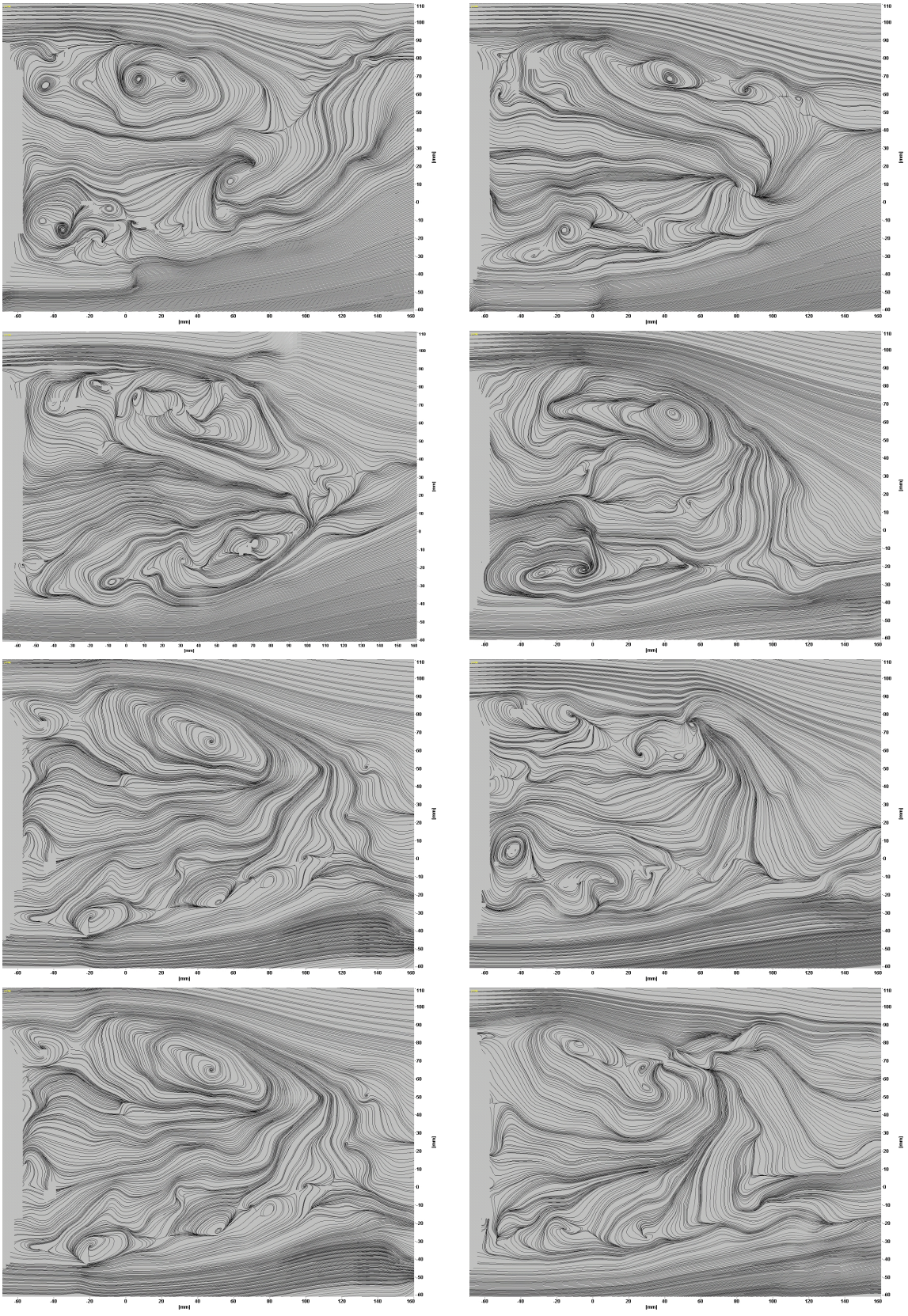

Figure 3.18: Baseline Instantaneous Streamlines displaying vorticity concentration of the naturally occuring flow in the base recirculation region.

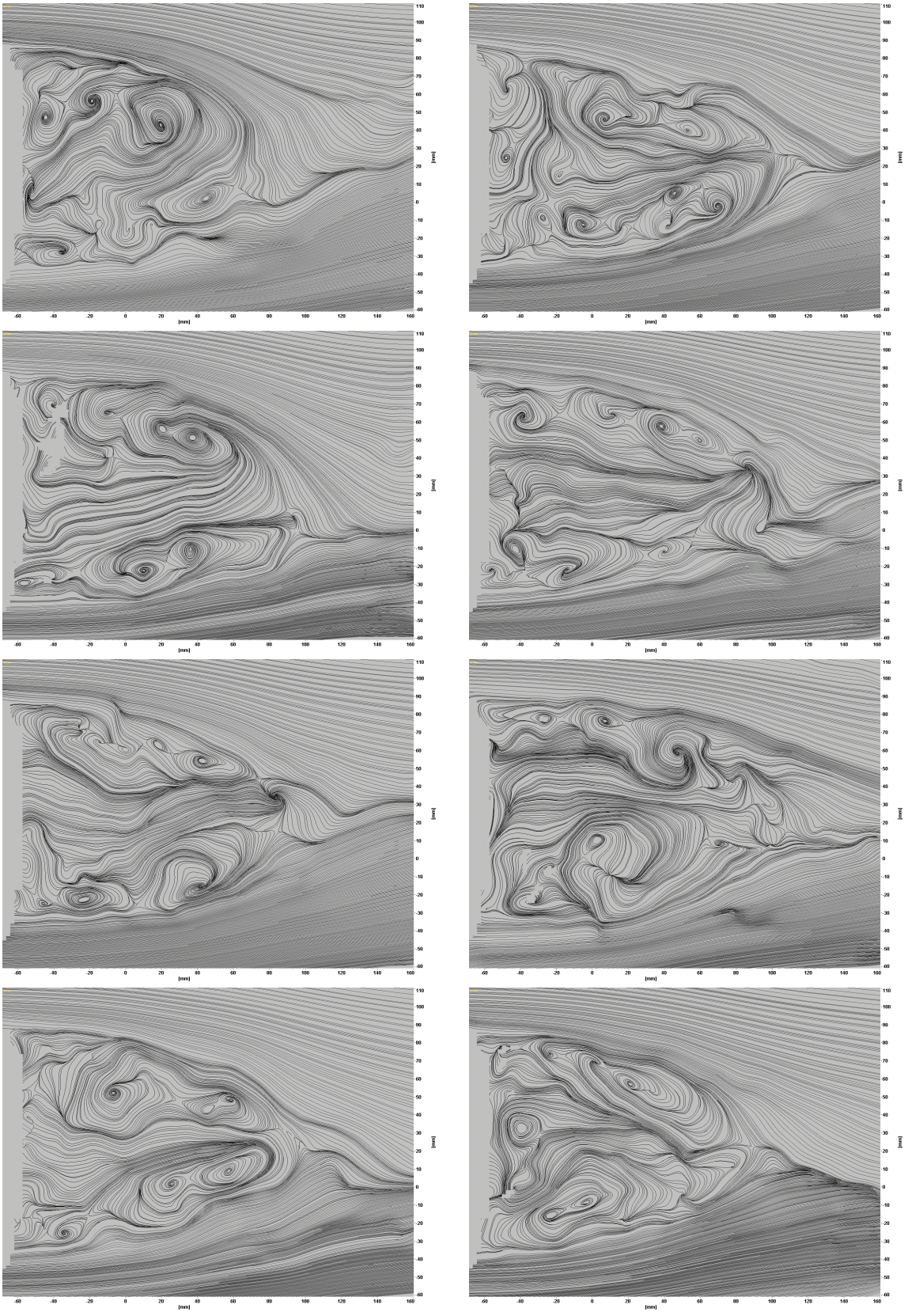

Figure 3.19: Jet1 Instantaneous Streamlines displaying vorticity concentration of the passive flow control augmented flow field in the base recirculation region.

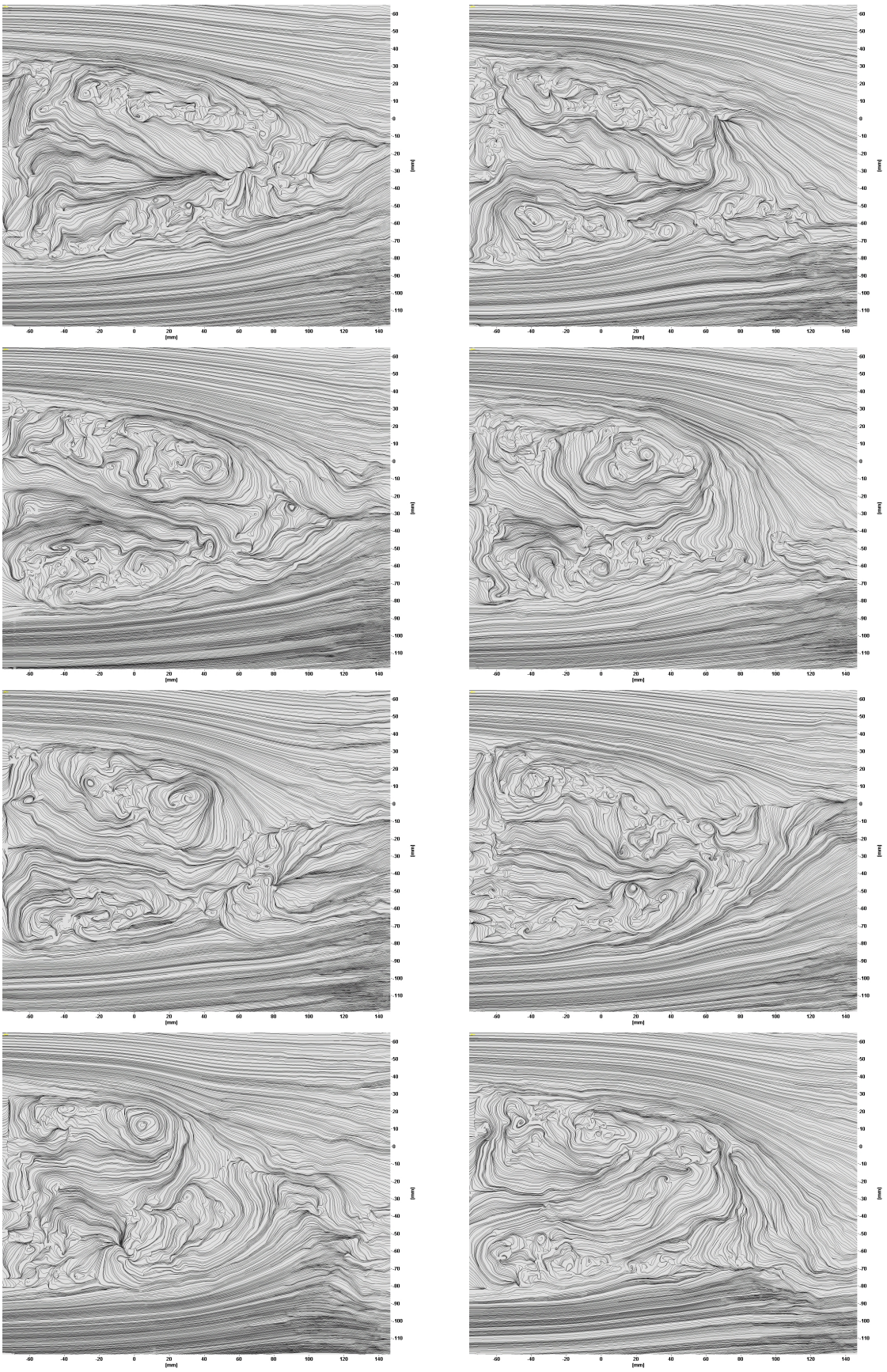

Figure 3.20: Jet2 Instantaneous Streamlines of the recirculation region displaying vorticity concentration associated with the second model using pasive flow control utilizing a higher Inlet to Outlet ratio.

3.0.6 Trailing Edge Jet Region Velocity Profiles and PIV Images

Investigation into flow field immediately behind the trailing edge of the mirror display the mixing mechanisms of the passive jet that generate the enhanced vorticity of the passive flow control base flow region. Displayed in Figures 3.21 and 3.23 are the flow behavior for the Baseline, Jet1 and Jet2 mirror designs at Reynolds number of Re = $85x10^3$. Immediately noticeable from the images for the baseline model is flow separation from the trailing edge of the mirror surface by the free stream. Additionally, as the flow moves past the mirror surface, separation occurs due to adverse pressure gradients which results in the delayed convergence of the shear layer and the free stream is observed to progress parallel to the flow downstream from the trailing edge surface of the mirror. Coherent structures can be also observed as well in Figure 3.21, showing the initiation and the type of coherent structure to be consistent for the baseline mode throughout the samples shown. These coherent structures reside in the mixing layer and can be observed to initiate at relatively the same distance each time they occur. Additionally, these structures display a natural curling shape common with unforced shear layer coherent structures between two fluid with different velocities, $U_1 > U_2$.

Figure 3.22 shows the passive flow control jet and its effects on the free shear layer as it flows over the surface of the mirror. From the PIV images displayed, it can be observed that the passive jet instigates enhanced vorticity in the mixing layer as can be seen through the altered cohere structures at the intersecting point in the base flow region. These coherent structures are no longer consistent with the unforced coherent structures present in the baseline model flow field and now show a structure that is consistent with a coherent pairing process. After the high kinetic energy free stream fluid enters the inlet of the Jet1 passive flow control mirror design its is accelerated through a converging nozzle and ducted out at an angel of 7° to the free stream flow towards the center of the recirculation region. Once the fluid exits the rear duct, its immediately oriented upward towards the free shear layer by the lower pressure gradient where it acts a perturbation to the spanwise vortex filaments that are present

in the streamwise flow field moving over the mirror surface. Despite its original orientation as it flows through the mirror duct, the Jet1 passive jet has a large positive Y axis component and intersects with the free stream at a large angle. This perturbation or forced jet instigates the coherent pairing process as fluid is forced upwards into regions of the shear layer where the velocity gradient is larger. This phenomenon creates a forced mixing layer resulting in enhanced entrainment of the Jet1 model. This intersection occurs closer to the mirror surface than the location of the naturally occurring coherent vortices and prevents separation as the free stream remains attached to the mirror surface. The result of the JBT passive flow control is the initiation of the mixing process closer to the trailing edge of the mirror surface, the remediation of the adverse pressure gradients observed previously in the baseline flow and the convergence of the shear layer towards the center line of the recirculation region which all contribute to the behavior of the Jet1 flow field observed in the full wake profiles of Figure 3.2.

The Jet2 model can be seen as displaying similar traits as the Jet1 model but its mechanisms differ due to high velocity and high flow rates of the passive jet and its orientation to the free stream shear layer. Due to the high inlet and outlet areas, the Jet2 passive jet has much higher velocity and momentum. As a result, the passive jet can be observed to increase the production of vortices in the mixing layer when compared to the Jet1 and Baseline models. The vortices that occur in the mixing layer are due the high differential velocity gradients associated with the different shear layers of the jet exit region. In the jet region of the Jet2 model, it can be observed that a region of low velocity fluid exists between the free stream shear layer and top surface of the passive jet stream. As a result of the velocity differentials in this region, coherent counter rotating vortex shedding is present as the jet stream interface causes shearing with the region of fluid. Due to the properties of the mixing region, the Jet2 model can be observed to create higher concentrations of vortices in the mixing layer as it merges with the free stream shear layer as well. As was observed previously in the Jet1 model, the intersecting regions of flow create a mixing layer that enhances the

entrainment of the shear layer. In the Jet1 model, the passive jet intersects with the free stream at an angle such that a large component of the jet velocity is in the positive Y axis. The Jet2 model's passive jet merges with the free stream at an orientation that is slightly angled upward but almost parellel towards the free stream. The nature of the passive jet creates an additional interface of fluid in which shearing can occur due to the jet thickness. As the free stream flow progresses past the trailing edge of the mirror, its subjected to shear forces where the two flows merge. Due to the thickness of the jet flow of the Jet2 model, the parallel jet flow also exhibits shear between its lower interface and the recirculation region flow which cause coherent vortex shedding similar to what was observed in the baseline model between the recirculation region and the free stream. These three shearing interfaces create the turbulent mixing layer of the Jet2 model and cause the recirculation region to be greatly reduced. As a result, the recirculation region has an initiation height that is consistent with the height of the center mirror surface semi minor axis rather than the full semi minor axis of the full model. Additionally, the mixing layer of the Jet2 configuration is more turbulent and consists of a higher turbulent area in the mixing region.

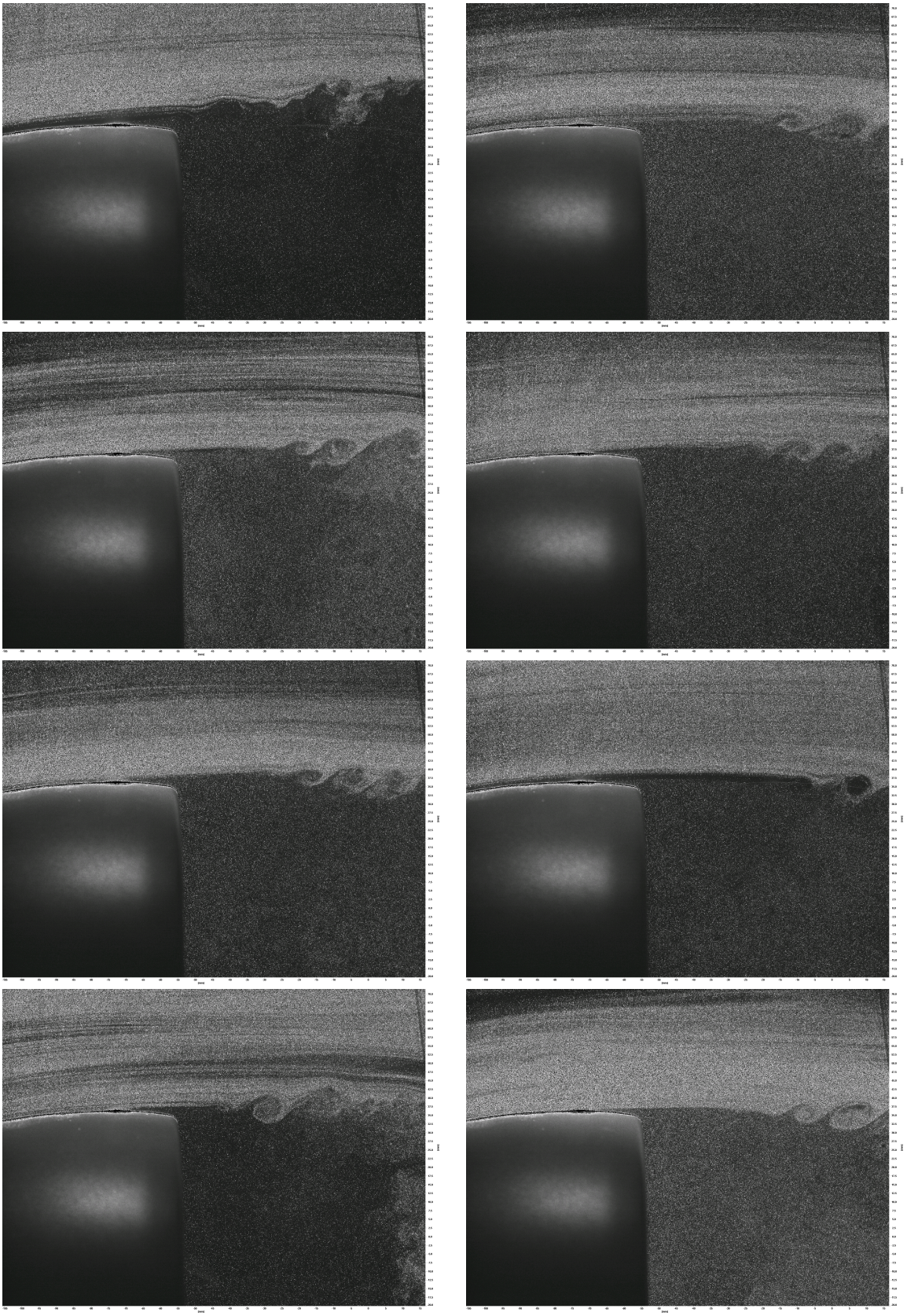

Figure 3.21: Baseline mirror PIV taken at 10ms displaying separation of the shear layer and coherent vortex production far downstream.

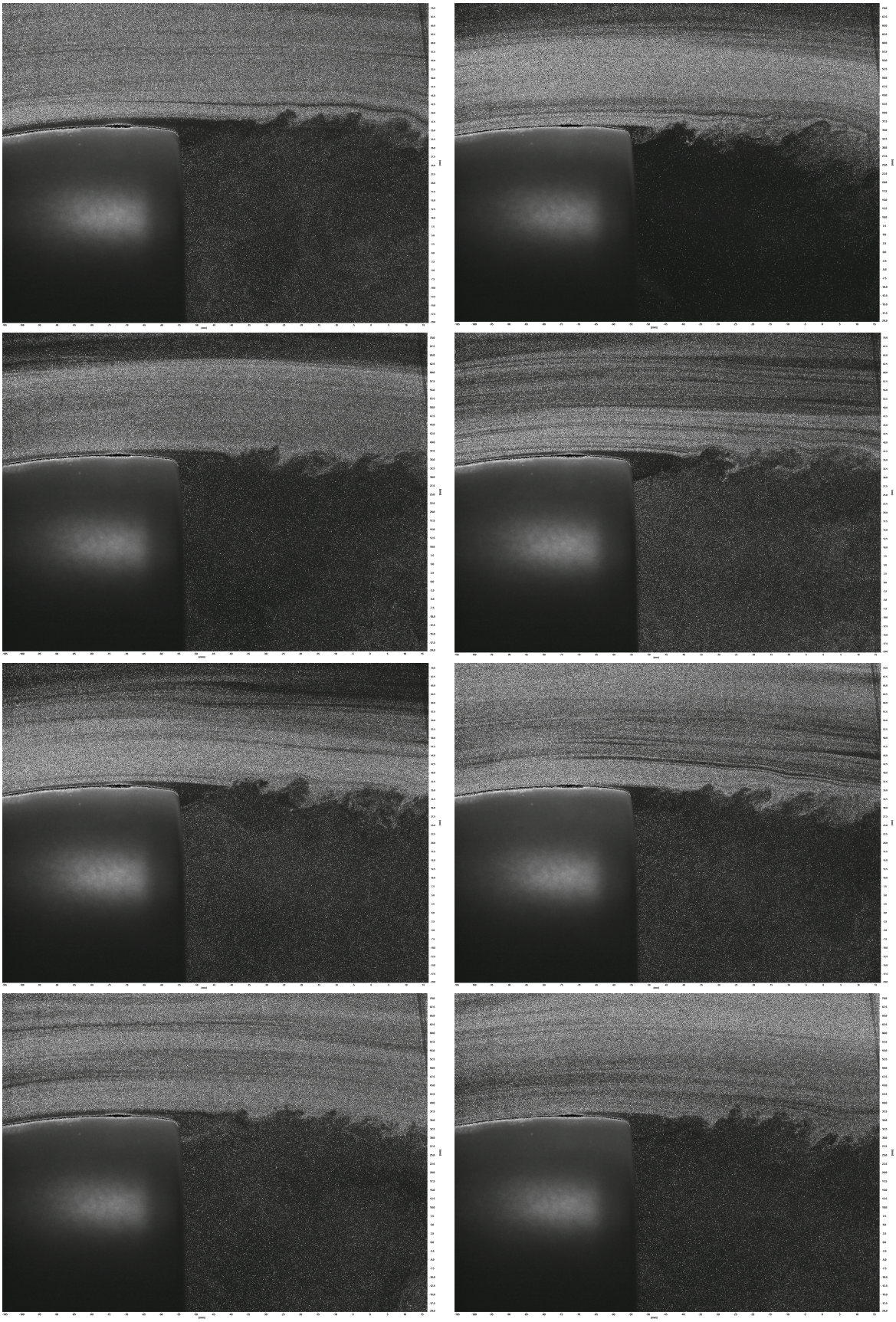

Figure 3.22: Jet1 PIV taken at 10ms displaying force mixing mechanism and shear layer interaction.

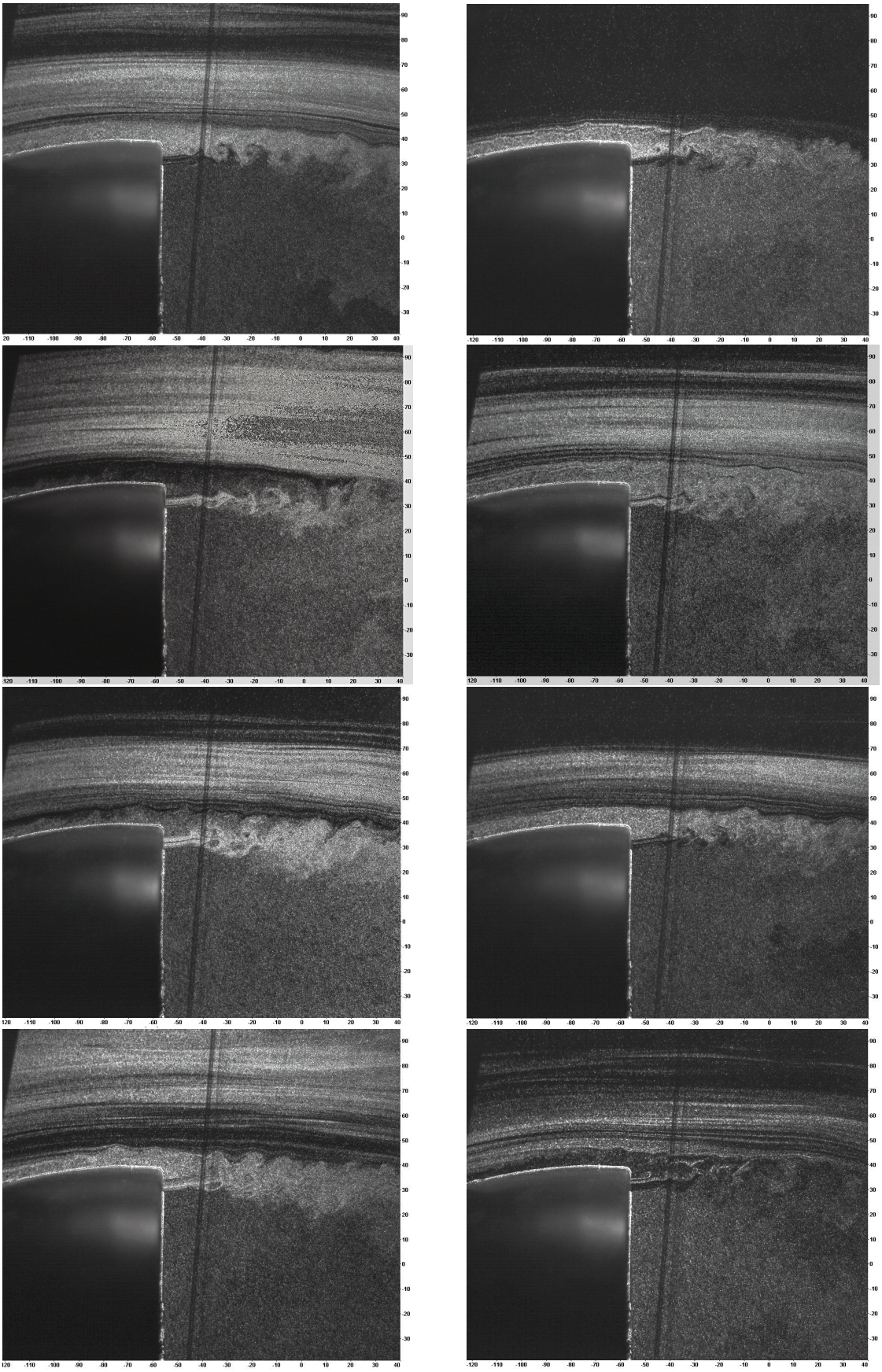

Figure 3.23: Jet2 PIV taken at 10ms displaying force mixing mechanism and shear layer interaction.

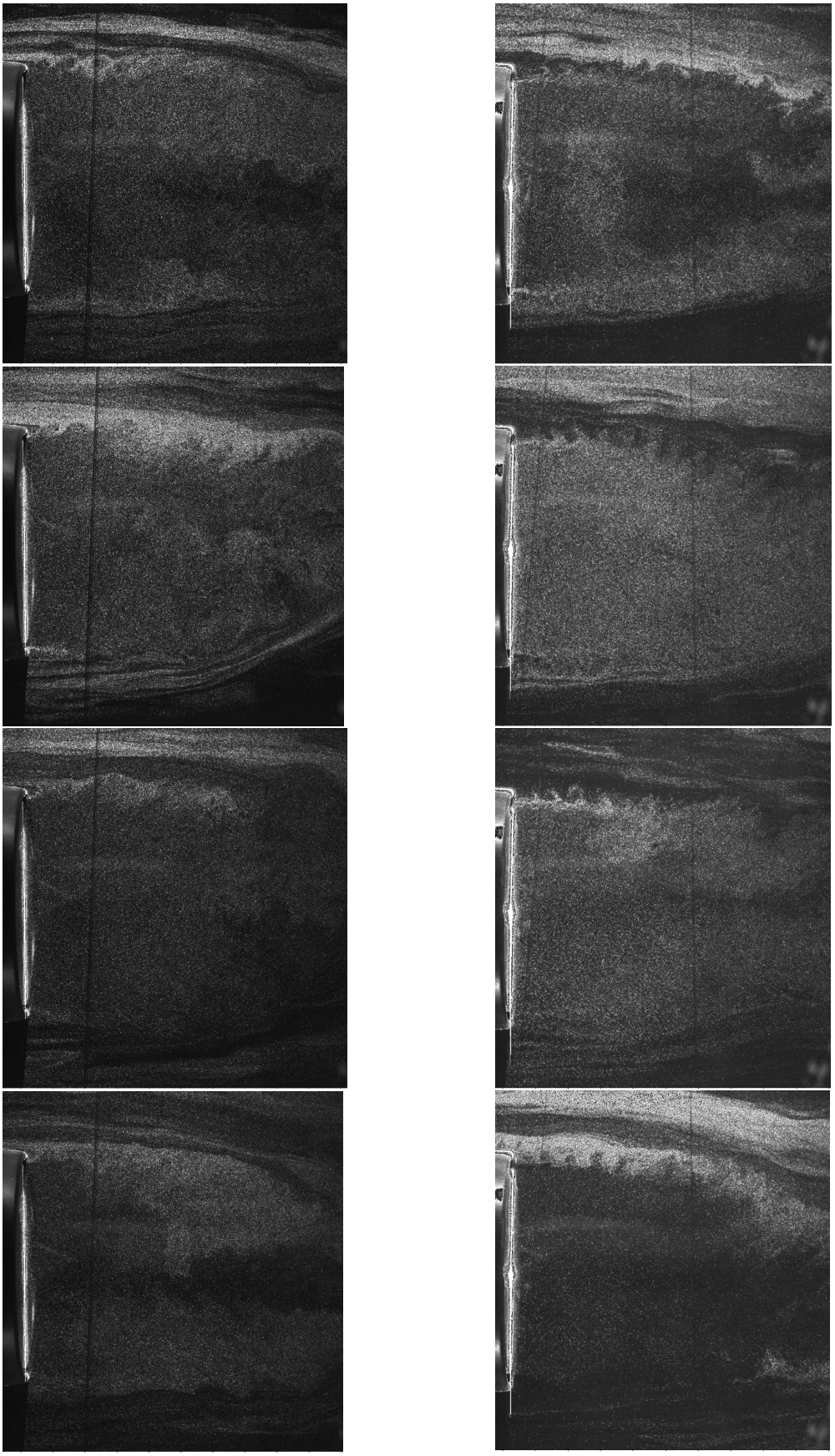

Figure 3.24: Jet PIV taken at 30ms displaying force mixing mechanism and shear layer interaction for both Jet models. Jet1 on the left, Jet2 on the right.

Average Velocity Contours PIV Data

Average velocity contour plots for the Reynolds number of Re = $2.55x10^5$ or V = 30m/s show significant differences in the base flow recirculation region due to the mechanisms displayed in the previous subsection. The contour plots displayed in this section are all normalized according to the recorded free stream velocity measured in the wind tunnel test section during the time of each experiment. The velocity scales of the measurements are kept constant for each component of velocity investigated in order to more clearly present the changes in the flow stream between experiments. Observing average velocity contour plots for the baseline model in Figure 3.25, the mixing layer that develops from the free stream and recirculation region interface displays a very linear growth rate with no abrupt thickening which initiates at the trailing edge of the mirror model. This behavior is consistent with what is expected from unforced boundary layers shown in the previous section in the PIV images with the coherent vortex structures. In addition, the orientation of the boundary layer is almost parallel to the flow stream with a slight inclination in the region that consists of velocities normalized to 1.1V of the recorded free stream velocities. The flow behavior for the Jet1 model can be seen in Figure 3.26. Observations of the flow field show the behavior expected from the implementation of the passive jet into the base flow area of the Jet mirror model. In this model, the non-linear growth rate accompanied by a forced jet mixing layer can be observed as it develops downstream of the Jet1 mirror model. This difference in the nature of the growth rate is also accompanied by the immediate thickening of the mixing layer in the region where the passive jet of the flow control design mixes with the free stream. This immediate increase in the thickness is also observed with an immediate contraction in the velocity profile of the mixing layer following the trailing edge. The mixing layer for the Baseline shear layer can be seen to have a lower shearing interface height equal to the height of the top the mirror surface. When compared to the Jet1 mirror model, the lower shearing interface is reduced to a new level below the top of the mirror surface. It is believed that the composition of all these factors that drive the overall reduction in the wake profile

observed in from the full field PIV measurements that were observed previously. In addition to the non-linear growth rate of the mixing layer, the orientation is now pivoted downward towards the centerline of the recirculation region from the lowered initiation point which accounts for the reduction of the wake profile and the lower negative velocity profile measures at 1.5 mirror lengths behind the rear surface. These traits all suggest the incorporation of a passive circumferential jet in the rear base region of a bluff body will successfully reduce the overall wake profile from the Baseline configuration. The enhanced mixing properties of the mixing layer not only initiates a thicker and lower shear layer there by reducing the area of the recirculation region but also increases the entrainment velocity as well. In a normal boundary layer, we can associate a thickening boundary layer to the increase in the entrainment velocity. From the mixing layer shown in the Jet1 velocity contour figures, the immediate thickening of the boundary layer suggest the immediate increase in the entrainment velocity near the trailing edge of the mirror model. This starts the entrainment process sooner in the base flow region, which aids in energizing the recirculation region and effectively resulting in the reduction of the drag. As the entrainment of the high energy flow into the base region develops, the velocity of this area is reduced and can be seen in the velocity contours. This reduction in the velocity is accompanied by an increase in the pressure of the region which effectively reduces the drag force produced by the bluff body. When comparing the Jet2 model flow field performance to the Jet1 model, significant alterations to the base flow region can be attributed to the nature of the passive jet geometry associated with the larger inlet and outlet found on the Jet2 design. As can be observed in Figure 3.27, the larger high momentum jet displays a noticeable contribution to the alteration of the mixing layer and the subsequent base flow region properties. Here, we can observe the high velocity jet region extending further in the base flow region, merging with the free stream shear layer at a slight inclined angle. The high momentum jet also can be observed to obstruct the formation of a continuous mixing layer as was see in Figure 3.26 associated with the Jet1 mixing layer. The penetration of the high momentum and high

velocity fluid further downstream creates a larger region of turbulence and a recirculation region that initiates at a smaller height as well. Despite these alterations, the passive jet in the Jet2 design injects a large amount of high energy fluid downstream which while preventing the wake region from contracting as significantly as seen in the Jet1 model results in a smaller recirculation region as can be observed in Figure 3.27. Velocity contours of the base flow recirculation region suggest that despite the reduction in area, the velocity recorded is observed to be higher for a significant portion of the flow field when compared to the Jet1 model in addition to the velocity profile recorded at 1.5 mirror lengths downstream.

Model	BL	Jet1	Jet2
Vjet	0.0 %	.4138 %	.9860

Table 3.1: Mean Jet Velocities

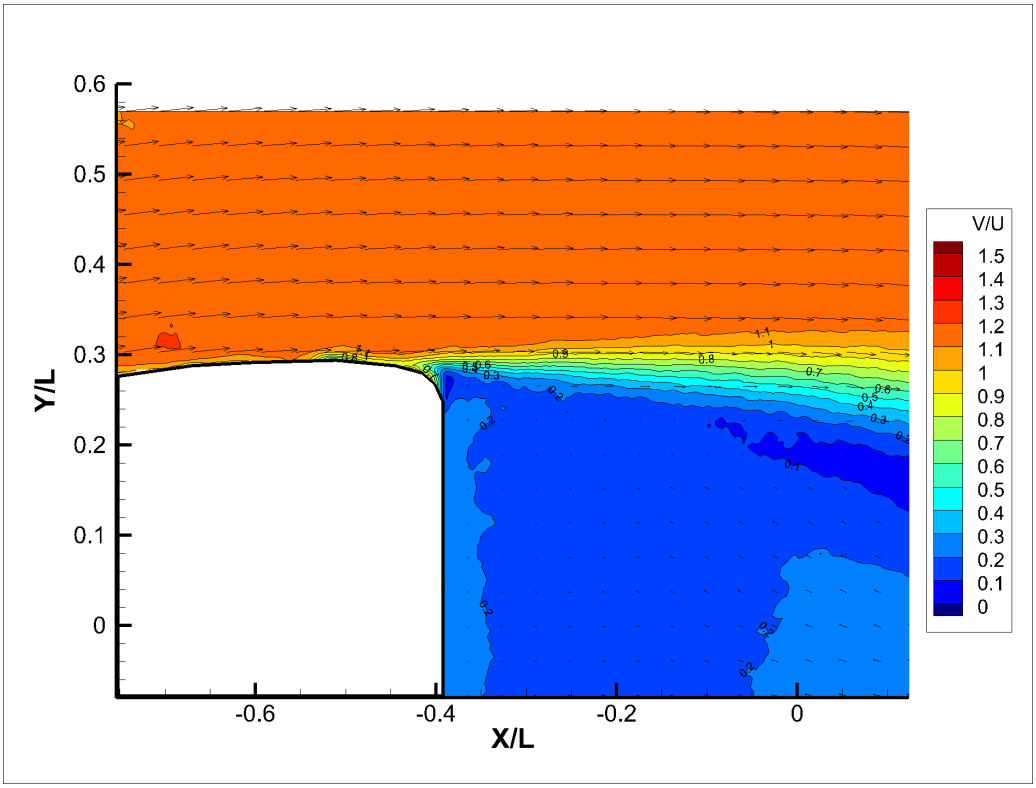

Figure 3.25: Baseline mirror mean total velocity contours in the vertical symmetry plane of the near wake. V = 30 m/s, Re = 2.55x10^5.

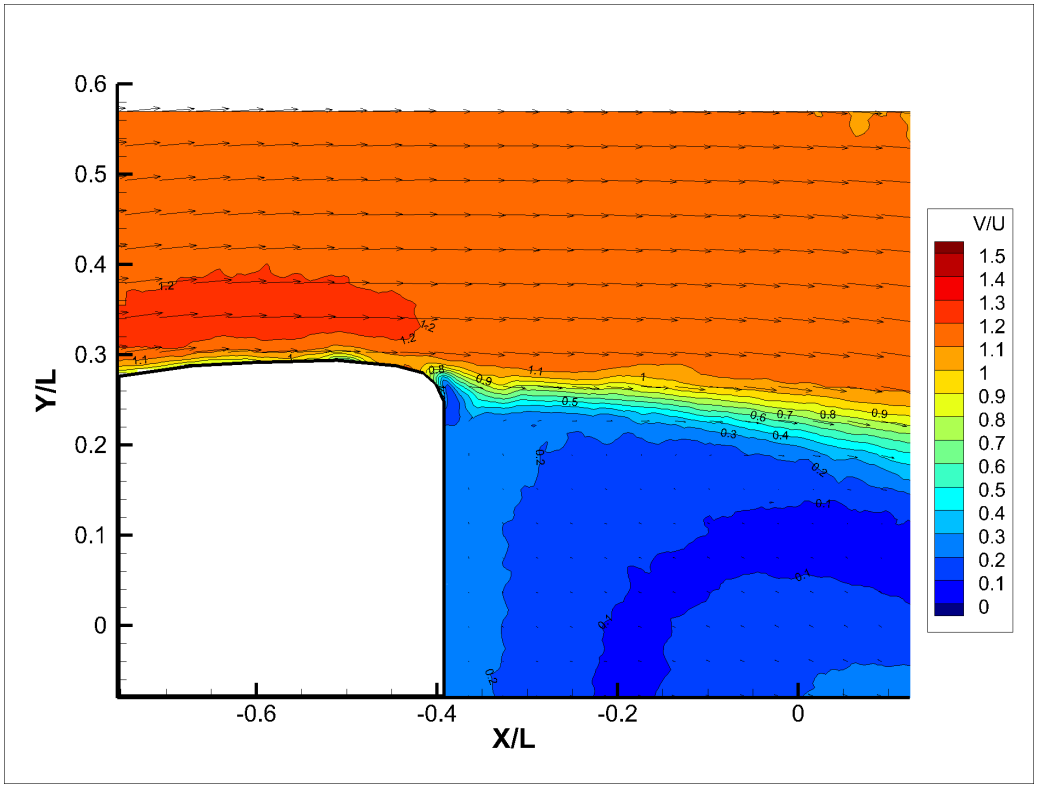

Figure 3.26: Jet1 mirror mean total velocity contours in the vertical symmetry plane of the near wake. V = 30 m/s, Re = 2.55×10^5.

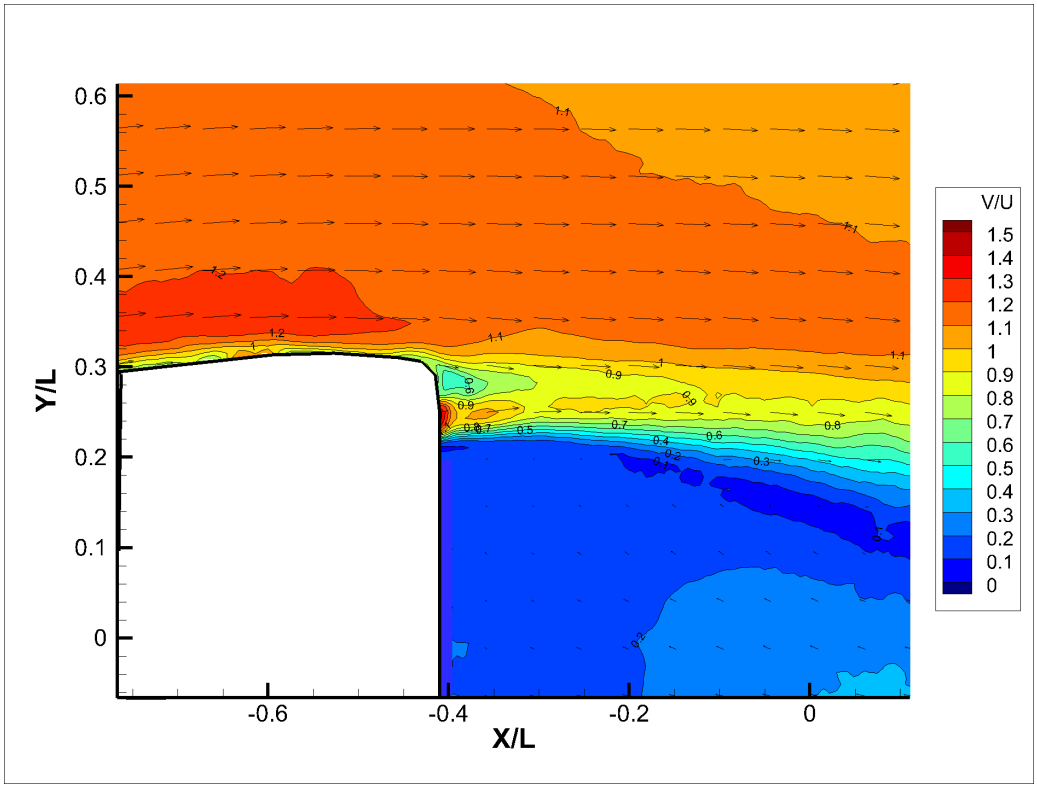

Figure 3.27: Jet2 mirror mean total velocity contours in the vertical symmetry plane of the near wake. V = 30 m/s, Re = 2.55×10^5.

The Vx velocity profiles of the trailing edge for all three mirror designs presents similar data to what can be viewed in Figures 3.25 - Figure 3.27. As can be observed in Figure 3.28, the mixing layer that is created at the interface between the free stream and the recirculation region shows a linear growth pattern initiated the rear trailing edge of the mirror body and at a height even with the top surface. This mixing layer continues to grow through vorticity diffusion and displays a flow direction that is almost parallel to the free stream. Contrast to the behavior of the Jet1 mirror design in Figure 3.29, the recirculation region velocity was measured to contain regions of higher negative Vx velocity magnitudes and can be observed to have larger concentrations present as well. The passive jet utilized in the Jet1 model displays a strong influence the Vx component of the flow velocity. As was noticed of the mixing layer in the planar velocity contours, a contraction of the recirculation region can be noticed in the area where the passive jet stream intersect with the free stream shear layer. This reduction or sharp convergence of the mixing layer is followed with an immediate thickening of the shear layer as well which is known to be a trait for forced mixing layers. In addition to the behavior of the mixing layer, the recirculation region shows a reduction in the recirculation velocity for the Vx component of flow and an area of increased velocity in the Vx component above the trailing edge mirror surface. The presence of the high velocity region in the Jet1 flow field at the trailing edge of the mirror suggests the acceleration is caused by the passive jet and the associated mixing effect it has when it comes in contact with the free stream shear layer. Figure 3.30 shows the impact the larger high momentum jet of the Jet2 model displays on the Vx component of velocity in flow field behind the trailing edge of the mirror. Similar to what is seen in the flow above the Jet 1mirror surface, the Jet2 model also displays a region of high magnitude Vx component of velocity in addition to an increase in the Vx recirculation velocity component as well. This is accompanied by an initial reduction in the mixing layer which is observed to be more pronounced for the Jet2 model than the behavior seen in the Jet1 model. The high velocity jet region is also clearly defined and the mixing layer created from the merging of the free stream shear

layer shows a nonlinear growth rate as well.

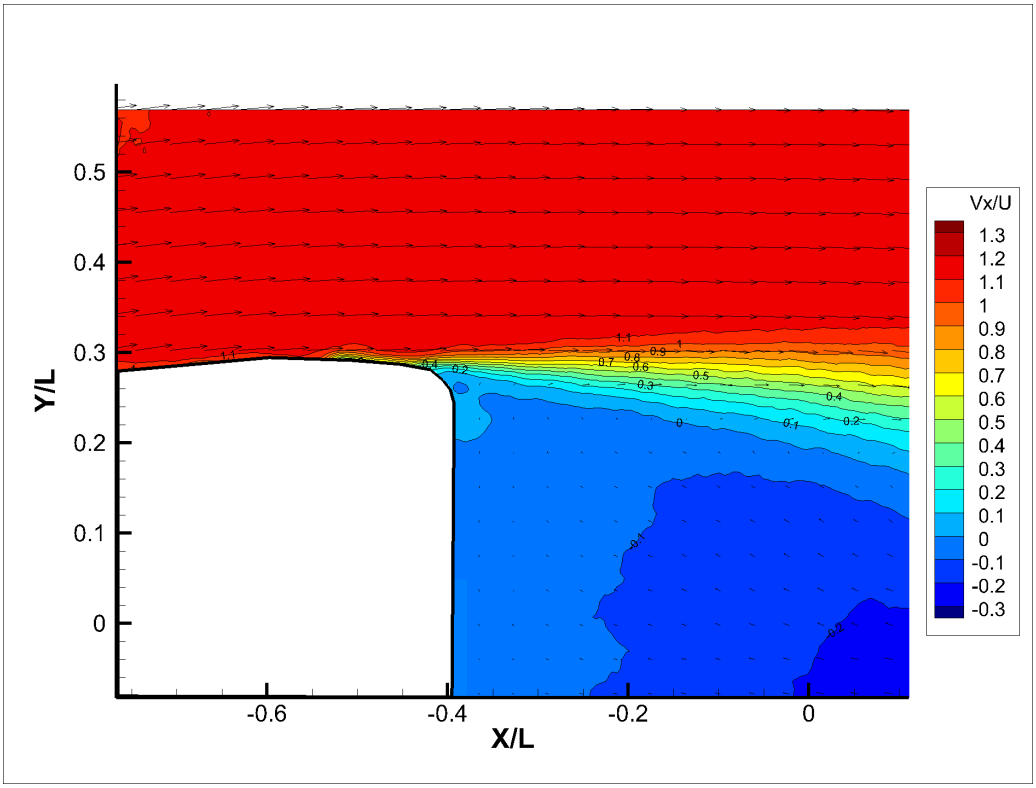

Figure 3.28: Baseline mirror mean Vx velocity contours in the vertical symmetry plane of the near wake. V = 30 m/s, Re = 2.55×10^5.

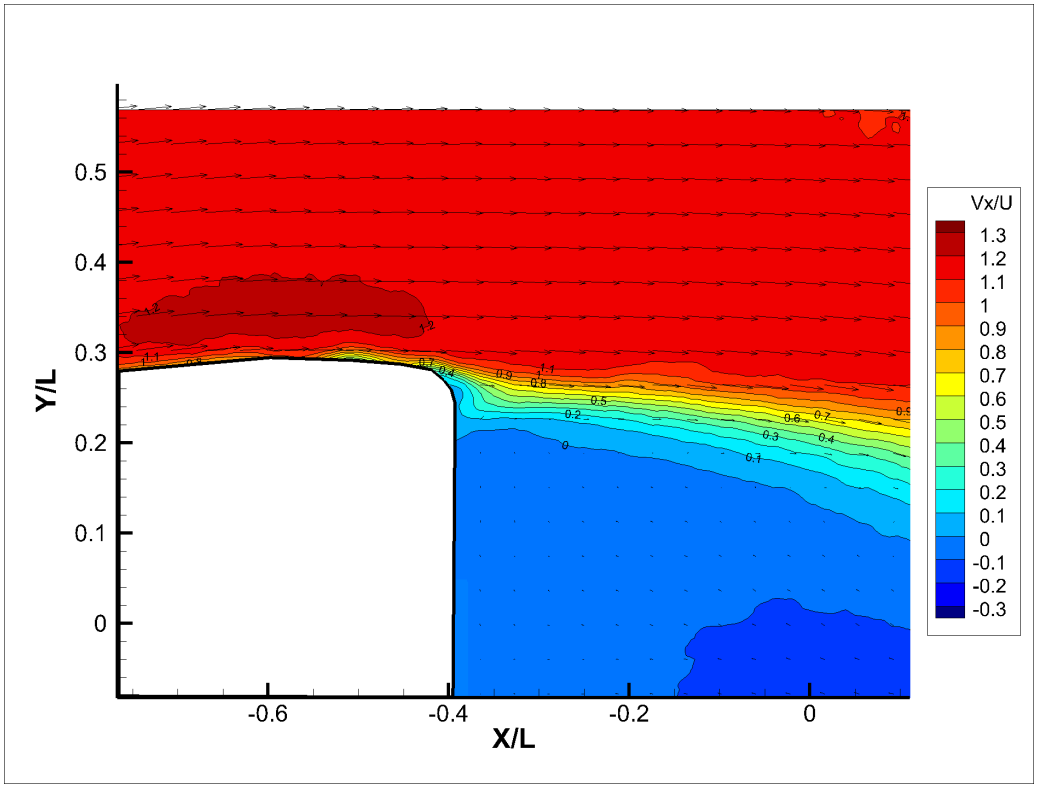

Figure 3.29: Jet1 mirror mean Vx velocity contours in the vertical symmetry plane of the near wake. V = 30 m/s, Re = 2.55x10^5.

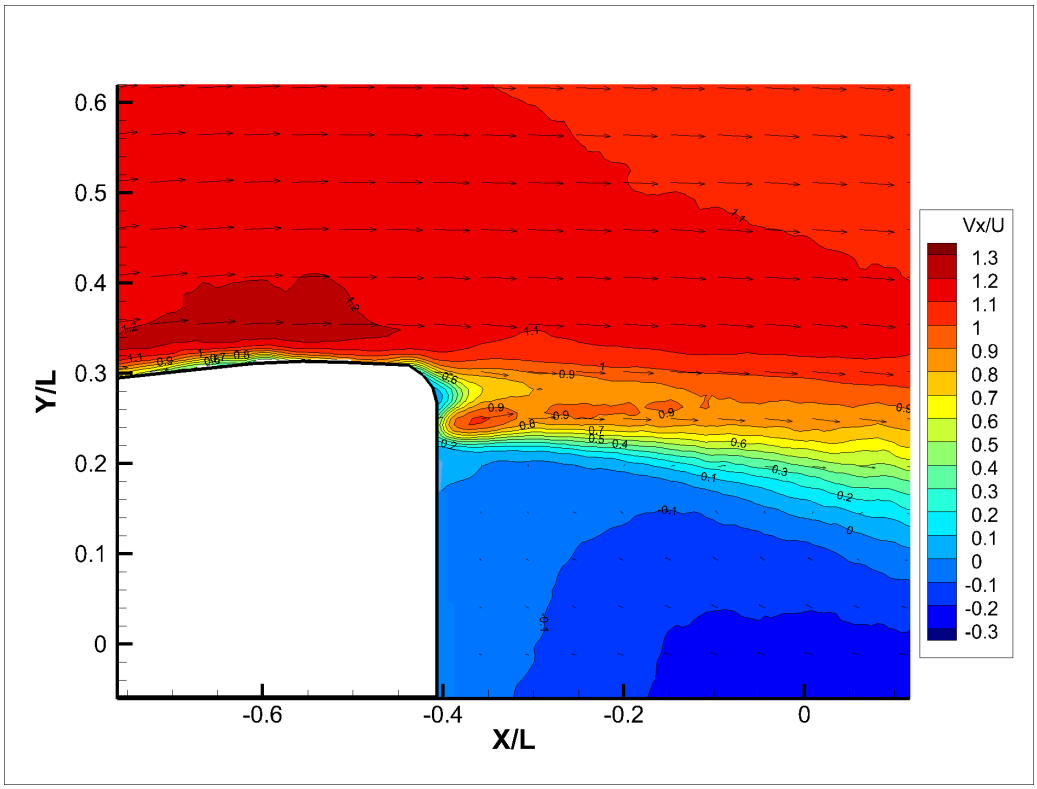

Figure 3.30: Jet2 mirror mean Vx velocity contours in the vertical symmetry plane of the near wake. V = 30 m/s, Re = 2.55x10^5.

The Vy component of Velocity for each model can be observed in the Figures

3.31 - 3.33. The baseline model displays large concentration of positive Vy component of velocity within the recirculation region with the negative components of the free stream outside of the viewing area. This suggests the contraction of the base flow region is extend and initiates further downstream that what can be observed in the viewing area. The Jet1 configuration in Figure 3.32 shows interesting traits that are a result of the passive jet and its mixing effects on the free stream shear layer. Immediately noticeable near the trailing edge of the mirror is the area of opposing Vy components of flow. These are located almost adjacent to the rear mirror surface. The area of negative Vy velocity component is directly above the area associated with a concentration of positive Vy component of flow due. This is consistent with the Vx velocity profile for the Jet1 configuration in Figure 3.29 as the negative Vy component of velocity is in the region of the contraction of the mixing layer initiated by the passive jet. Similar behavior can also be observed in the Jet2 Vy velocity contour plot in Figure 3.33. The Jet2 model shows a higher magnitude of measured velocities in the region immediately downstream of the passive jet due to the high velocity mixing of the jet and the shear layer. These velocity magnitude contours suggest that the higher momentum jet for the Jet2 configuration creates a stronger pair of opposing Vy velocity components and the effect can be seen by the sharper contraction of the mixing layer in the Jet2 Vx profile in Figure 3.30. Additionally, the initiation of high magnitude negative Vy velocities downstream indicate the entrainment of the high energy free stream is reducing the wake area which is consistent behavior in both Jet1 and Jet2 models. The Jet1 models displays higher recorded negative velocities that can be observed to occur closer to the trailing edge of the mirror and contains the recirculation region with the lowest positive Vy components of flow. This data suggests the reduction of the recirculation region velocity is dependent on the component of negative velocity into the region through the mixing layer. The Jet2 model, despite having an increased presence of negative Vy velocity components in the downstream wake region when compared to the baseline model, also has a recirculation area with larger positive Vy components of velocity when compared to

the Jet1 model.

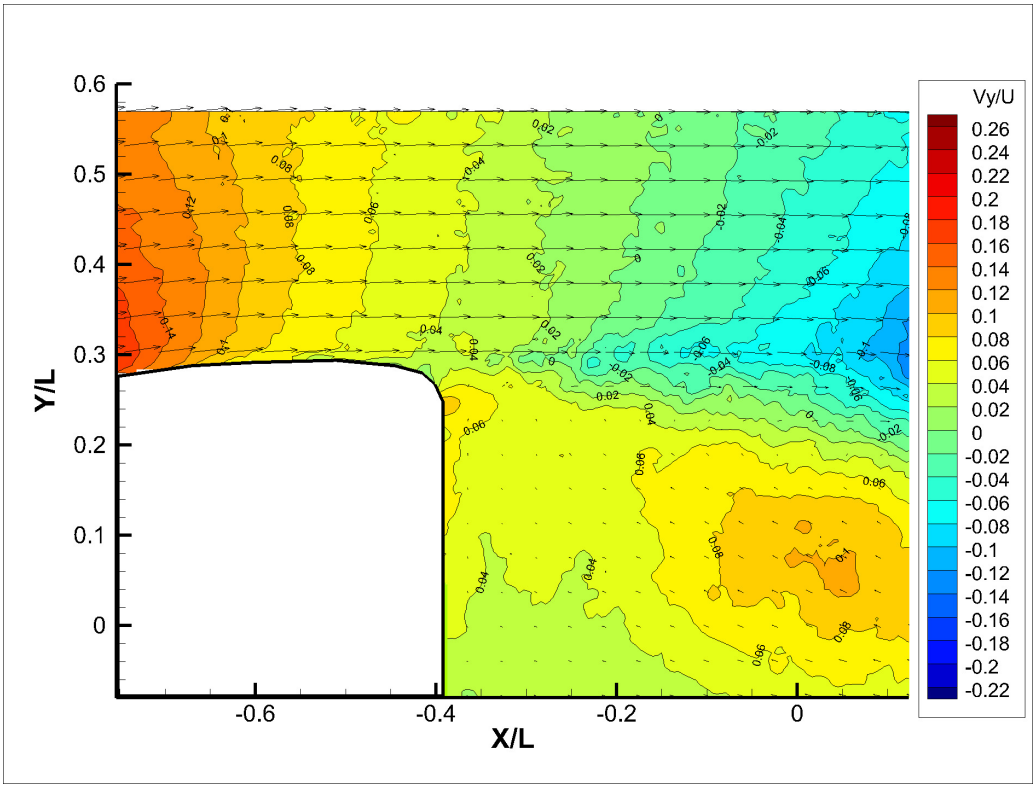

Figure 3.31: Baseline mirror mean Vy velocity contours in the vertical symmetry plane of the near wake. V = 30 m/s, Re = 2.55x10^5.

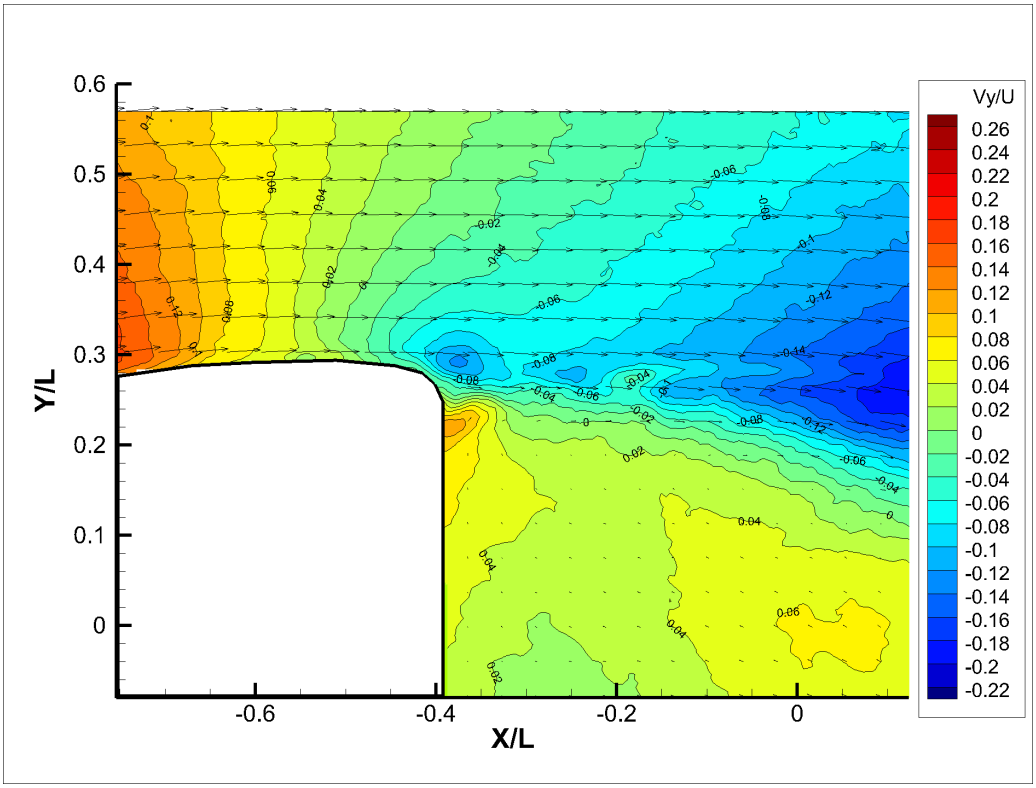

Figure 3.32: Jet1 mirror mean Vy velocity contours in the vertical symmetry plane of the near wake. V = 30 m/s, Re = 2.55x10^5.

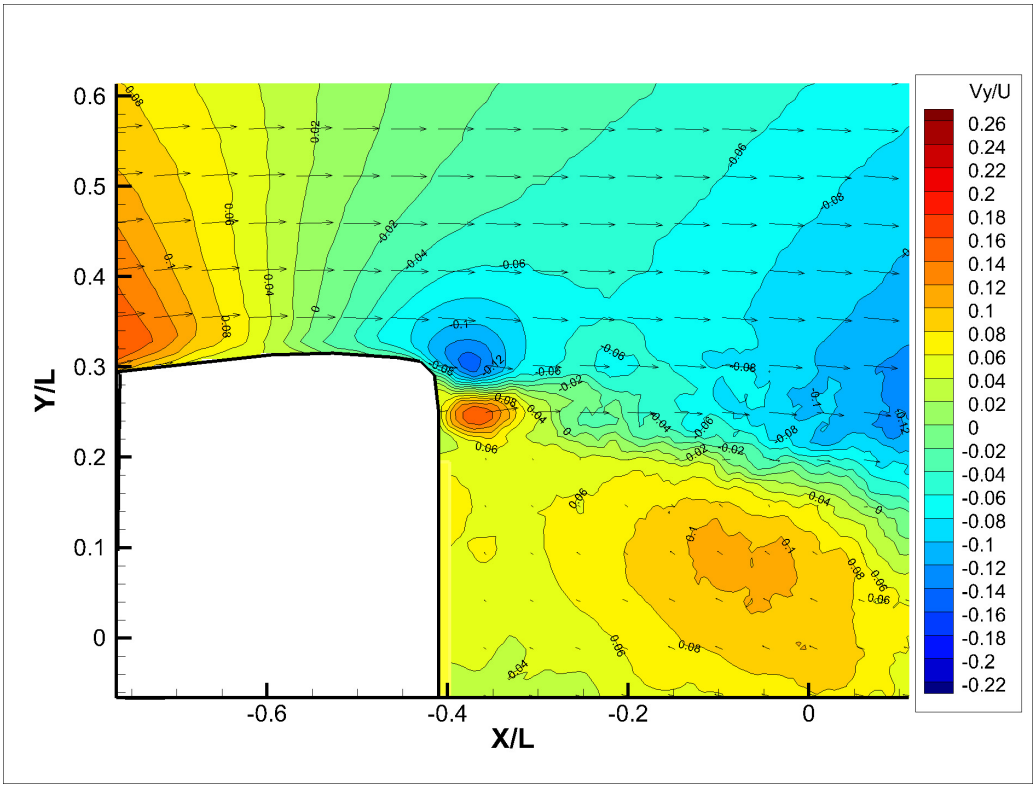

Figure 3.33: Jet2 mirror mean Vy velocity contours in the vertical symmetry plane of the near wake. V = 30 m/s, Re = 2.55x10^5.

The Z component of velocity for the trailing edge of the mirror can be observed in the Figure 3.64 - 3.66. The Jet1 model displays detached region of positive Z component of velocity that is directly attributed to the passive jet. This region is also accompanied by an opposing Vz component of velocity at the trailing edge of the mirror. This behavior was not observed on the Baseline or Jet2 model base flow field and is oriented 90 ° from the high velocity Vy component of flow that was observed in Figure 3.32. This data suggests the influence of the Jet 1passive jet is creating substantial vorticity in the region which is aiding in initiating the entrainment of the high energy flow into the base region.

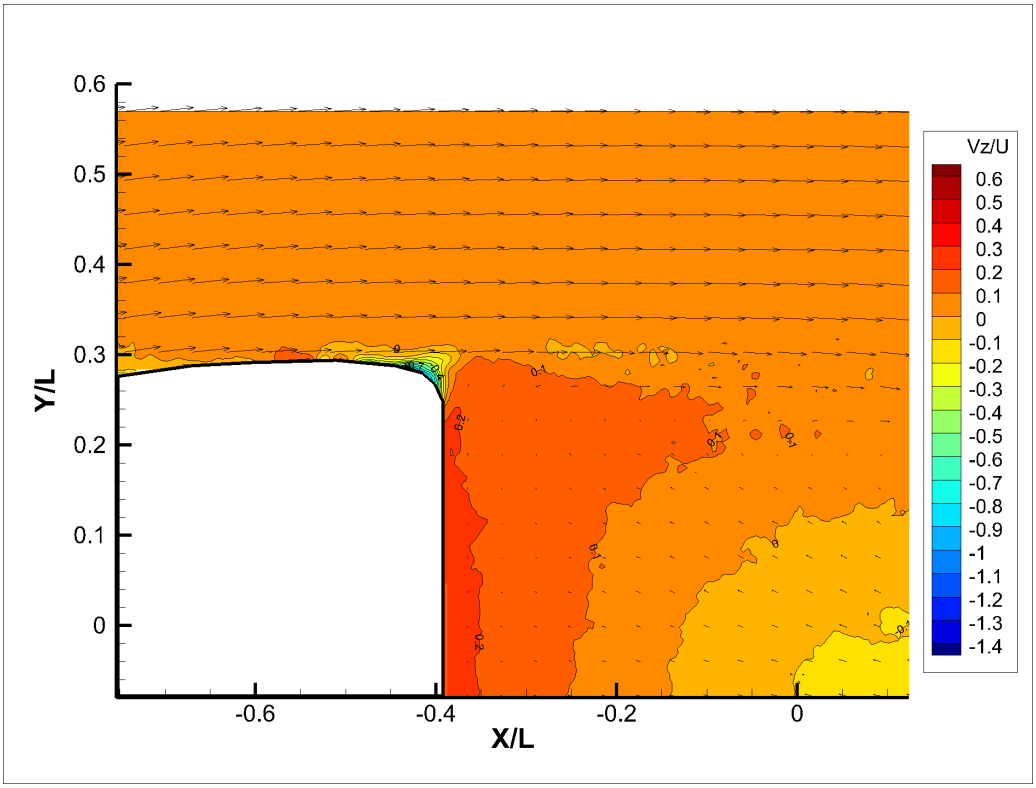

Figure 3.34: Baseline mirror mean Vz velocity contours in the vertical symmetry plane of the near wake. V = 30 m/s, Re = 2.55x10^5.

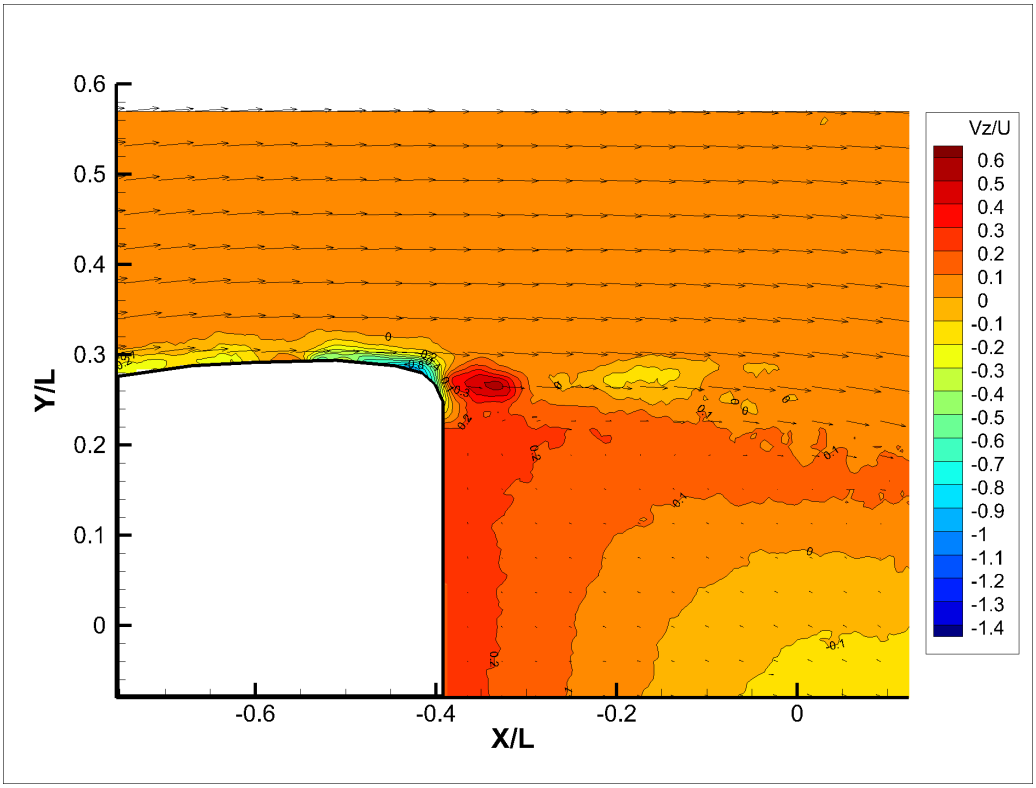

Figure 3.35: Jet1 mirror mean Vz velocity contours in the vertical symmetry plane of the near wake. V = 30 m/s, Re = 2.55x10^5.

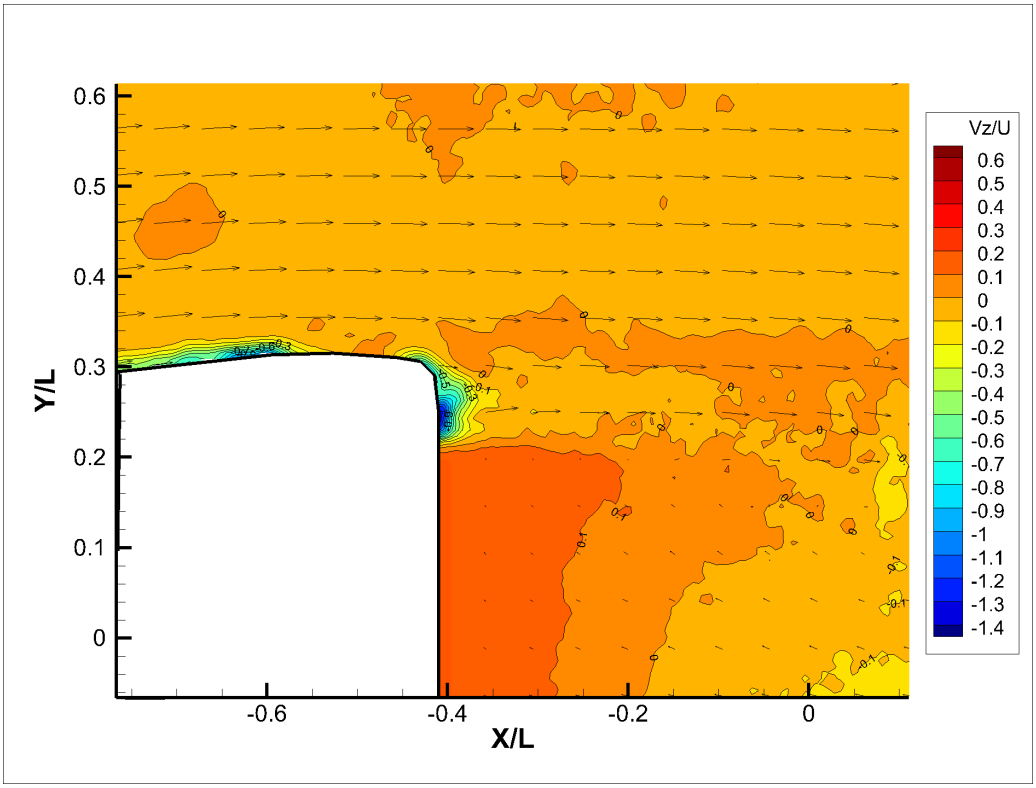

Figure 3.36: Jet2 mirror mean Vz velocity contours in the vertical symmetry plane of the near wake. V = 30 m/s, Re = 2.55×10^5.

3.0.7 Vorticity of the Trailing Edge Jet Region

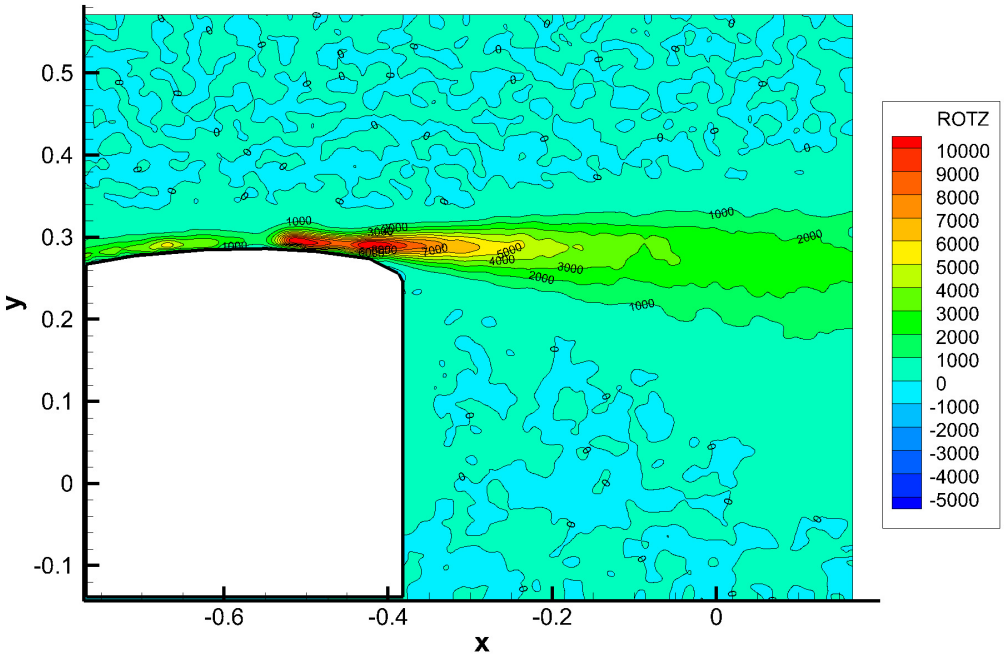

Figure 3.37: Baseline mirror mean Vorticity contours in the vertical symmetry plane of the near wake. V = 30 m/s, Re = 2.55x10^5.

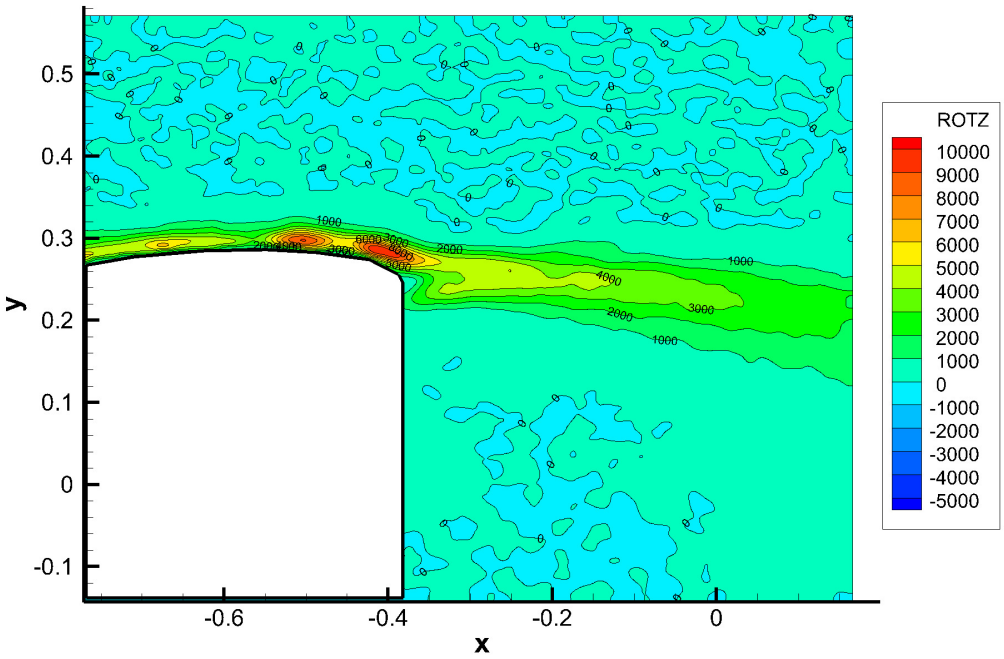

Figure 3.38: Jet1 mirror mean Vorticity contours in the vertical symmetry plane of the near wake. V = 30 m/s, Re = 2.55x10^5.

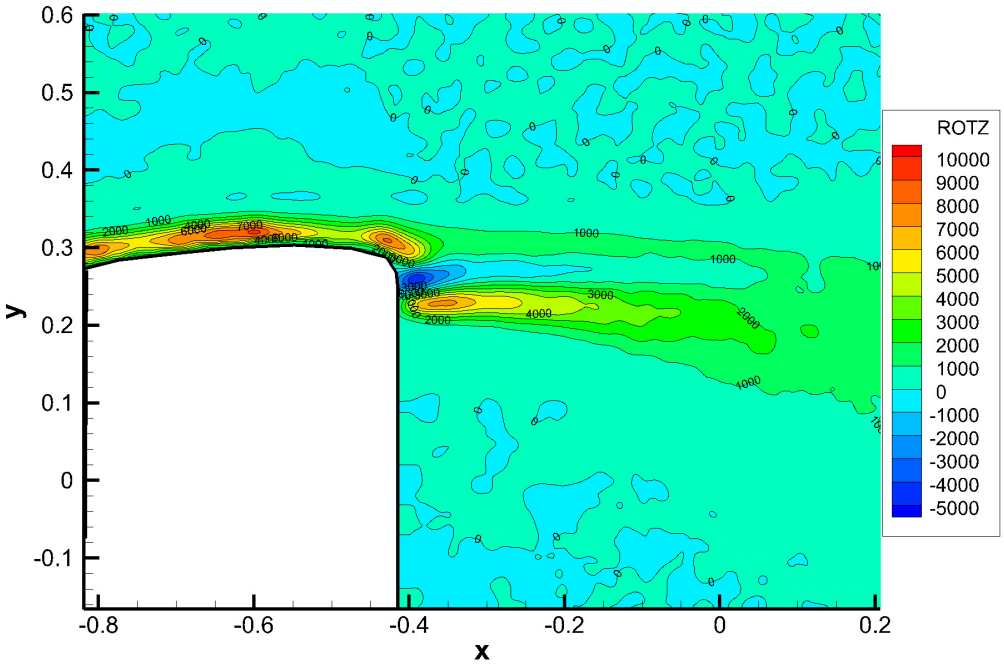

Figure 3.39: Jet2 mirror mean Vorticity contours in the vertical symmetry plane of the near wake. V = 30 m/s, Re = 2.55x10^5.

3.0.8 Reynolds Stress of the Trailing Edge Jet Region

The second order velocity correlations in the streamwise vertical mid plane are shown in the following figures. Figure 3.40 shows the $\frac{\overline{u'u'}}{U^2}$ component of Reynolds normal stress. The Baseline model displays local maximum values in the shear layer downstream of the rear surface of the model. The normal stress component of $\frac{\overline{u'u'}}{U^2}$ correlates with the position of the shear layer displayed in Figure 3.25 showing the planar velocity contours. The Jet1 model in Figure 3.41 shows immediate changes in the normal stress distribution due to implementation of the passive jet. Noticeable on the top of the mirror surface, high fluctuations in the Vx component of velocity suggest acceleration and high rate of change for the velocity in the region. The magnitude of the normal stress is also significantly higher correlating to the velocity contours on the model of Figure 3.29. These areas of high normal stress in conjunction with the area of acceleration in the flow stream over the model surface suggest the implementation of the passive jet not only affects the downstream base flow region but also the upstream boundary layer on the model surface as well. In addition to increased $\frac{\overline{u'u'}}{U^2}$ normal stress on the mirror surface, the shear layer for the Jet1 configuration indicates increased normal stress in the flow stream as it contracts and flows into the mixing region between the circumferential jet and the free stream. This behavior indicates the turbulence of the region is also influenced by the mixing dynamics between the passive jet and the shear layer. As seen in the model for the Baseline configuration, the $\frac{\overline{u'u'}}{U^2}$ normal stress also coincides with the area of the shear layer for the Jet1 configuration displayed on Figure 3.29. While the Jet 2 configuration displays similar behavior to the Jet1 model, the larger Inlet/Outlet ratio jet has a much more unique downstream contribution and less influence on the boundary region of the mirror surface. In the immediate proximity to the trailing edge of the mirror model, a high magnitude distribution of $\frac{\overline{u'u'}}{U^2}$ normal stress can be observed indicating the high flow jet creates high magnitude of turbulent fluctuations in the X direction due to the passive Jet.

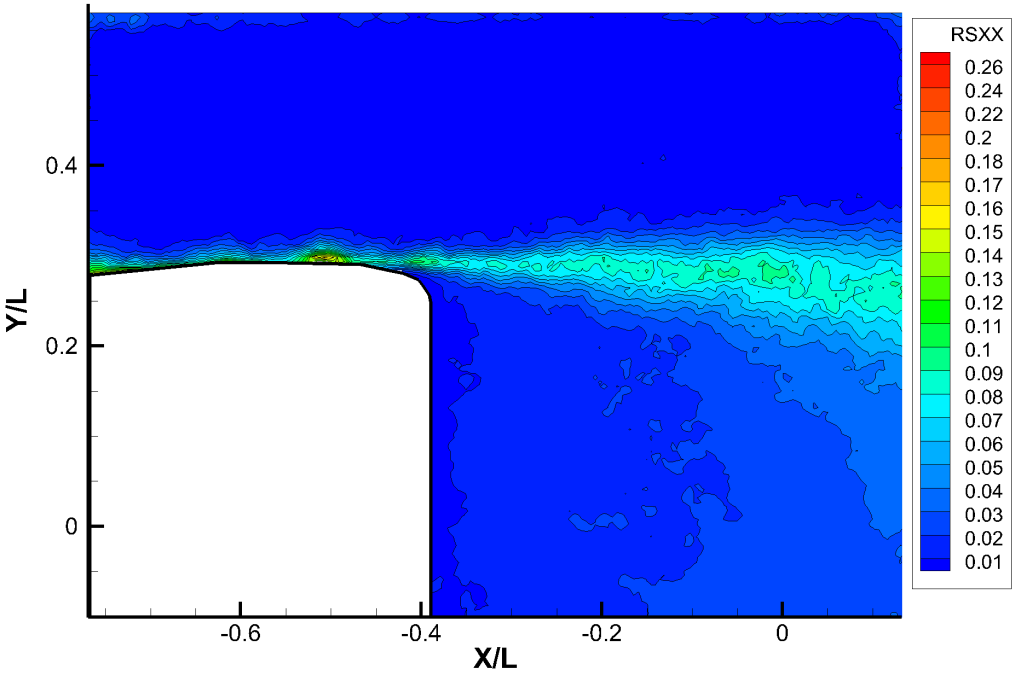

Figure 3.40: Baseline Mirror $\frac{\overline{u'u'}}{U^2}$ Reynolds Stress contours in the vertical symmetry plane of the wake. V = 30 m/s, Re = 2.55x10^5.

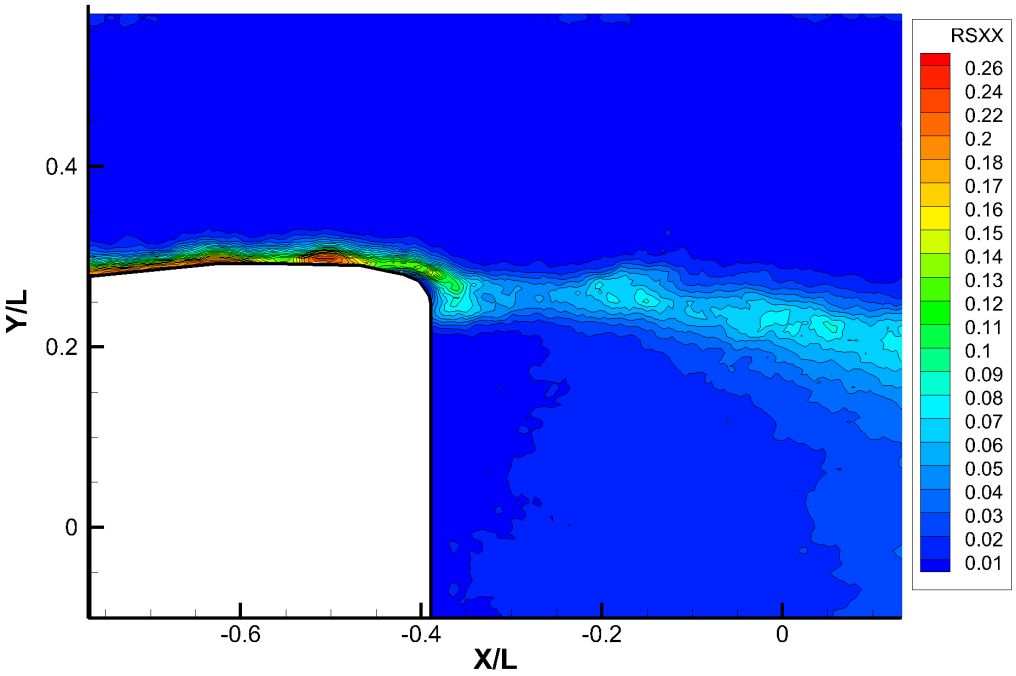

Figure 3.41: Jet1 Mirror$\frac{\overline{u'u'}}{U^2}$ Reynolds Stress contours in the vertical symmetry plane of the wake. V = 30 m/s, Re = 2.55x10^5.

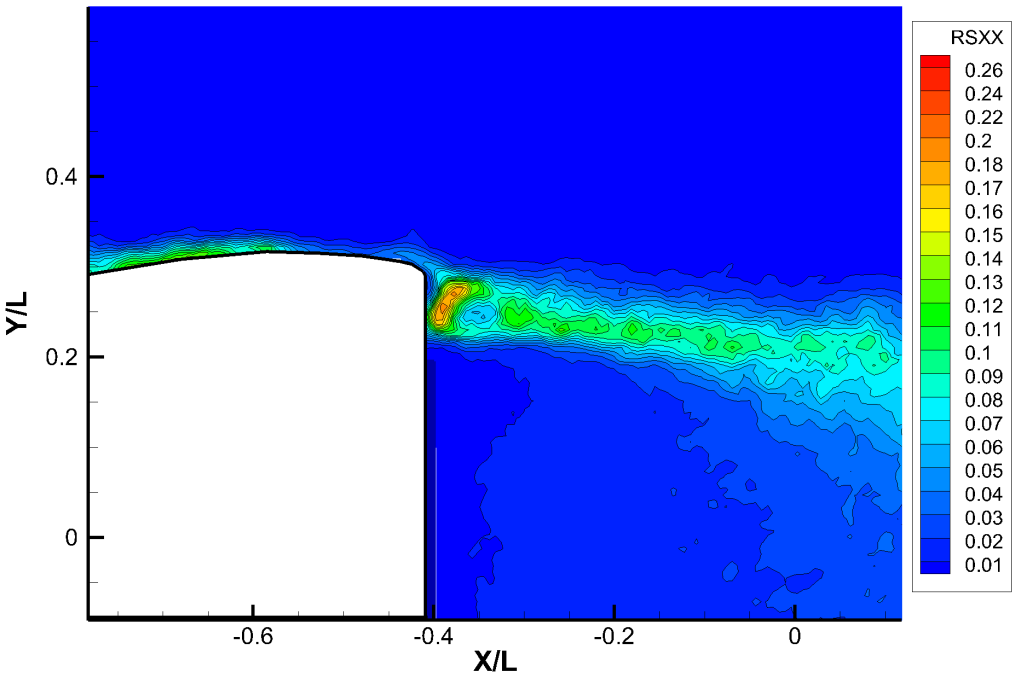

Figure 3.42: Jet2 Mirror $\frac{\overline{u'u'}}{U^2}$ Reynolds Stress contours in the vertical symmetry plane of the wake. V = 30 m/s, Re = 2.55x10^5.

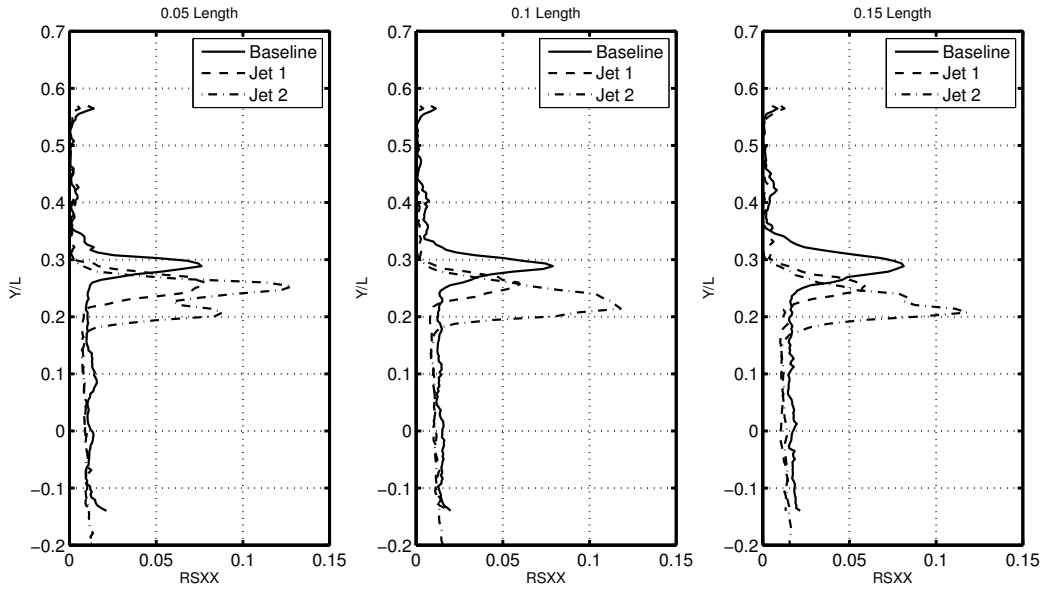

Figure 3.43: $\frac{\overline{u'u'}}{U^2}$ Reynolds Stress profiles for select mirrors lengths downstream. V = 30 m/s, Re = 2.55x10^5.

The $\frac{\overline{u'v'}}{U^2}$ component of Reynolds stress can be observed for all three models in Figures 3.44 - Figures 3.46. Associated with each model are high magnitudes in

turbulent fluctuations with increasing intensity downstream from the mirror. The Jet1 model shows a reduction in the turbulent fluctuations for $\frac{\overline{u'v'}}{U^2}$ downstream as the area of high magnitude $\frac{\overline{u'v'}}{U^2}$ Reynolds stress is also noticeably reduced when compared to both baseline and Jet2 models. The Jet1 model can be seen influencing the region of the shear layer immediately following the trailing edge of the model. Observed in Figure 3.45, Reynolds stress concentrations on the base region of the mirror surface can be observed to possess localized regions of increased $\frac{\overline{u'v'}}{U^2}$ Reynolds stress values when compared to the baseline model. The Jet1 model is also observed to reduce the intensity area of the $\frac{\overline{u'v'}}{U^2}$ region that develops downstream when compared to the Baseline and Jet2 models in despite having reduced jet area. In Figure 3.46, the Jet2 configuration displays a strong influence in the jet region of the base flow with a strong positive magnitude of $\frac{\overline{u'v'}}{U^2}$ stress due to the positive orientation of the jet leaving the circumferential slot. Despite the strong influence in the base flow region, the base region of the mirror surface does not exhibit the same effect that was seen in the Jet1 model.

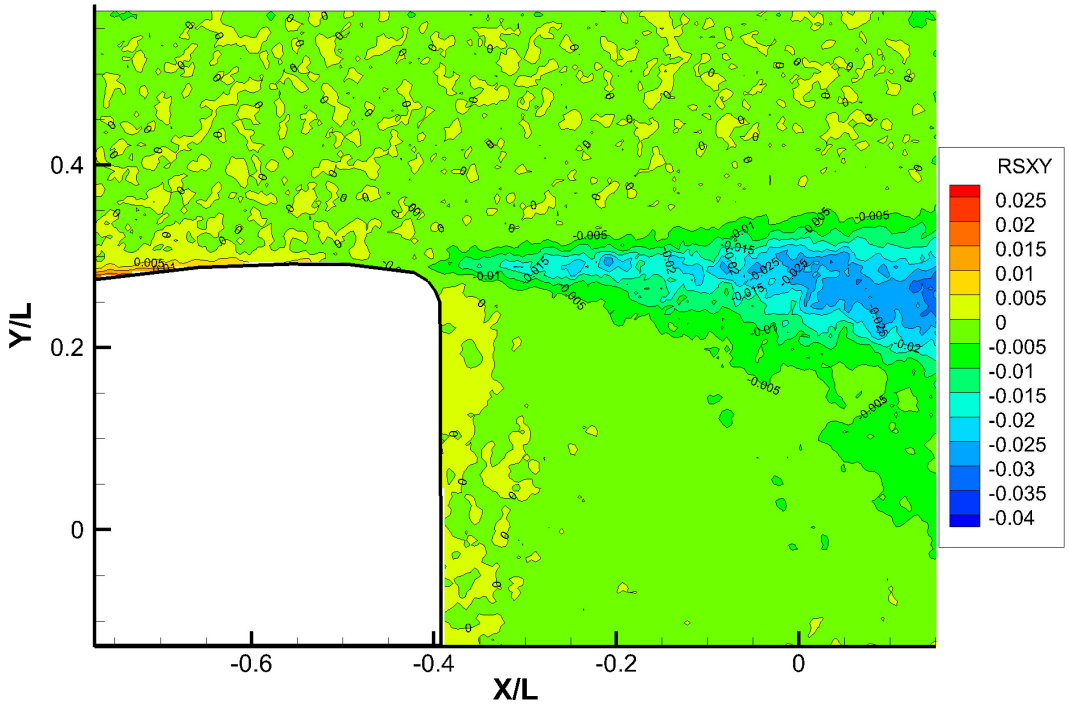

Figure 3.44: Baseline Mirror $\frac{\overline{u'v'}}{U^2}$ Reynolds Stress contours in the vertical symmetry plane of the wake. V = 30 m/s, Re = 2.55x10^5.

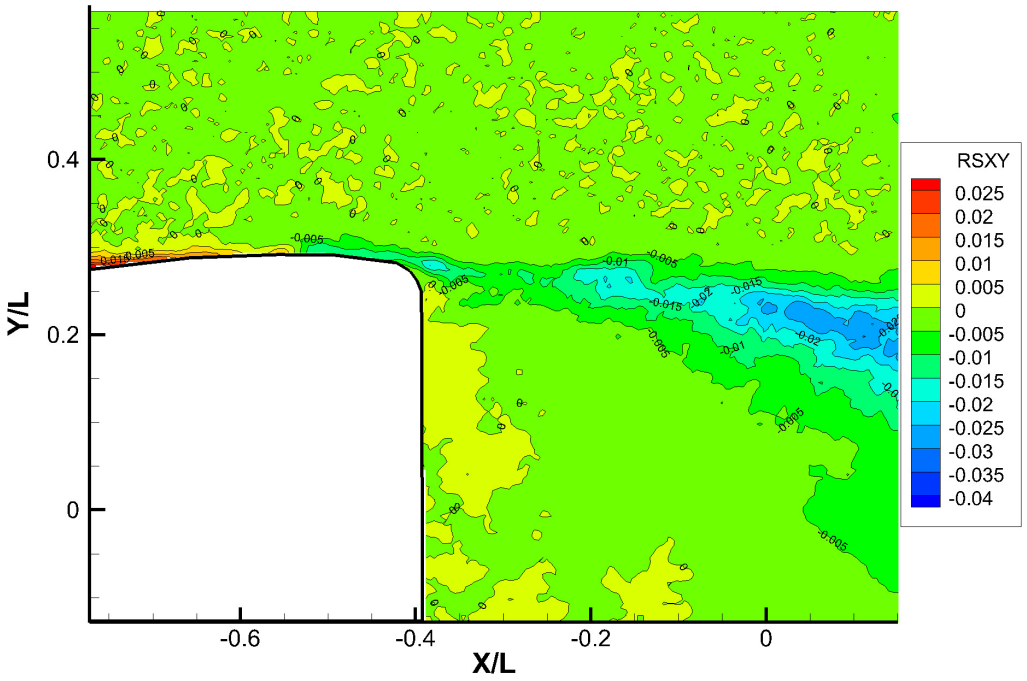

Figure 3.45: Jet1 Mirror $\frac{\overline{u'v'}}{U^2}$ Reynolds Stress contours in the vertical symmetry plane of the wake. V = 30 m/s, Re = 2.55x10^5.

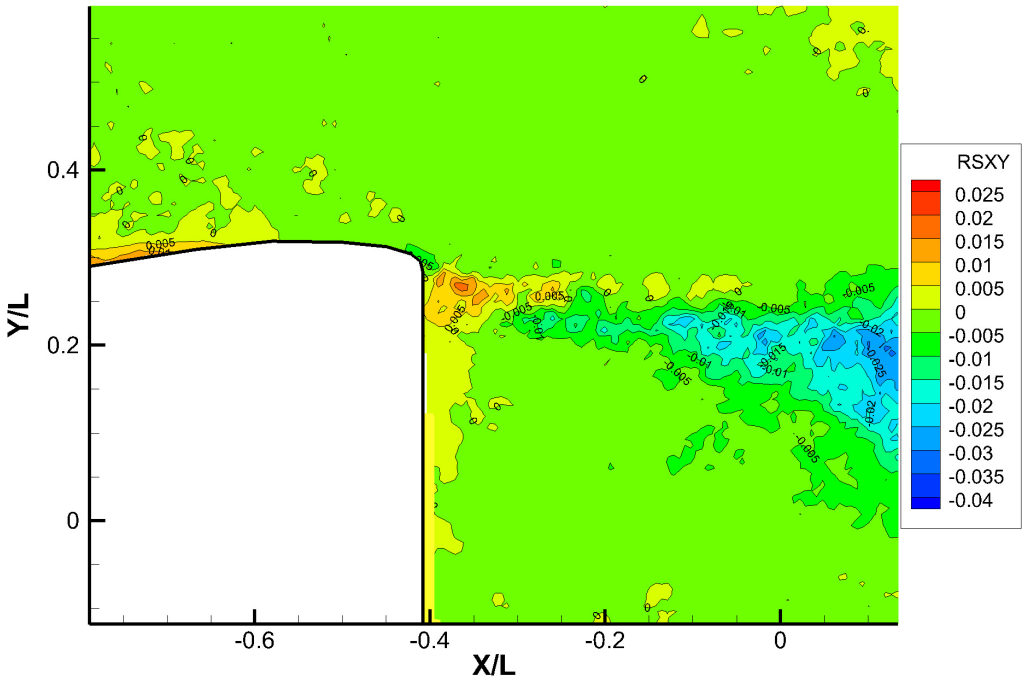

Figure 3.46: Jet2 Mirror $\frac{\overline{u'v'}}{U^2}$ Reynolds Stress contours in the vertical symmetry plane of the wake. V = 30 m/s, Re = 2.55x10^5.

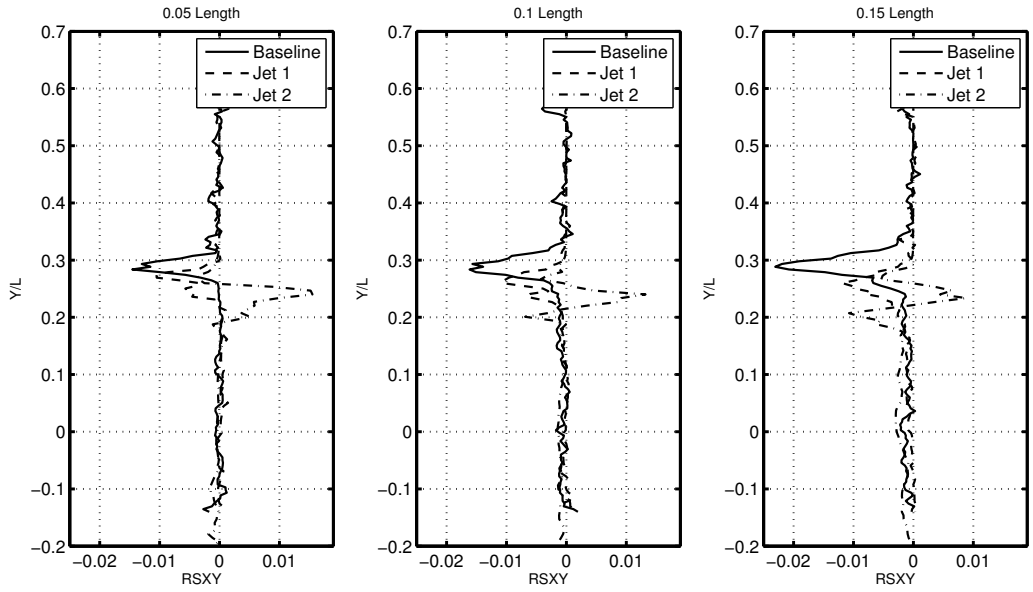

Figure 3.47: $\frac{\overline{u'v'}}{U^2}$ Reynolds Stress profiles for select mirror lengths downstream. V = 30 m/s, Re = 2.55x10^5.

Reynolds stress values for $\frac{\overline{u'w'}}{U^2}$ display similar behavior to what was observed in the in the contour plots for $\frac{\overline{u'u'}}{U^2}$. The high intensity region of the models can be observed to exist in the shear layers between the recirculation region and the free stream. The Baseline model in Figure 3.48 shows relatively low intensity region initiating in from the mirror surface at the area of flow separation and extending downstream in the shear layer. The Jet1 model can be seen to cause values of $\frac{\overline{u'w'}}{U^2}$ to increase in the boundary region of the mirror top surface and cause a localized high intensity region to exist in the immediate mixing region of the wake. Figure 3.50 shows the high intensity values of $\frac{\overline{u'u'}}{U^2}$ for the Jet2 configuration which also coincide with the shear layer for the Jet2 model. Due to larger Inlet/Outlet area, the turbulent shear layer intensity is high in magnitude and in the area as well.

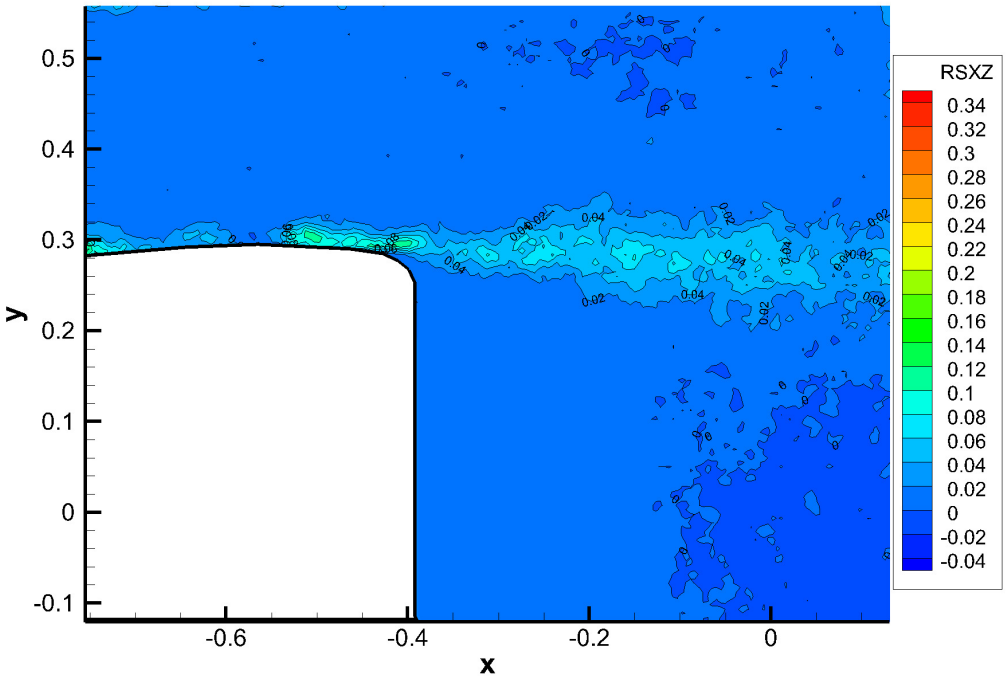

Figure 3.48: Baseline Mirror $\frac{\overline{u'w'}}{U^2}$ Reynolds Stress contours in the vertical symmetry plane of the wake. V = 30 m/s, Re = 2.55x10^5.

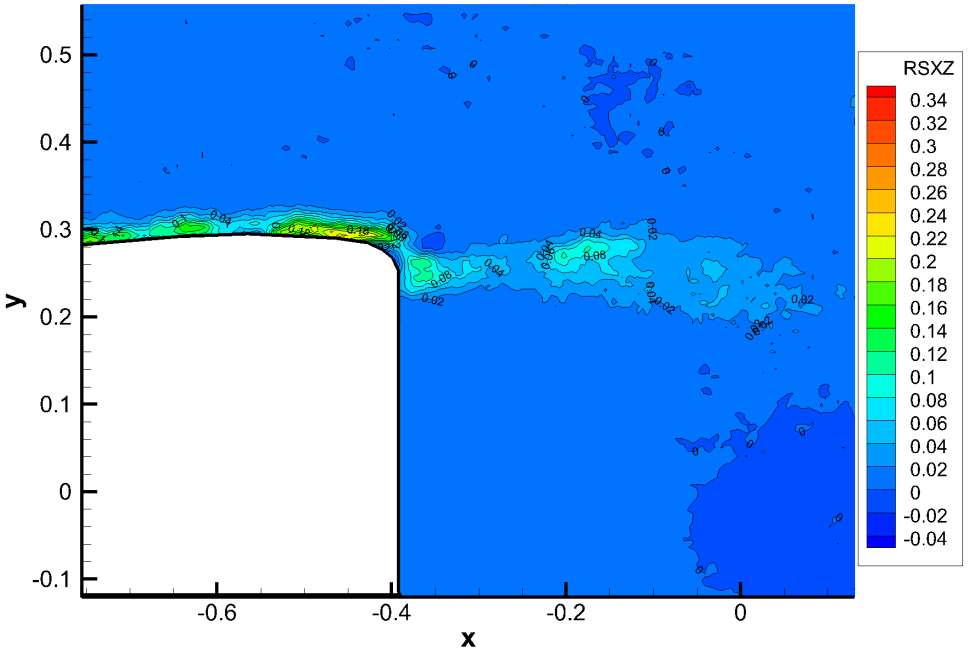

Figure 3.49: Jet1 Mirror $\frac{\overline{u'w'}}{U^2}$ Reynolds Stress contours in the vertical symmetry plane of the wake. V = 30 m/s, Re = 2.55x10^5.

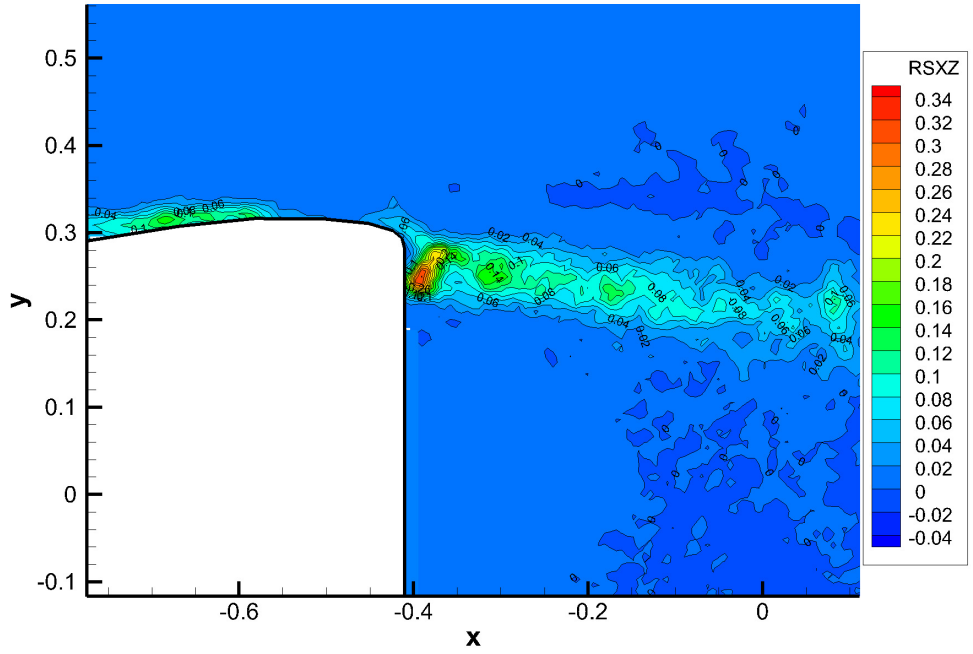

Figure 3.50: Jet2 Mirror $\frac{\overline{u'w'}}{U^2}$ Reynolds Stress contours in the vertical symmetry plane of the wake. V = 30 m/s, Re = 2.55x10^5.

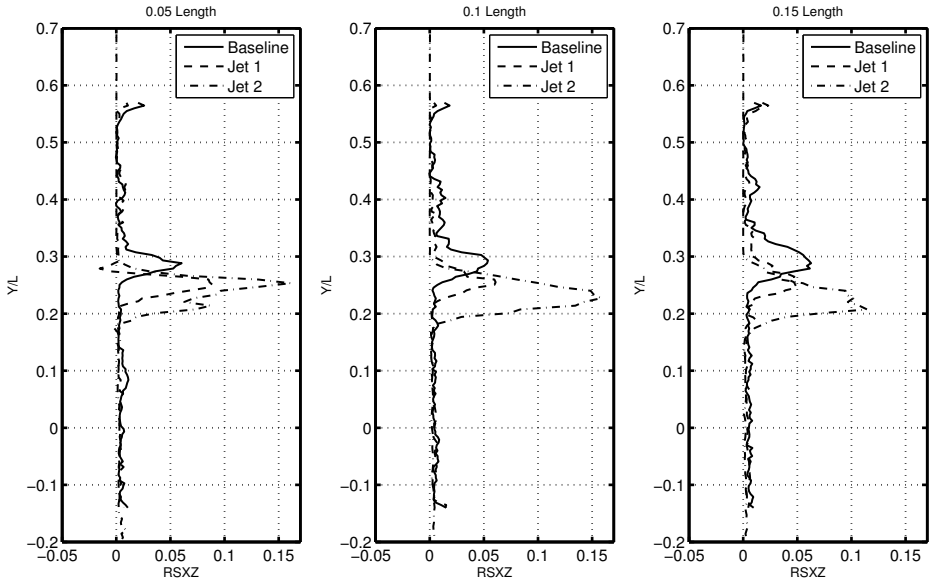

Figure 3.51: $\frac{\overline{u'w'}}{U^2}$ Reynolds Stress profiles for select mirror lengths downstream. V = 30 m/s, Re = 2.55x10^5.

The Reynolds stress values for $\frac{\overline{v'v'}}{U^2}$ also display interesting behavior due to the jet interaction with the shear layer. Observing Figure 3.52 the turbulent intensities for

the shear layer show high intensity regions and a large rate of growth downstream. The shear layer intensities of Figure 3.53 show the Jet1 values for $\frac{\overline{y'y'}}{U^2}$ reduce the not only the growth rate of the high intensity region, but also magnitudes associated with the Reynolds stress as well. In addition to the intensity reduction, the area of high $\frac{\overline{y'y'}}{U^2}$ appears to be curved following the top of the shear layer as it starts to converge to the center of the recirculation region. As seen in Figure 3.52, the Baseline intensity region appears to follow a more linear slope downstream as the shear layer converges. The Jet2 model values for $\frac{\overline{v'v'}}{U^2}$ Reynolds stress can be seen in Figure 3.54. The Jet2 model produces noticeably higher Reynolds stress concentrations associated with the passive jet in the recirculation region of the flow field. Intensity measurements recorded for the Jet2 model can be observed to display much higher values downstream with intensity measurements of .055 for the Jet2 model and .025 for the same relative area in the Jet1 flow stream.

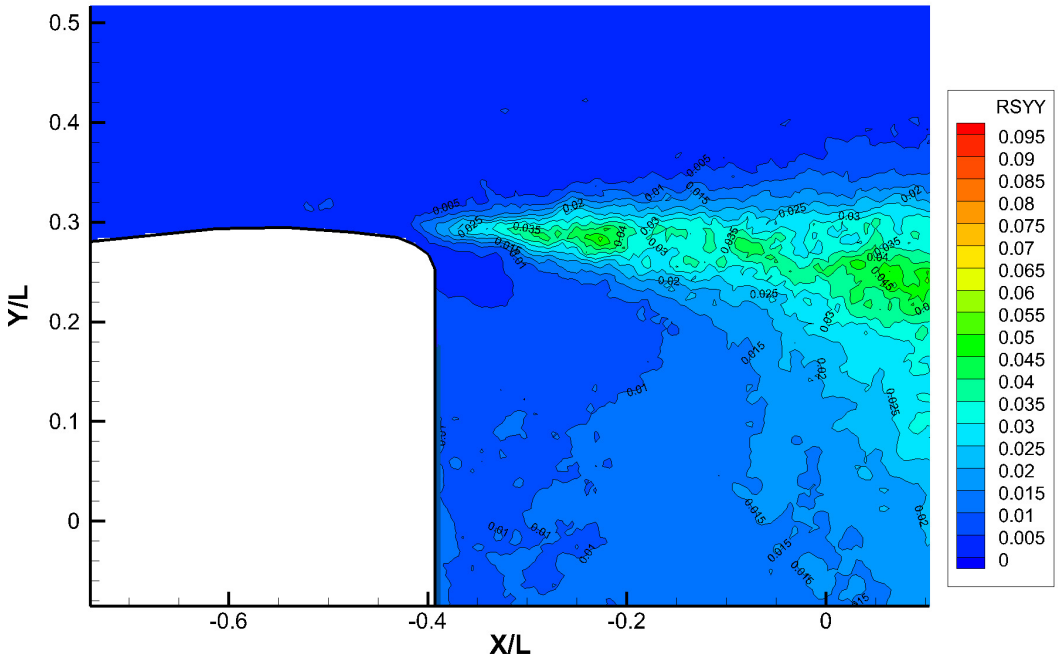

Figure 3.52: Baseline Mirror $\frac{\overline{v'v'}}{U^2}$ Reynolds Stress contours in the vertical symmetry plane of the wake. V = 30 m/s, Re = 2.55x10^5.

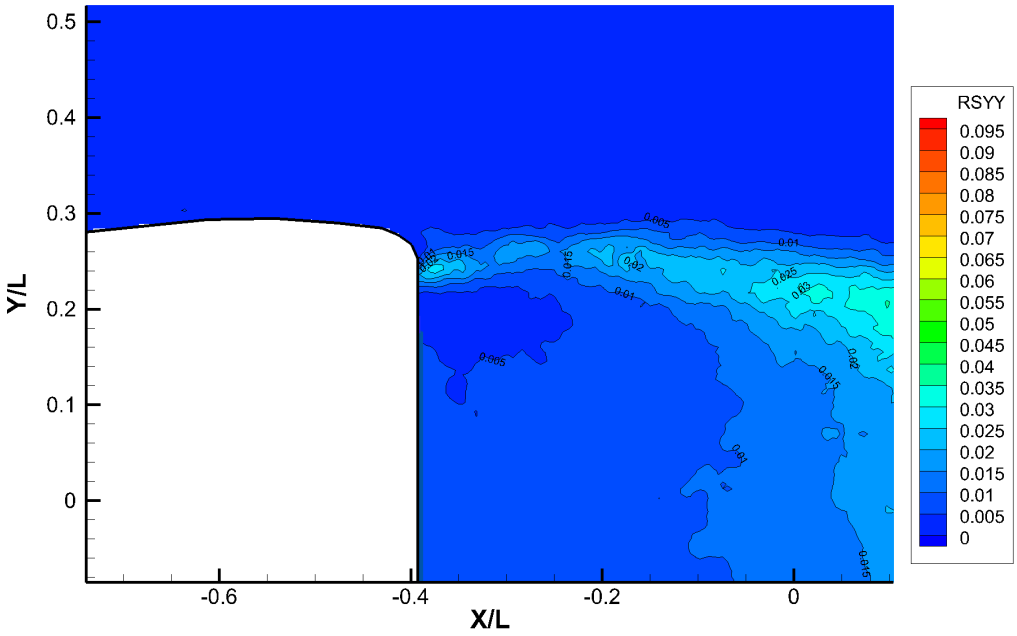

Figure 3.53: Jet1 Mirror $\frac{\overline{v'v'}}{U^2}$ Reynolds Stress contours in the vertical symmetry plane of the wake. V = 30 m/s, Re = 2.55x10^5.

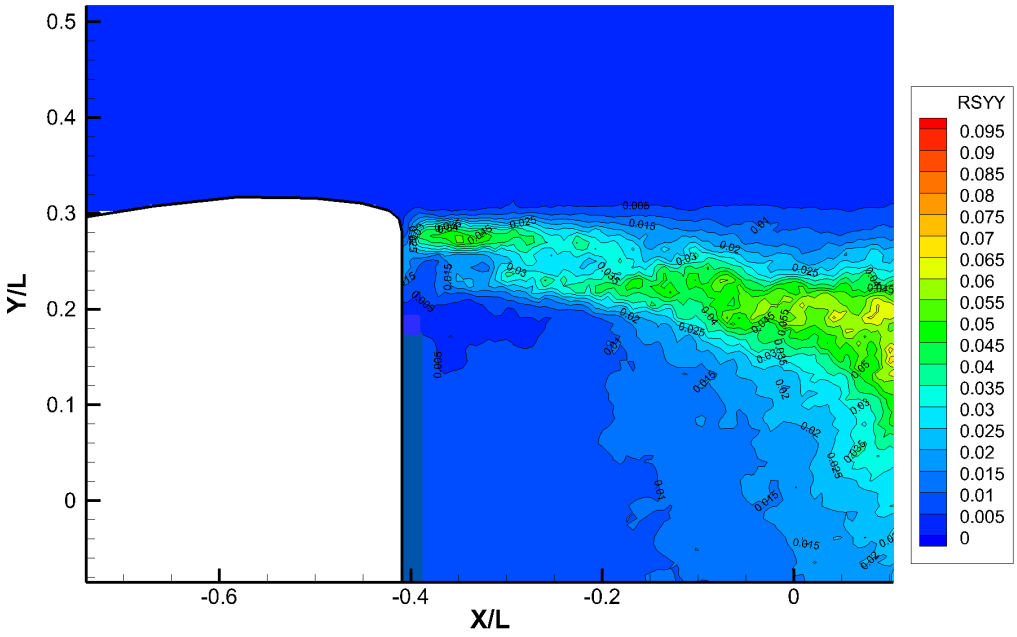

Figure 3.54: Jet2 Mirror$\frac{\overline{v'v'}}{U^2}$ Reynolds Stress contours in the vertical symmetry plane of the wake. V = 30 m/s, Re = 2.55x10^5.

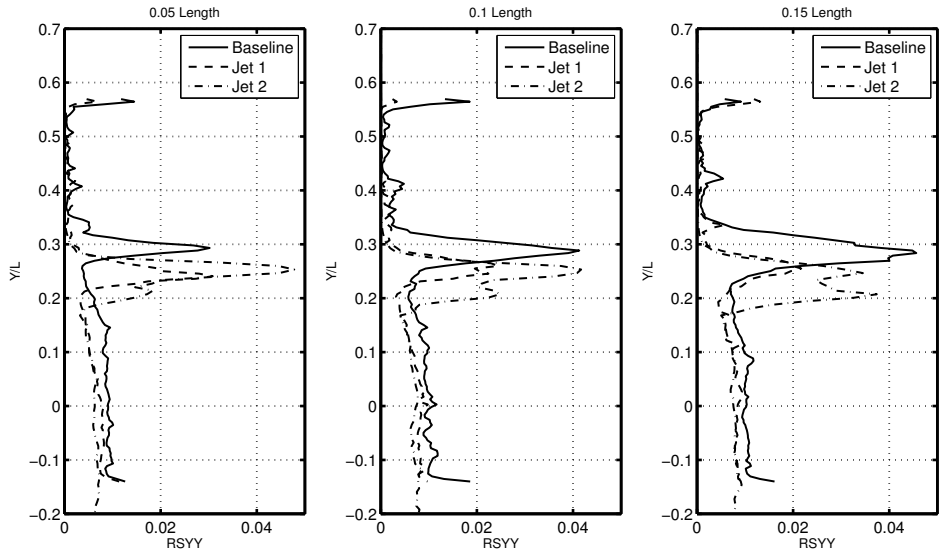

Figure 3.55: $\frac{\overline{v'v'}}{U^2}$ profles for select mirror lengths downstream. V = 30 m/s, Re = 2.55x10^5.

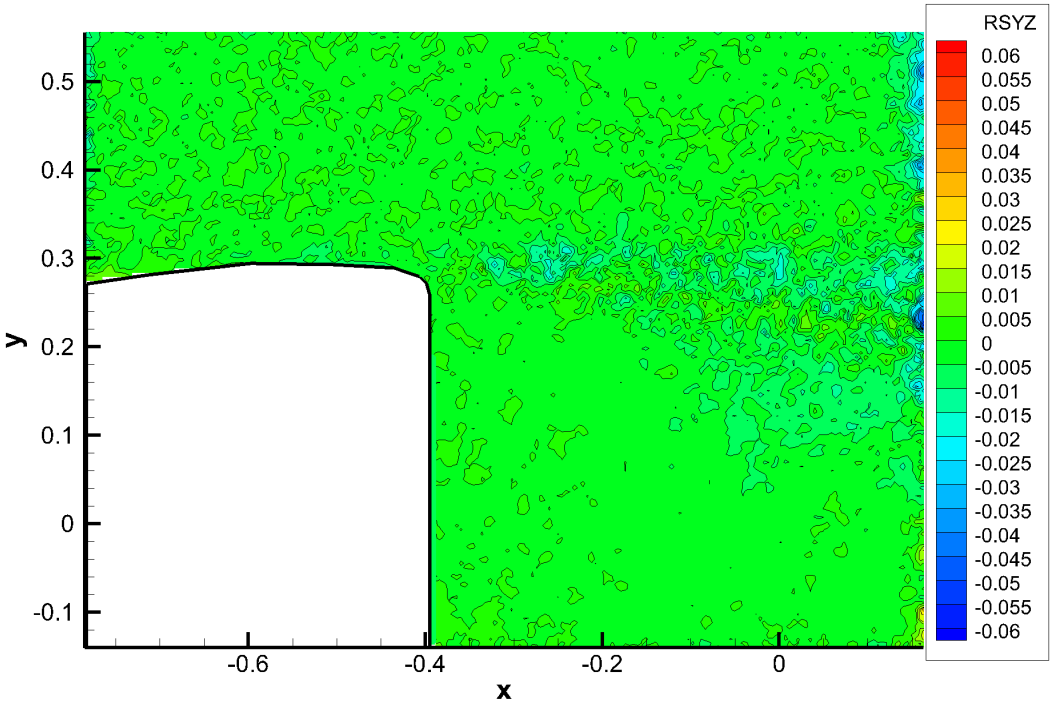

Figure 3.56: Baseline Mirror $\frac{\overline{v'z'}}{U^2}$ Reynolds Stress contours in the vertical symmetry plane of the wake. V = 30 m/s, Re = 2.55x10^5.

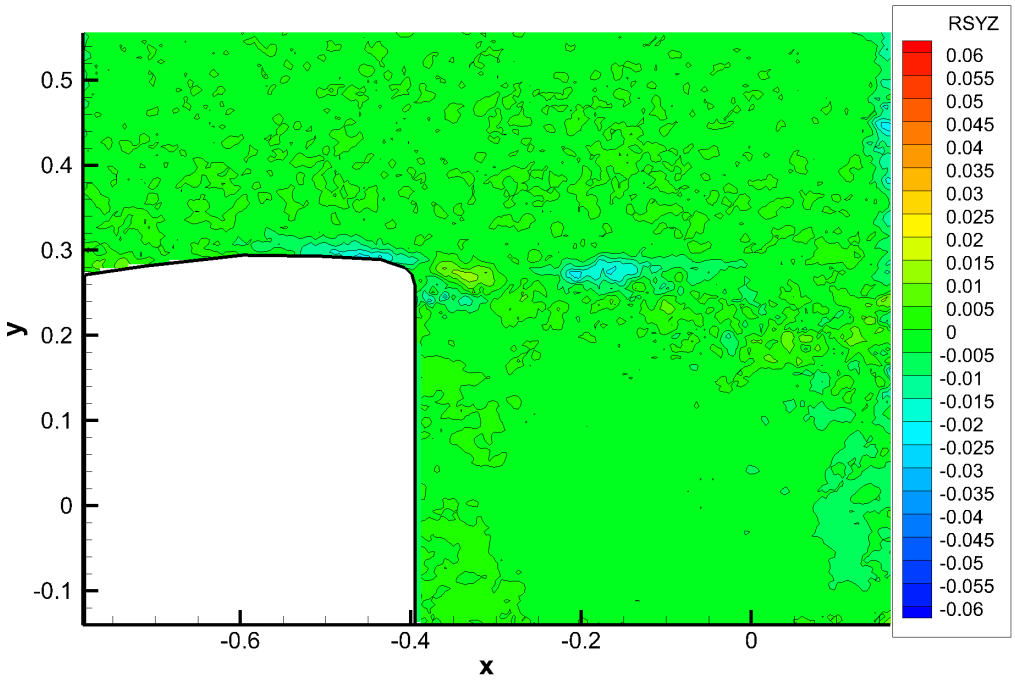

Figure 3.57: Jet1 Mirror $\frac{\overline{v'z'}}{U^2}$ Reynolds Stress contours in the vertical symmetry plane of the wake. V = 30 m/s, Re = 2.55x10^5.

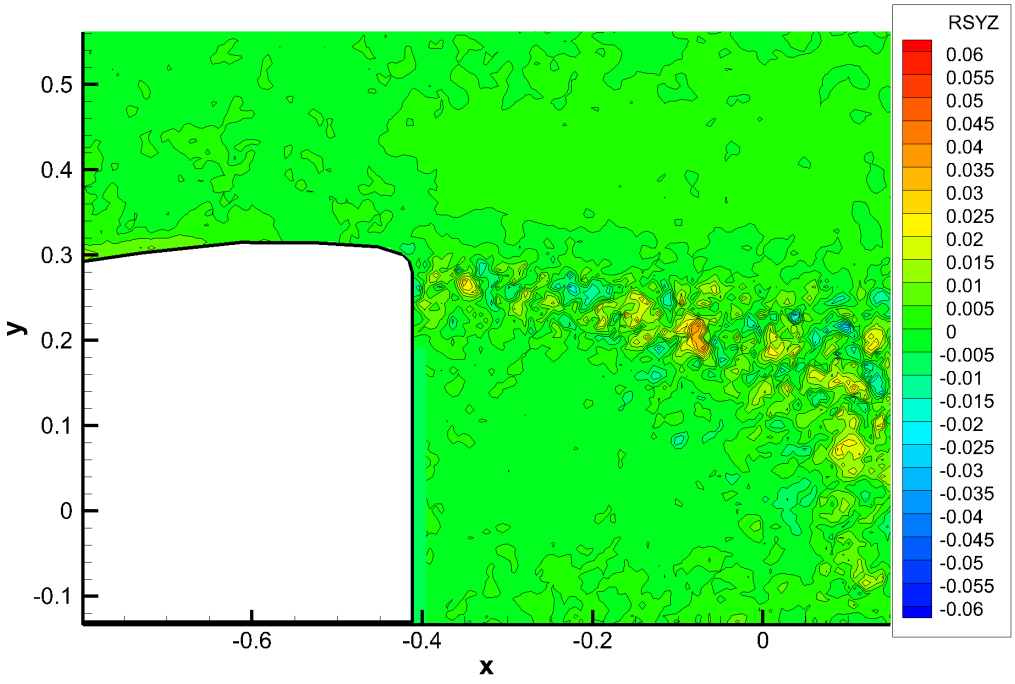

Figure 3.58: Jet2 Mirror$\frac{\overline{v'z'}}{U^2}$ Reynolds Stress contours in the vertical symmetry plane of the wake. V = 30 m/s, Re = 2.55x10^5.

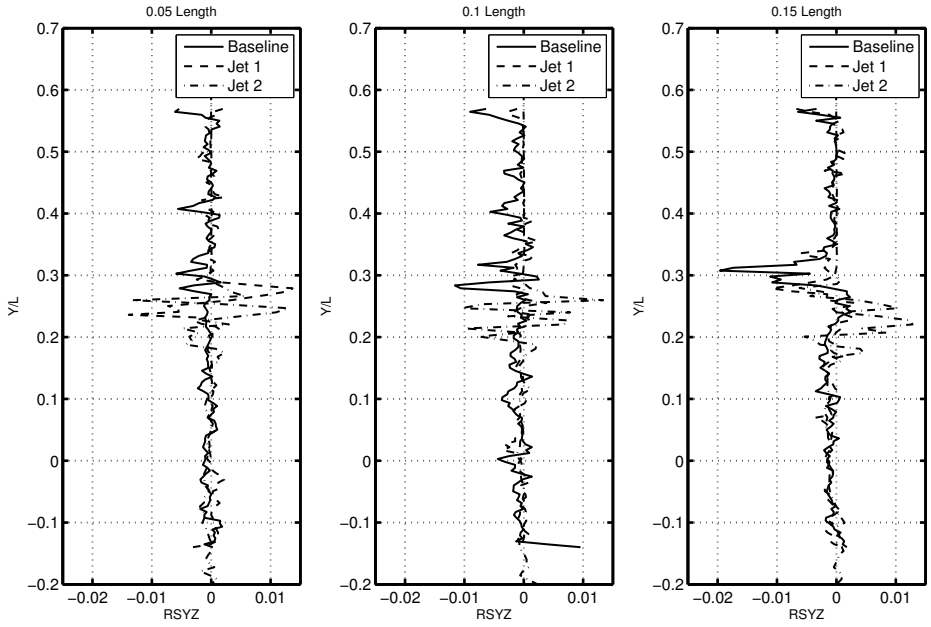

Figure 3.59: $\frac{\overline{v'z'}}{U^2}$ Reynolds Stress contours in the vertical symmetry plane of the wake. V = 30 m/s, Re = 2.55x10^5.

The following figures show the values for $\frac{\overline{w'w'}}{U^2}$ for all three models under investigation. The Baseline model shows high intensity regions in the shear layer developed by the free stream and the recirculation region. The undisturbed mixing layer that develops in the Baseline model shows no signs of increased normal stress in the boundary region on the mirror top surface. Observing Figure 3.61, the jet increases the turbulent fluctuation in of the $\frac{\overline{z'z'}}{U^2}$ values where the jet mixes with the shear layer in addition to the region on the mirror surface .1 mirror lengths before the trailing edge of the model. Downstream from the rear of the mirror rear surface, the intensity of the $\frac{\overline{z'z'}}{U^2}$ values for the Jet1 model display a reduction in the normal stress recorded in addition to the area it is applied to. The Jet1 model displays a region of increased values for the $\frac{\overline{z'z'}}{U^2}$ normal stress close to the mirror rear surface whereas the Baseline model displays increased values downstream in the shear layer. The Jet2 model can be observed in Figure 3.62. The intensities of the normal stress are greatly increased when compared to the Jet1 model and also display a region of peak values in the mixing region close to the trailing edge of the model. The high Inlet/Outlet ration of the Jet2 configuration displays not only an increase in the normal stress values concentrated in the mixing

layer, but an increase in the $\frac{\overline{z'z'}}{U^2}$ area where the elevated values are measured.

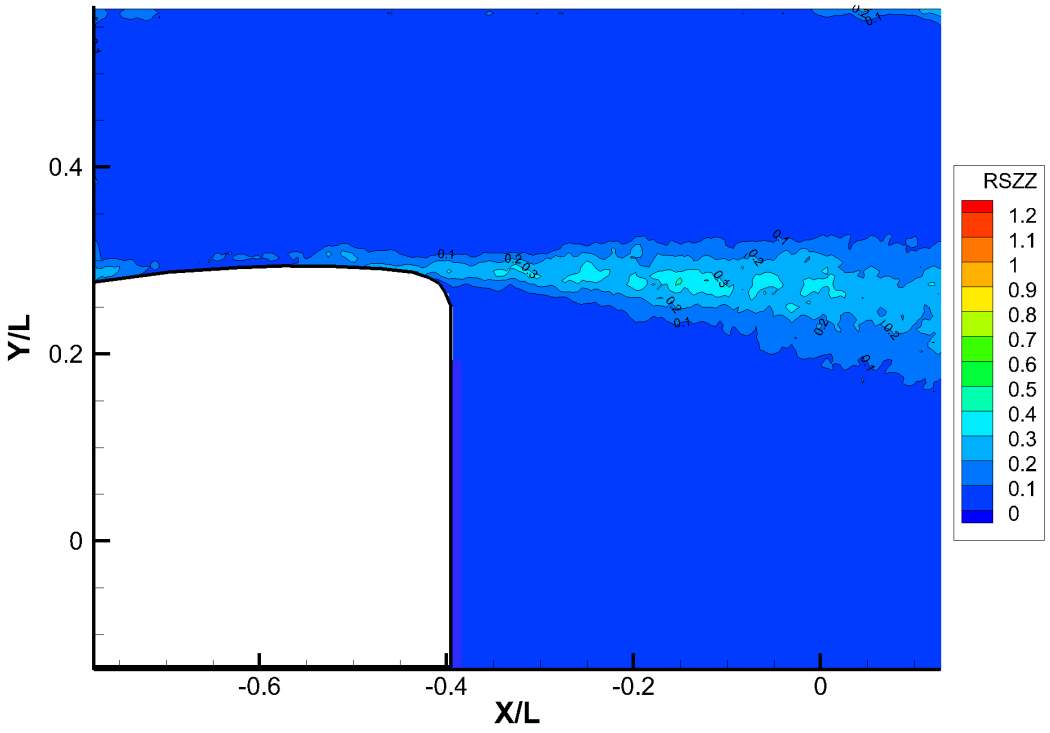

Figure 3.60: Baseline Mirror $\frac{\overline{w'w'}}{U^2}$ Reynolds Stress contours in the vertical symmetry plane of the wake. V = 30 m/s, Re = 2.55x10^5.

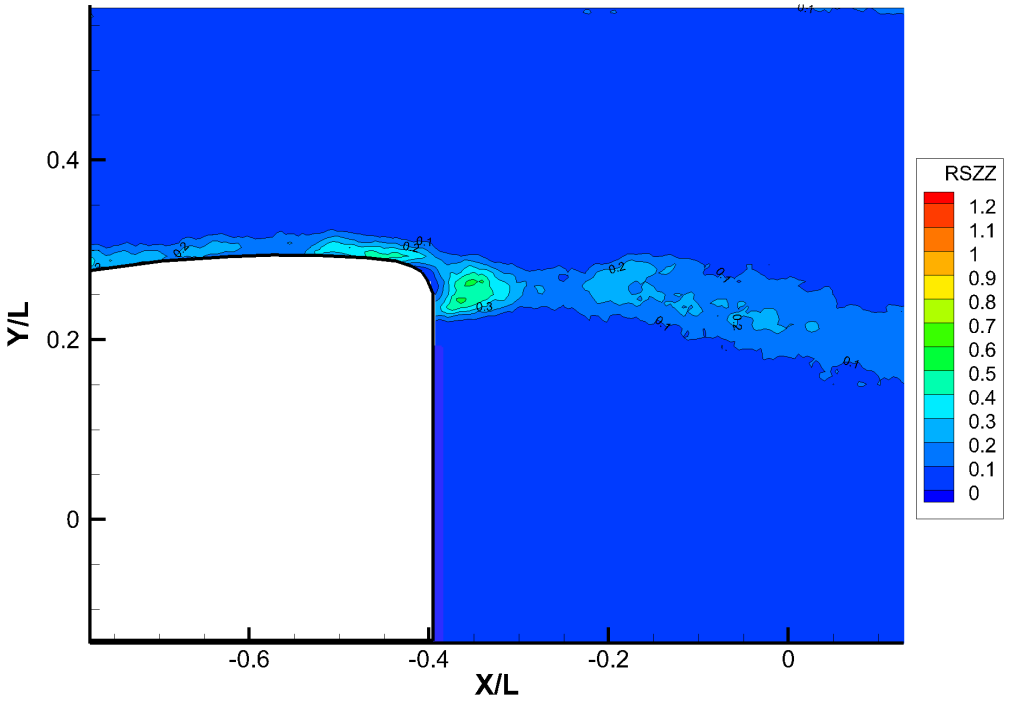

Figure 3.61: Jet1 Mirror $\frac{\overline{w'w'}}{U^2}$ Reynolds Stress contours in the vertical symmetry plane of the wake. V = 30 m/s, Re = 2.55x10^5.

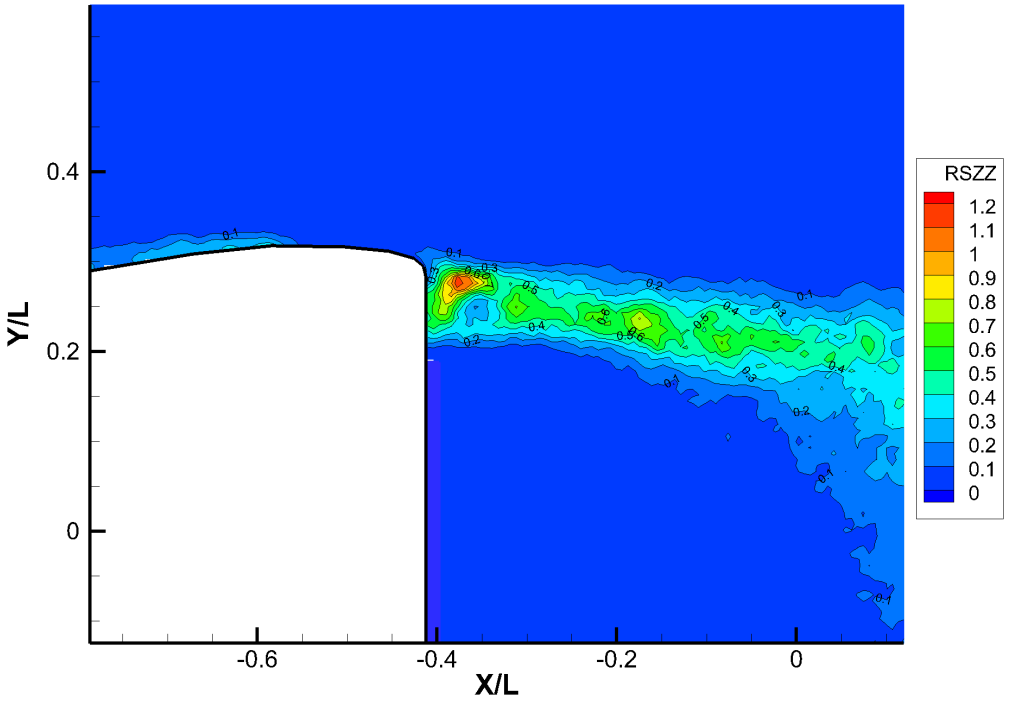

Figure 3.62: Jet2 Mirror $\frac{\overline{w'w'}}{U^2}$ Reynolds Stress contours in the vertical symmetry plane of the wake. V = 30 m/s, Re = 2.55x10^5.

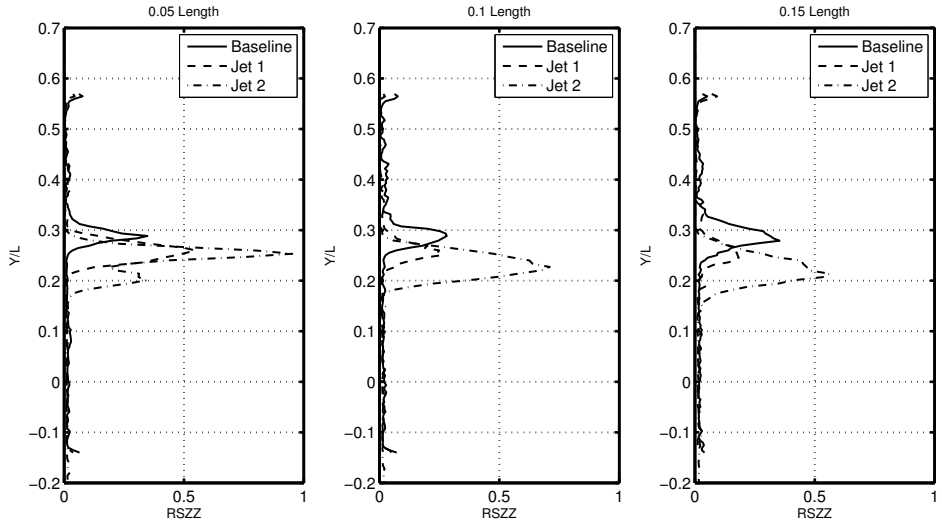

Figure 3.63: $\frac{\overline{w'w'}}{U^2}$ Reynolds Stress contours in the vertical symmetry plane of the wake. V = 30 m/s, Re = 2.55x10^5.

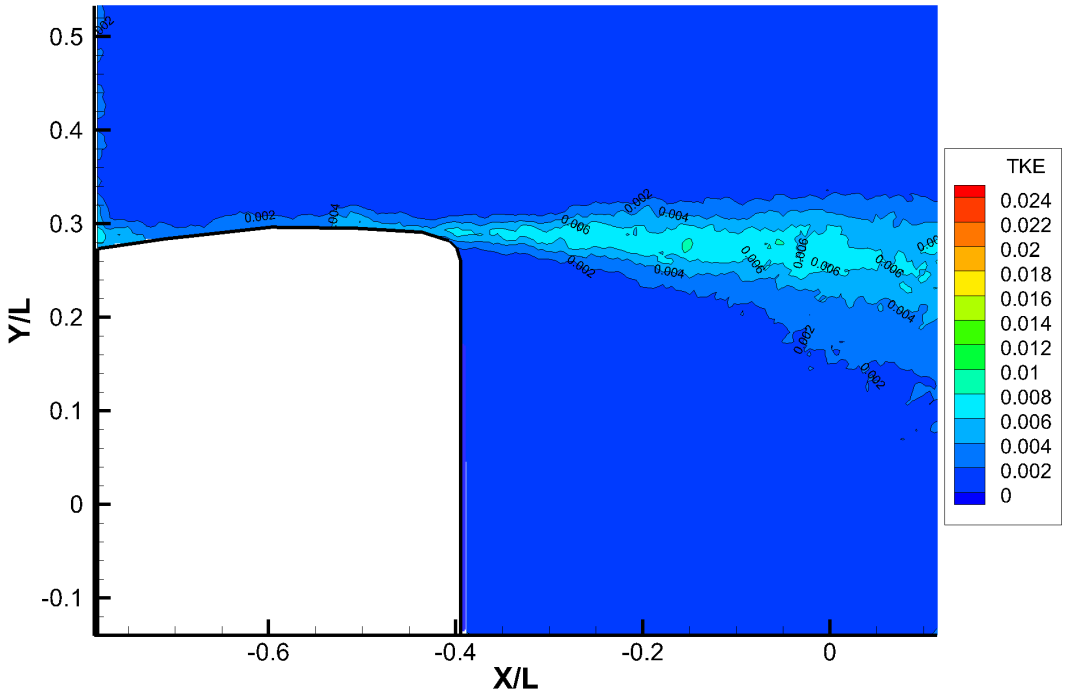

Figure 3.64: Baseline Mirror Turbulent Kinetic Energy contours in the vertical symmetry plane of the wake. V = 30 m/s, Re = 2.55x10^5.

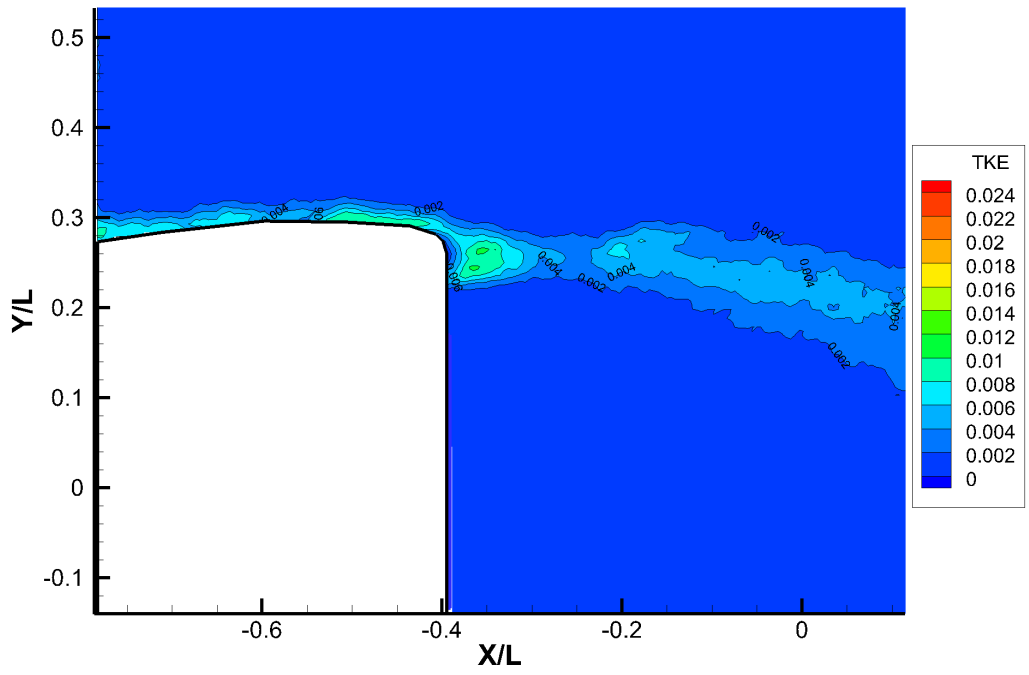

Figure 3.65: Jet1 Mirror Turbulent Kinetic Energy contours in thevertical symmetry plane of the wake. V = 30 m/s, Re = 2.55x10^5.

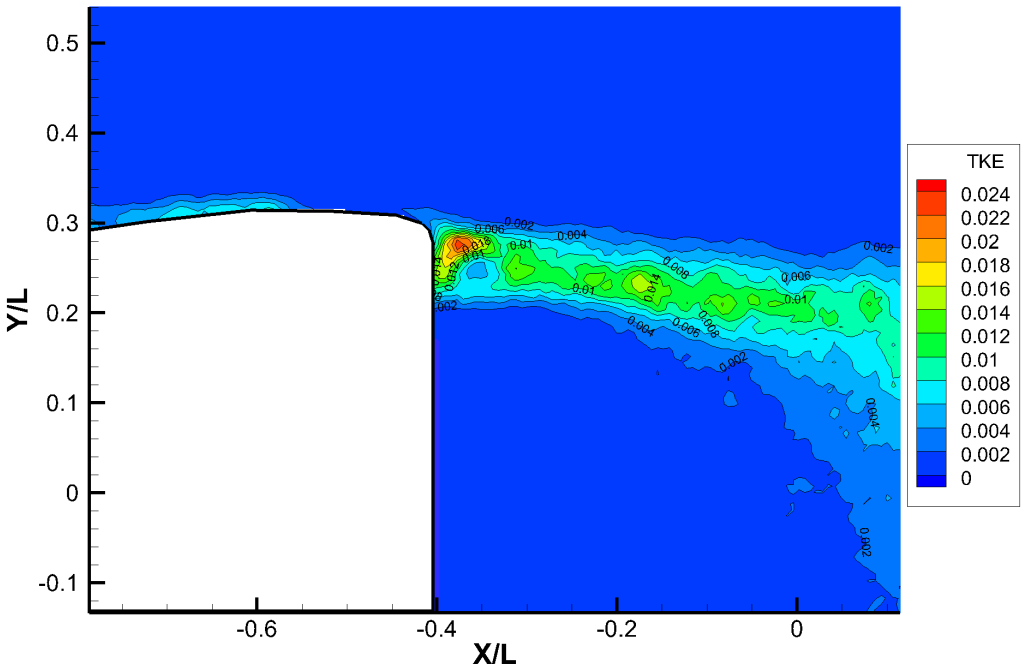

Figure 3.66: Jet2 Mirror Turbulent Kinetic Energy contours in the vertical symmetry plane of the wake. V = 30 m/s, Re = 2.55x10^5.

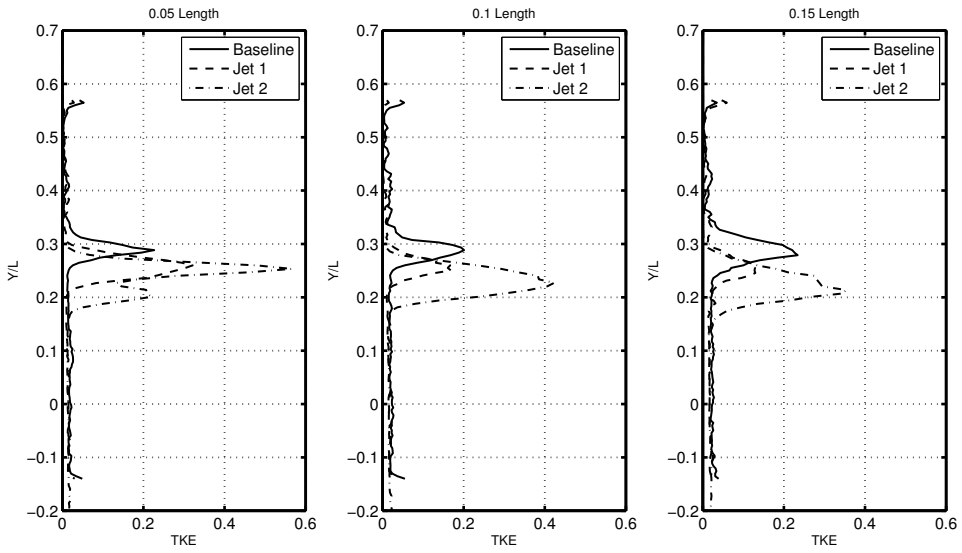

Figure 3.67: Turbulent Kinetic Energy profles for select mirror lengths downstream. V = 30 m/s, Re = 2.55x10^5.

3.0.9 Offset Velocity Profiles

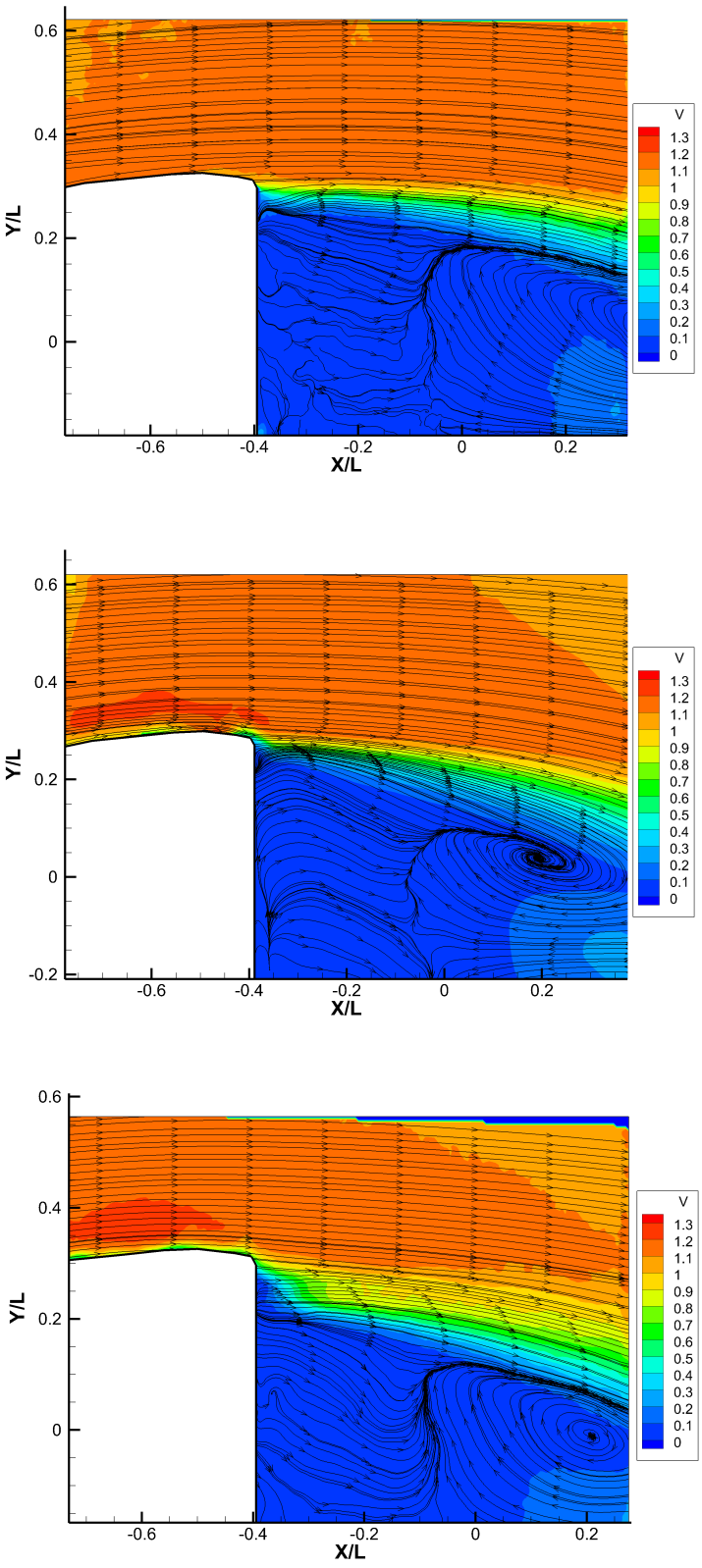

Figure 3.68: Baseline, Jet1 and Jet2 Mirrors at 21.55mm offset from the centerline Z=0 plane. V= 30 m/s Re = 2.55×10^5.

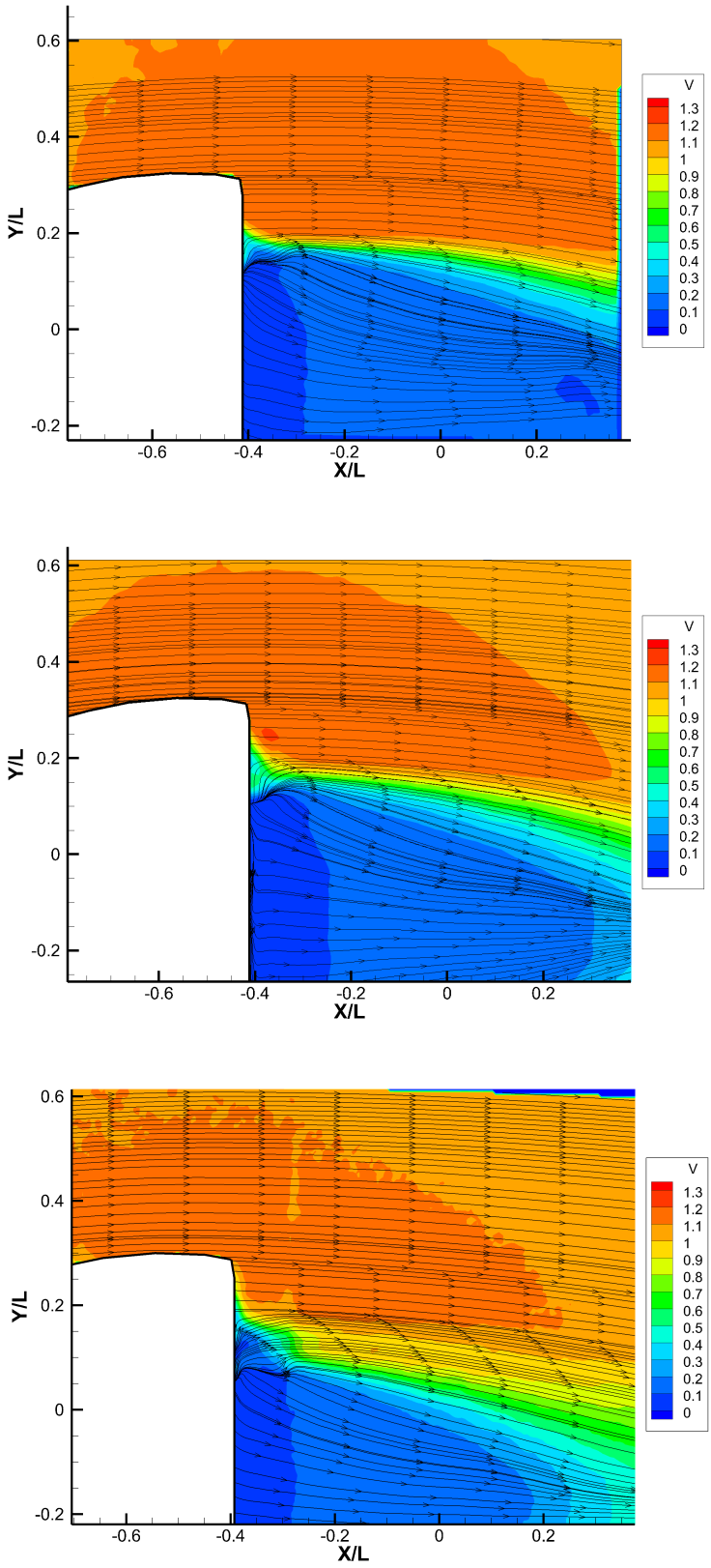

Figure 3.69: Baseline, Jet1 and Jet2 Mirrors at 43.10mm offset from the centerline Z=0 plane. V= 30 m/s Re = 2.55×10^5.

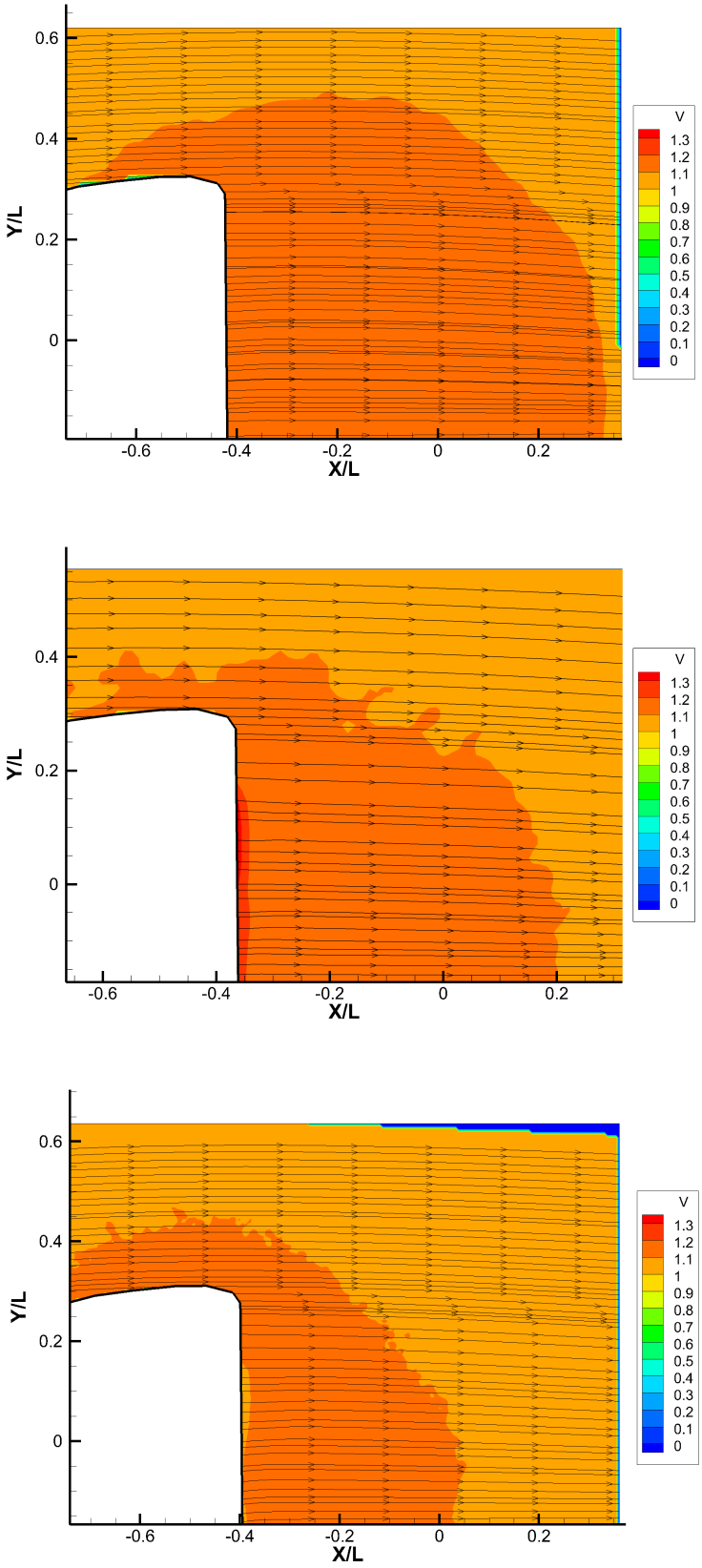

Figure 3.70: Baseline, Jet1 and Jet2 Mirrors at 67.65mm offset from the centerline Z=0 plane. V= 30 m/s Re = 2.55×10^5.

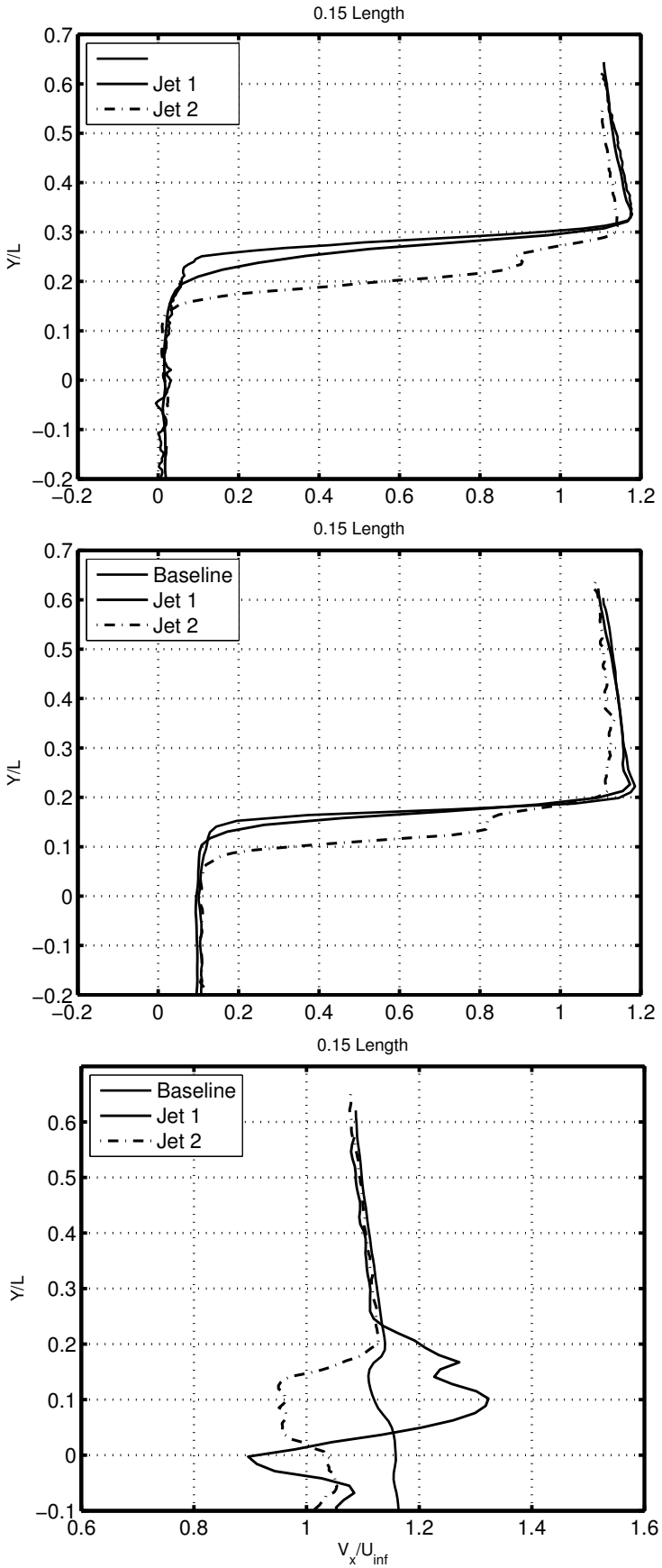

Figure 3.71: Baseline, Jet1 and Jet2 Mirrors Vx velocity profile at a) 21.55mm, b) 43.10mm, and c) 67.65mm from the centerline Z=0 plane. V= 30 m/s Re = 2.55×10^5.

3.0.10 POD Analysis

The POD analysis for the three models tested can be observed in the Figures 3.72 to Figures 3.92 where the reconstruction of the Reynolds Stress data is displayed for the Spatial Eigenmodes 1,2,3 4,5,6 100, 300 of the 400 image data set. Figure 3.72 indicates the first successive modes in the series contain a larger percentage of the energy associated with the flow in the near wake region of the mirror body than the remaining modes. It has been demonstrated through previous experimentation that more complex flow patterns will have a higher order modal energy distribution, whereas flow with less complex behavior will have a large percentage of the modal energy distributed amongst the first modes in the series [4]. From the data observed for the baseline wake region, the flow behind the baseline mirror can be seen as a higher order flow field in which the first 6 modes contain 14.6% of the fluctuation energy and the first 50 modes contain more than 45% of the total fluctuation energy.

The first 6 modes for the Jet1 model contain 13.2% of the fluctuation energy, a 1.4% decrease from the first 6 modes of than the baseline model. Additionally, the first 50 modes contain more than 42% of the total fluctuating energy which is also lower the Baseline model by 3.4% of the total fluctuation energy. The first six modes of the Jet2 model contain 10.7% of the total fluctuation energy which is lower than the Baseline model's first 6 model by 3.9%. Similar to the flow behavior in the Jet1 configuration, the first 50 modes of the Jet2 configuration show a 3.6% reduction in the modal energy of the Baseline model for a total fluctuation energy of 41.7%. This data indicates that the wake of the Jet1 model is more complex than that of the Baseline configuration due to the passive flow control implemented through the circumferential jet. In addition to this, in spite of the high inlet to outlet ratio of the Jet2 model, the Jet2 wake region is only slightly more complex than that of the Jet1 wake region as seen by the higher fluctuation energy percentage of the earlier series of Eigenfunction modes associated with the Jet2 configuration. It can also be observed in the modal data that the modal energy percentage converges for all three models to almost the same value by the 300th mode. For the Baseline model, 94% of the fluctuation energy is

contained in the 300th mode which is.6% higher than the Jet1 configuration at 93.4% of the fluctuation energy. The Jet1 and Jet2 models can again be seen to create a more complex flow field in the immediate wake region downstream of the mirror trailing edge than that of the Baseline configuration as a higher number of modes is still required to account for the modal energy of the flow in the recirculation region. The difference between the Jet1 and Jet2 configurations at 300 modes is .62%. Table 3.2 shows the corresponding energy associated with each mode mentioned and their difference with respect to each model.

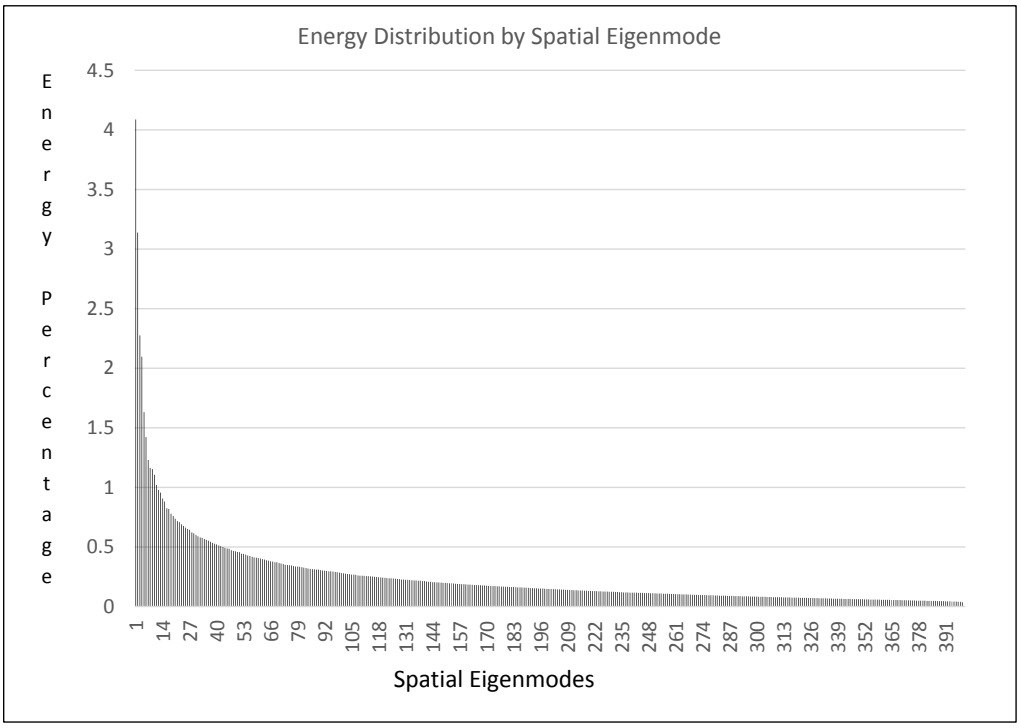

Figure 3.72: Baseline POD Energy Distribution by Spatial Eigenmode. V= 30 m/s Re = $2.55x10^5$.

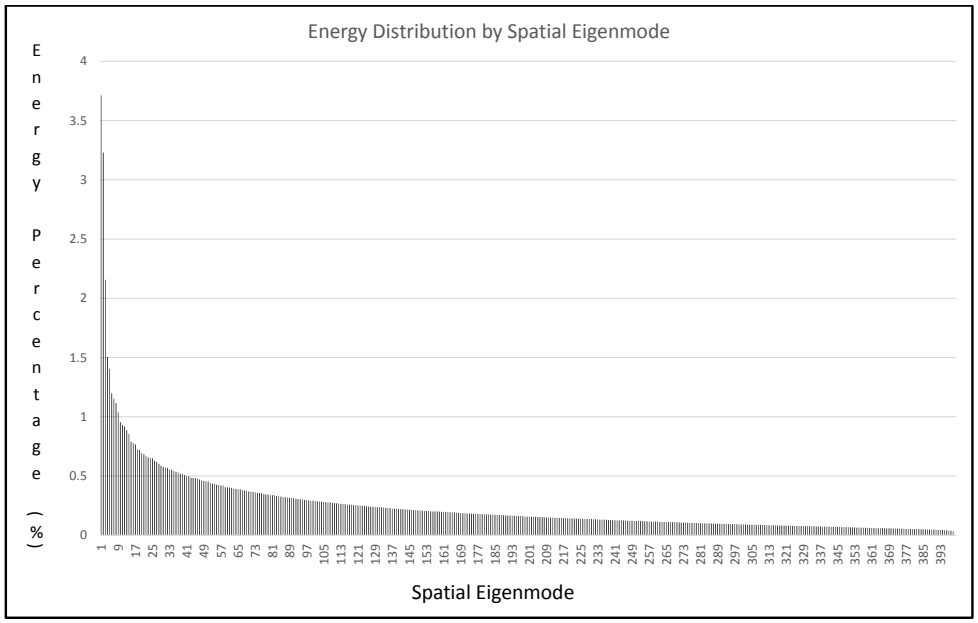

Figure 3.73: Jet1 POD Energy Distribution by Spatial Eigenmode. V= 30 m/s Re = 2.55×10^5.

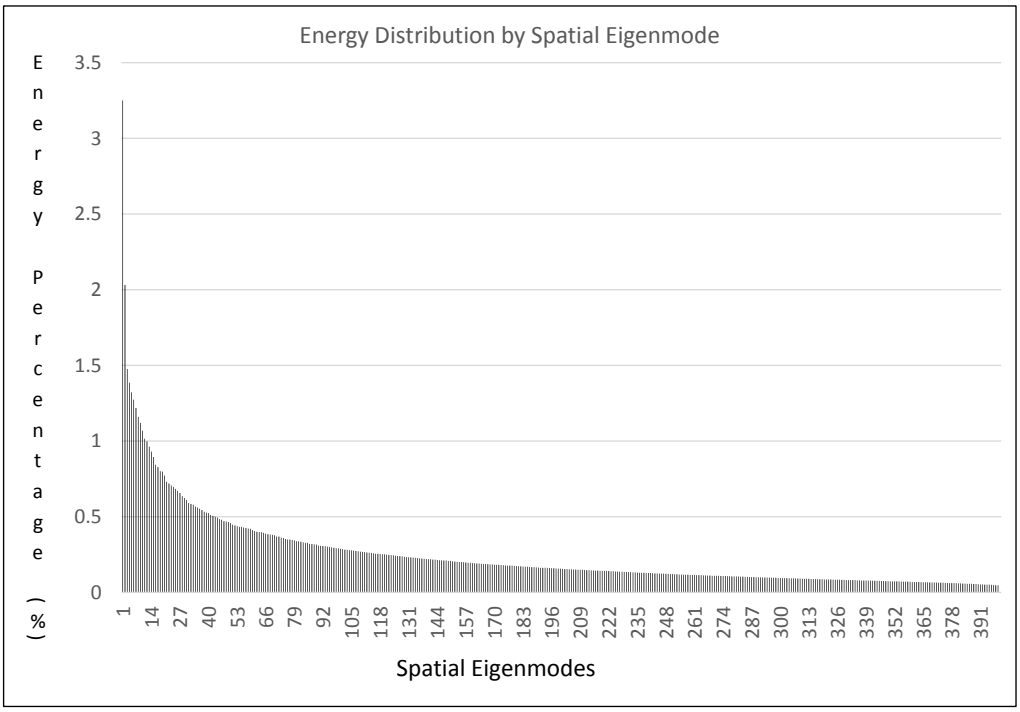

Figure 3.74: Jet2 POD Energy Distribution by Spatial Eigenmode. V= 30 m/s Re = 2.55x10^5.

Model	BL	Jet1	Jet2	Δ Jet1	ΔJet2	Δ Jet1-Jet2
6	14.6 %	13.2 %	10.7 %	1.4 %	3.9 %	2.4 %
50	45.4 %	42.0 %	41.7 %	3.4 %	3.6 %	.26 %
100	61.7 %	59.9 %	59. 6%	1.8 %	2.1 %	.35 %
300	94.0 %	93.4 %	92.8 %	.6 %	1.2 %	.62 %

Table 3.2: Percentage of energy captured by spatial eigenmodes for Baseline, Jet1 and Jet2 mirrors. The differences between each model is also presented as well.

The modal energy contribution to corresponding measured Reynolds stress in different locations downstream of the trailing edge of the mirror are displayed in the subsequent Figures. The behavior is consistent across the three models. As the modal energy increases, the Reynolds stress distributions converge to the experimental value. Figure3.75 shows the Baseline Reynolds stress profile contribution of the modes 1, 2, 3, 4, 5, 6, 100 and 300 for the $\frac{\overline{u'u'}}{U^2}$ normal stress components. It can be observed that although 100 modes consists of 61.7% of the total energy associated with the baseline model, the Reynolds stress profile is significantly reduced when compared to the

experimentally measured profile. This behavior suggests that the higher order modes and the flow behavior associated with them contribute significantly in creating Reynolds stress values of that region. For the Jet1 and Jet2 configuration, the Reynolds stress profiles can also be observed in Figures 3.81 - Figures 3.92. These profiles show that for both passive jet models, 100 modes do not effectively capture the energy in the wake flow. Figure 3.84 indicates that the remaining higher order modes are required in order to fully recreate the $\frac{\overline{y'y'}}{U^2}$ Reynolds stress profile for the Jet1 configuration suggesting the energy is due to the small scale fluctuations rather than large scale fluctuations.

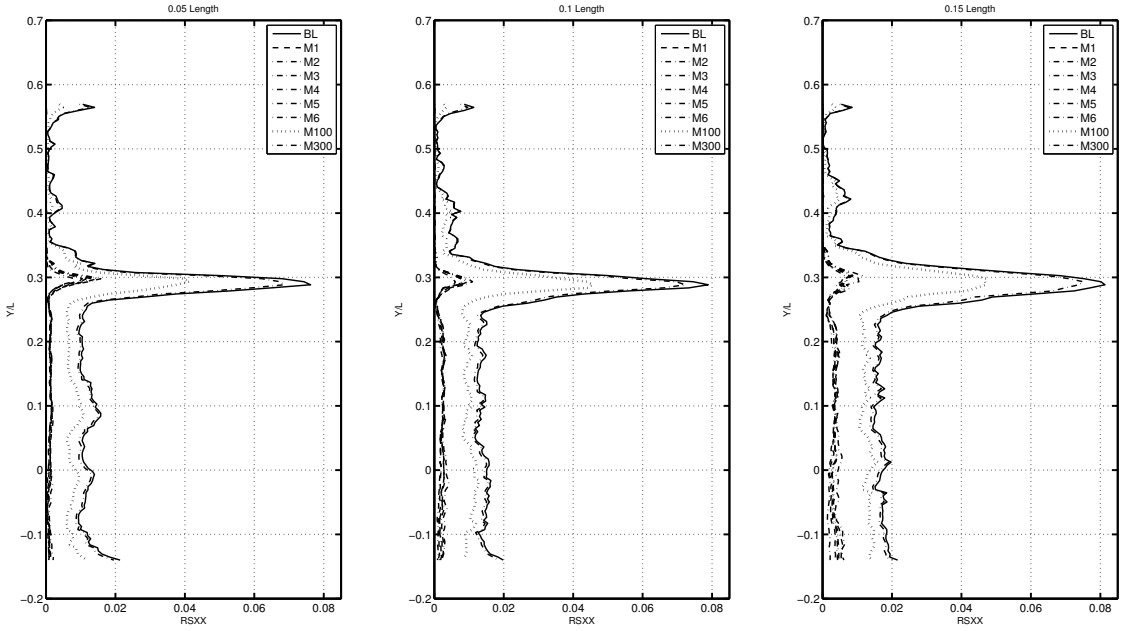

Figure 3.75: Baseline mirror mean POD reconstructed $\frac{\overline{u'u'}}{U^2}$ Reynolds Stress profiles in the vertical symmetry plane of the wake. V= 30 m/s Re = 2.55x10^5.

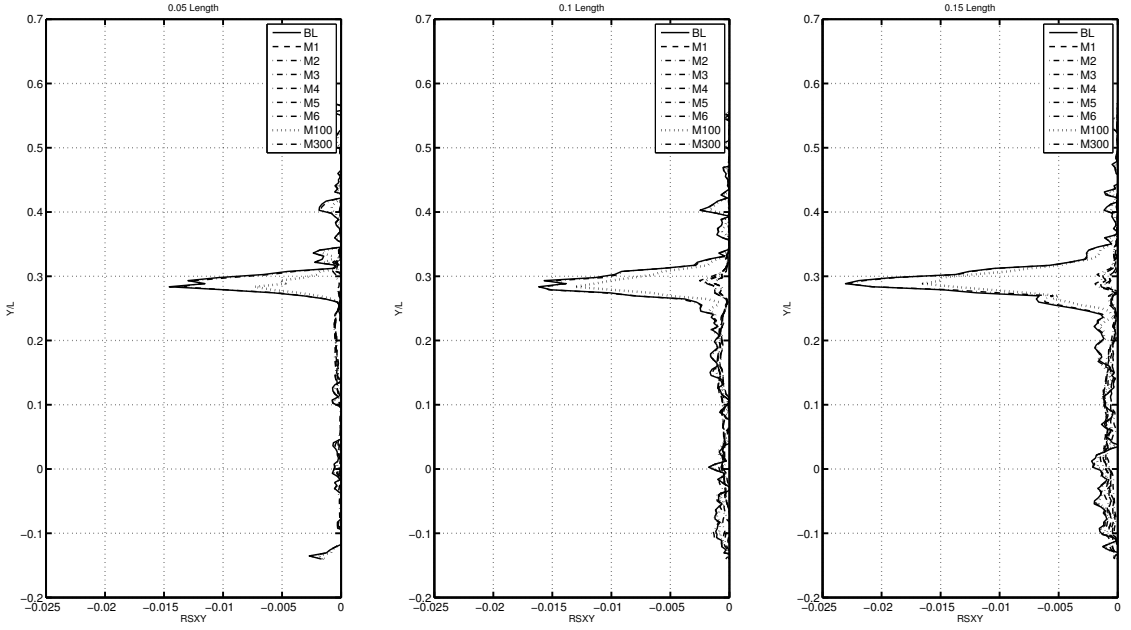

Figure 3.76: Baseline mirror mean POD reconstructed $\frac{\overline{u'v'}}{U^2}$ Reynolds Stress profiles in the vertical symmetry plane of the wake. V= 30 m/s Re = 2.55x10^5.

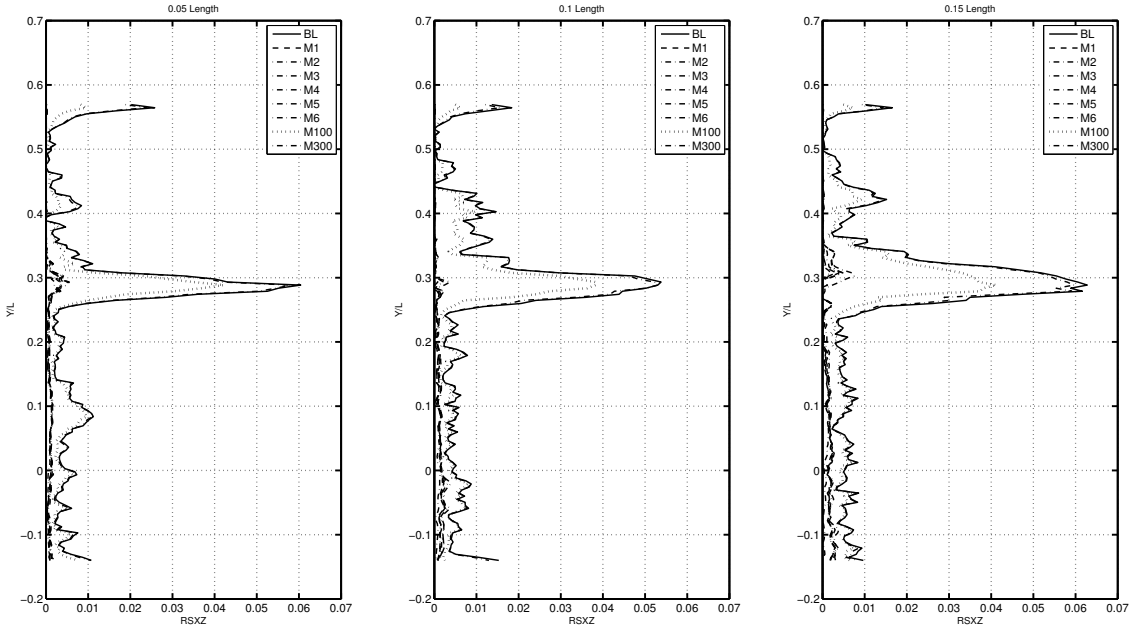

Figure 3.77: Baseline mirror mean POD reconstructed $\frac{\overline{u'w'}}{U^2}$ Reynolds Stress profiles in the vertical symmetry plane of the wake. V= 30 m/s Re = 2.55x10^5.

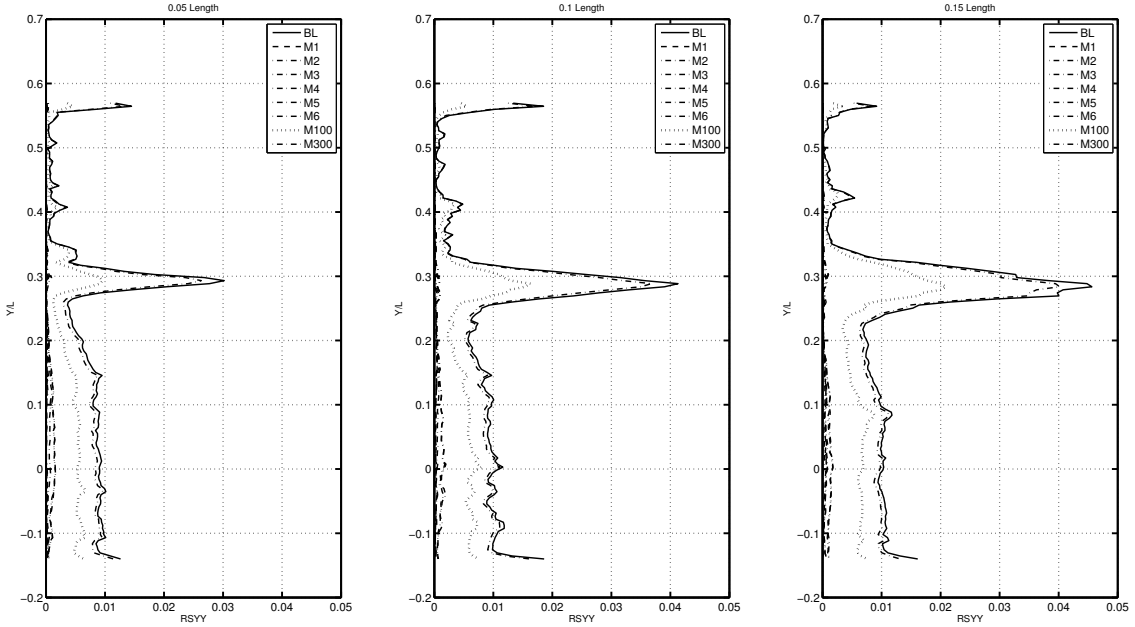

Figure 3.78: Baseline mirror mean POD reconstructed $\frac{\overline{v'v'}}{U^2}$ Reynolds Stress profiles in the vertical symmetry plane of the wake. V= 30 m/s Re = 2.55x10^5.

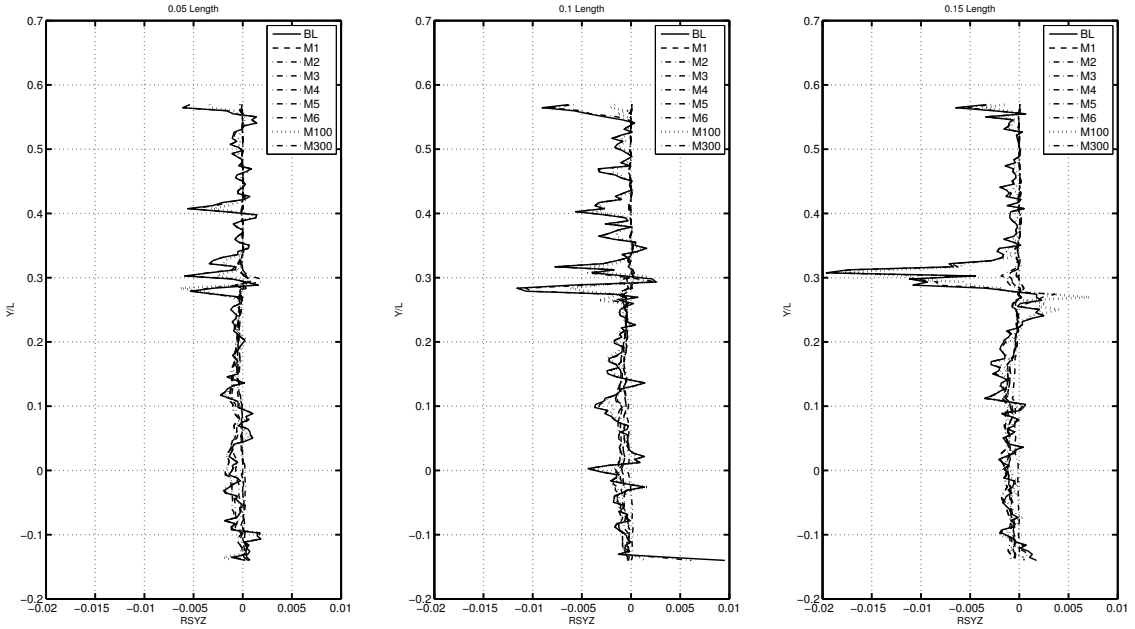

Figure 3.79: Baseline mirror mean POD reconstructed $\frac{\overline{v'w'}}{U^2}$ Reynolds Stress profiles in the vertical symmetry plane of the wake. V= 30 m/s Re = 2.55x10^5.

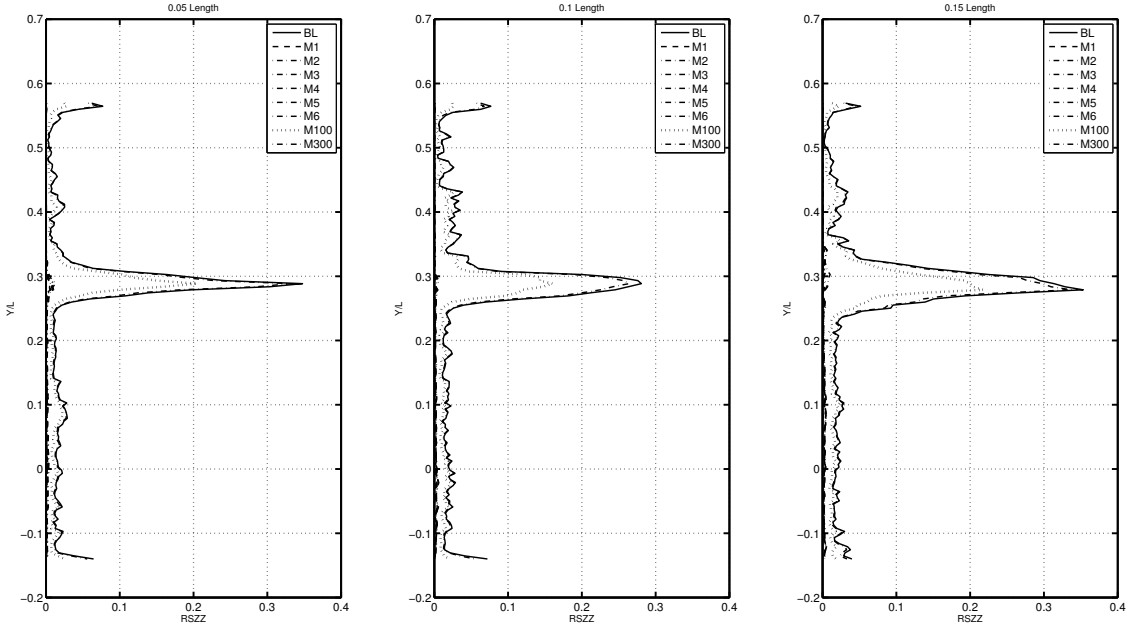

Figure 3.80: Baseline mirror mean POD reconstructed $\frac{\overline{w'w'}}{U^2}$ Reynolds Stress profiles in the vertical symmetry plane of the wake. V= 30 m/s Re = 2.55x10^5.

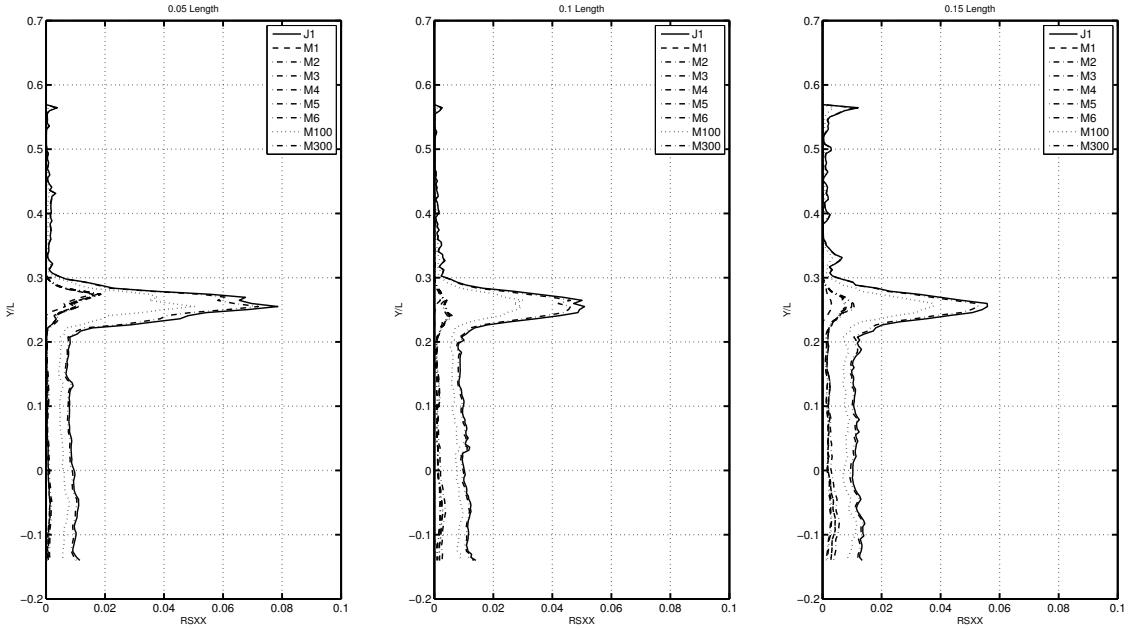

Figure 3.81: Jet1 mirror mean POD reconstructed $\frac{\overline{u'u'}}{U^2}$ Reynolds Stress profiles in the vertical symmetry plane of the wake. V= 30 m/s Re = 2.55x10^5.

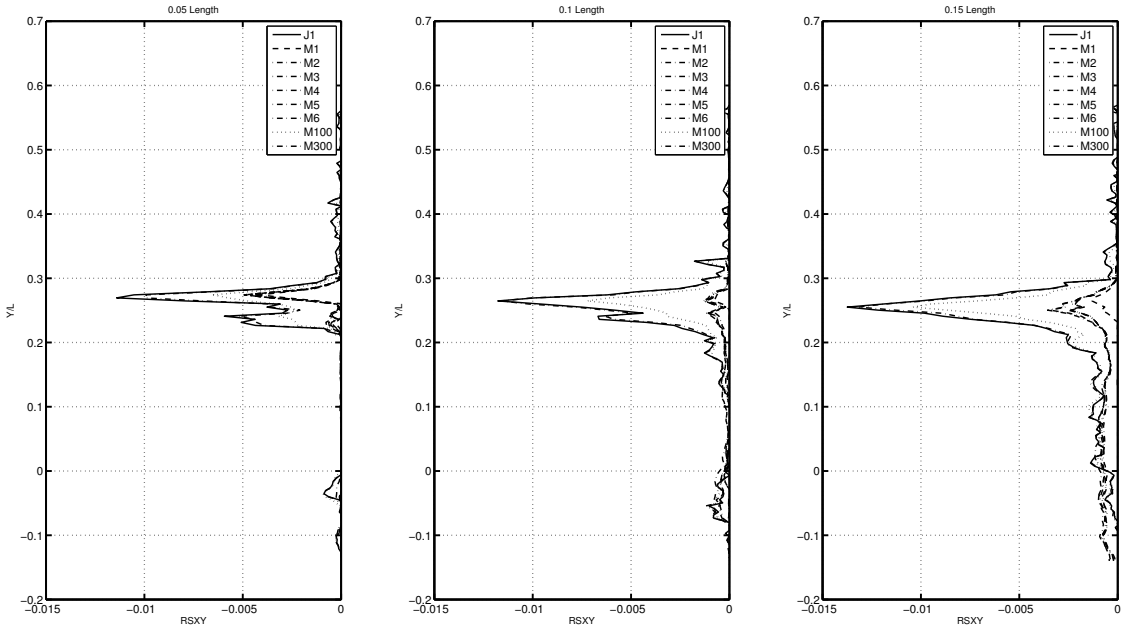

Figure 3.82: Jet1 mirror mean POD reconstructed $\frac{\overline{u'v'}}{U^2}$ Reynolds Stress profiles in the vertical symmetry plane of the wake. V= 30 m/s Re = 2.55x10^5.

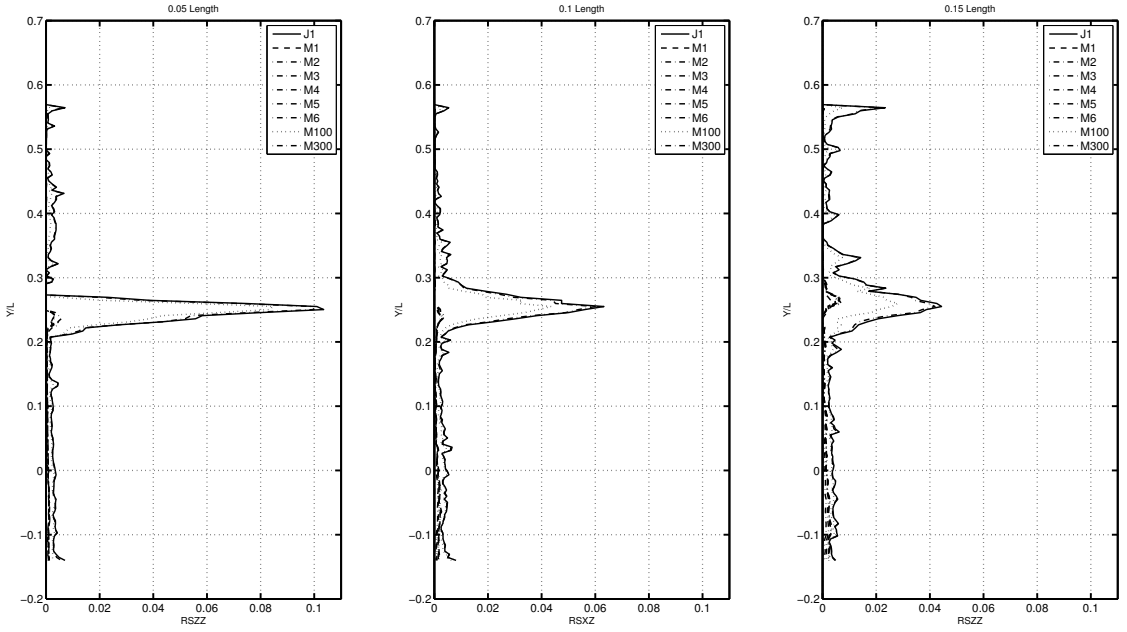

Figure 3.83: Jet1 mirror mean POD reconstructed $\frac{\overline{u'w'}}{U^2}$ Reynolds Stress profiles in the vertical symmetry plane of the wake. V= 30 m/s Re = 2.55x10^5.

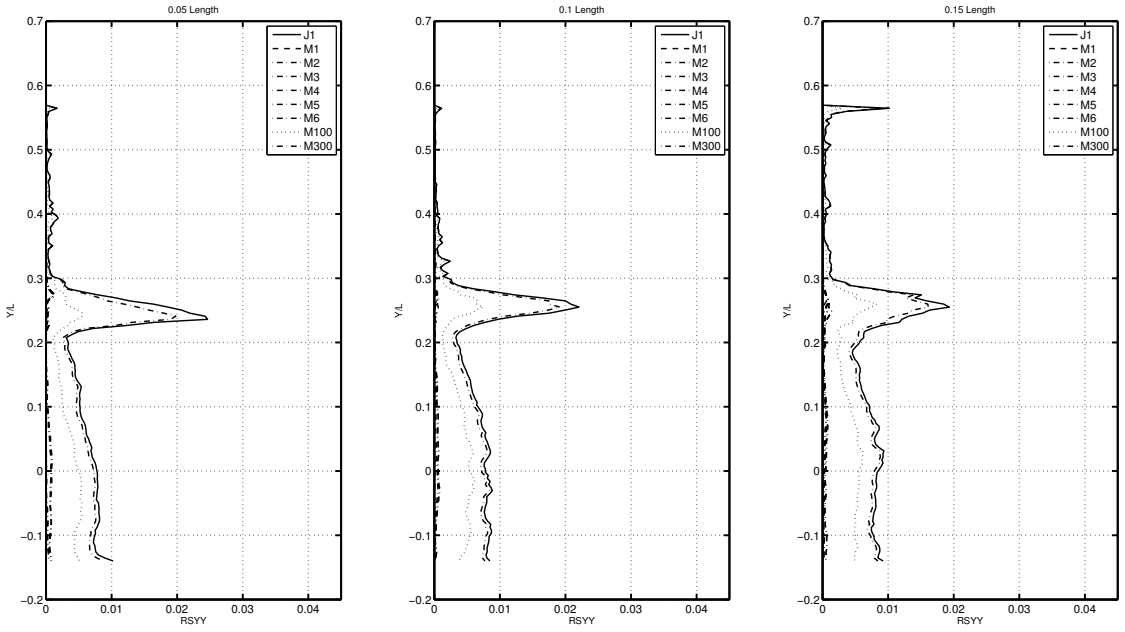

Figure 3.84: Jet1 mirror mean POD reconstructed $\frac{\overline{v'v'}}{U^2}$ Reynolds Stress profiles in the vertical symmetry plane of the wake. V= 30 m/s Re = 2.55x10^5.

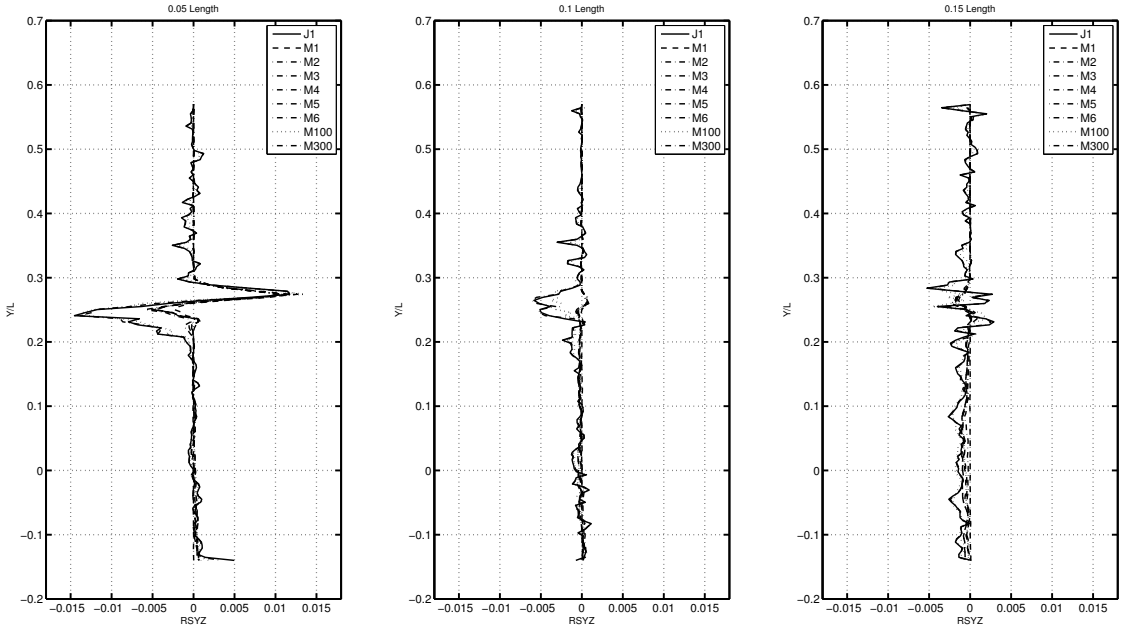

Figure 3.85: Jet1 mirror mean POD reconstructed $\frac{\overline{v'w'}}{U^2}$ Reynolds Stress profiles in the vertical symmetry plane of the wake. profiles. V= 30 m/s Re = 2.55x10^5.

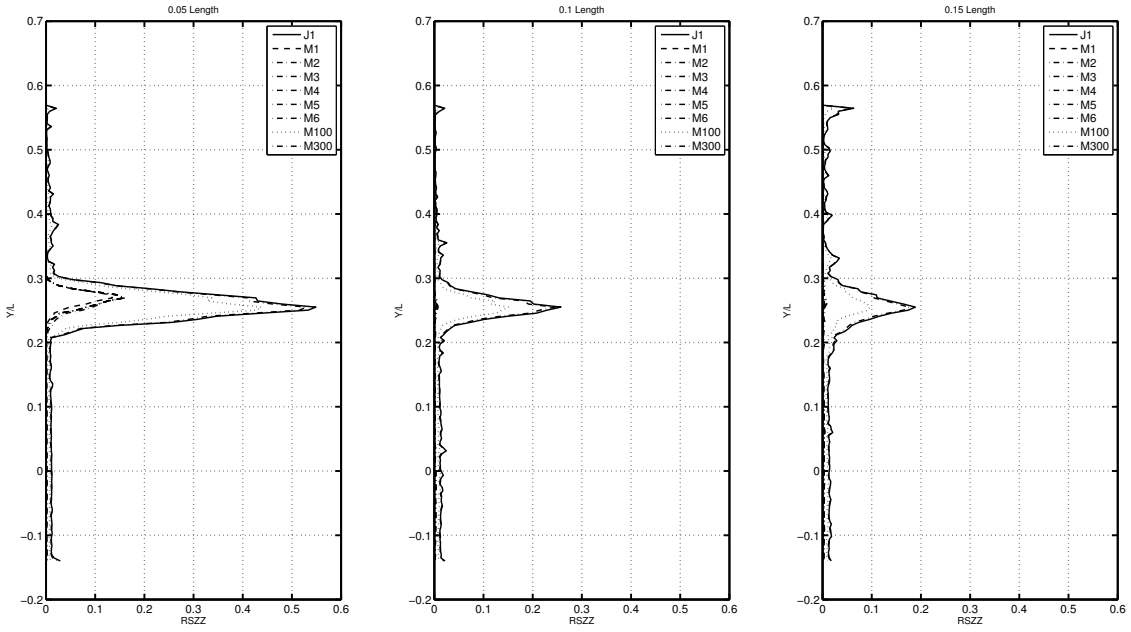

Figure 3.86: Jet1 mirror mean POD reconstructed $\frac{\overline{w'w'}}{U^2}$ Reynolds Stress profiles in the vertical symmetry plane of the wake. V= 30 m/s Re = 2.55x10^5.

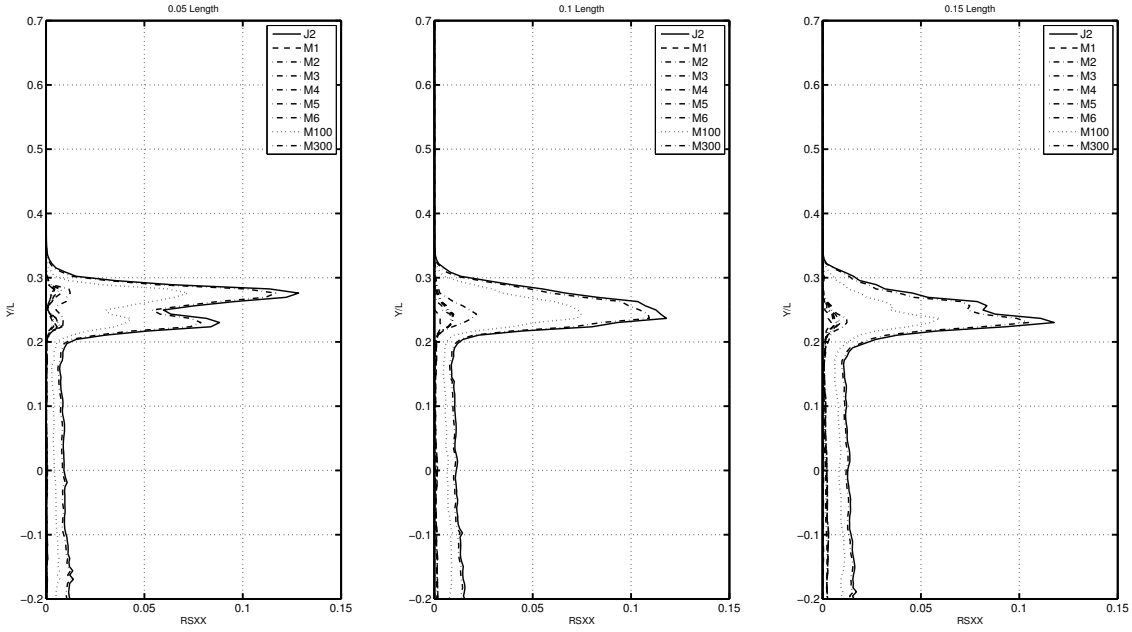

Figure 3.87: Jet2 mirror mean POD reconstructed $\frac{\overline{u'u'}}{U^2}$ Reynolds Stress profiles in the vertical symmetry plane of the wake. V= 30 m/s Re = 2.55x10^5.

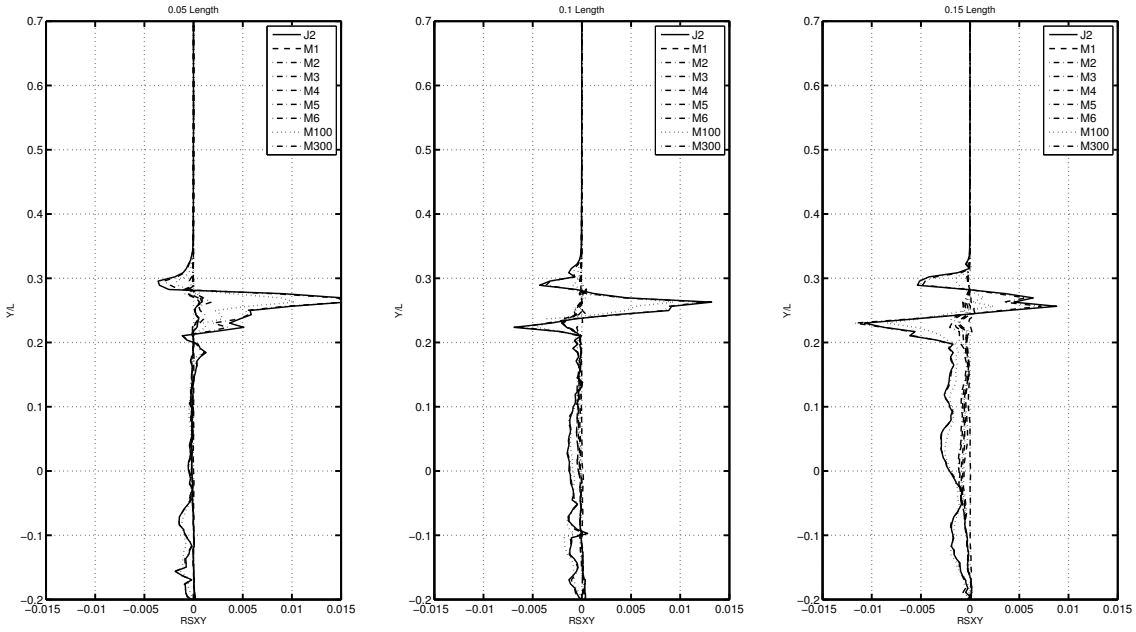

Figure 3.88: Jet2 mirror mean POD reconstructed $\frac{\overline{u'v'}}{U^2}$ Reynolds Stress profiles in the vertical symmetry plane of the wake. V= 30 m/s Re = 2.55x10^5.

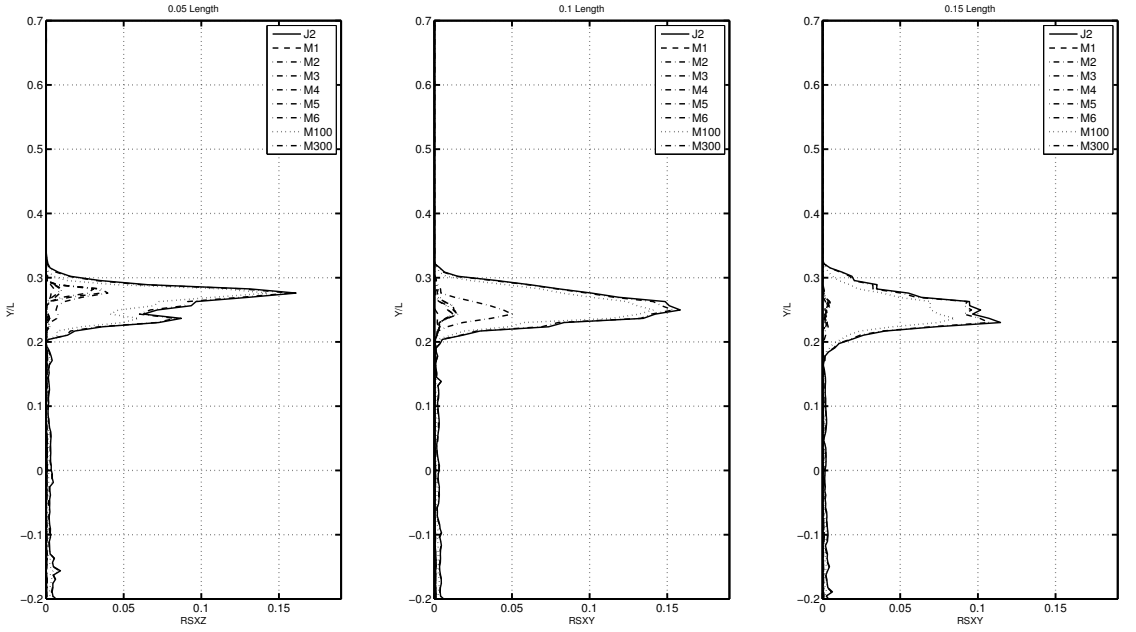

Figure 3.89: Jet2 mirror mean POD reconstructed $\frac{\overline{u'w'}}{U^2}$ Reynolds Stress profiles in the vertical symmetry plane of the wake. V= 30 m/s Re = 2.55x10^5.

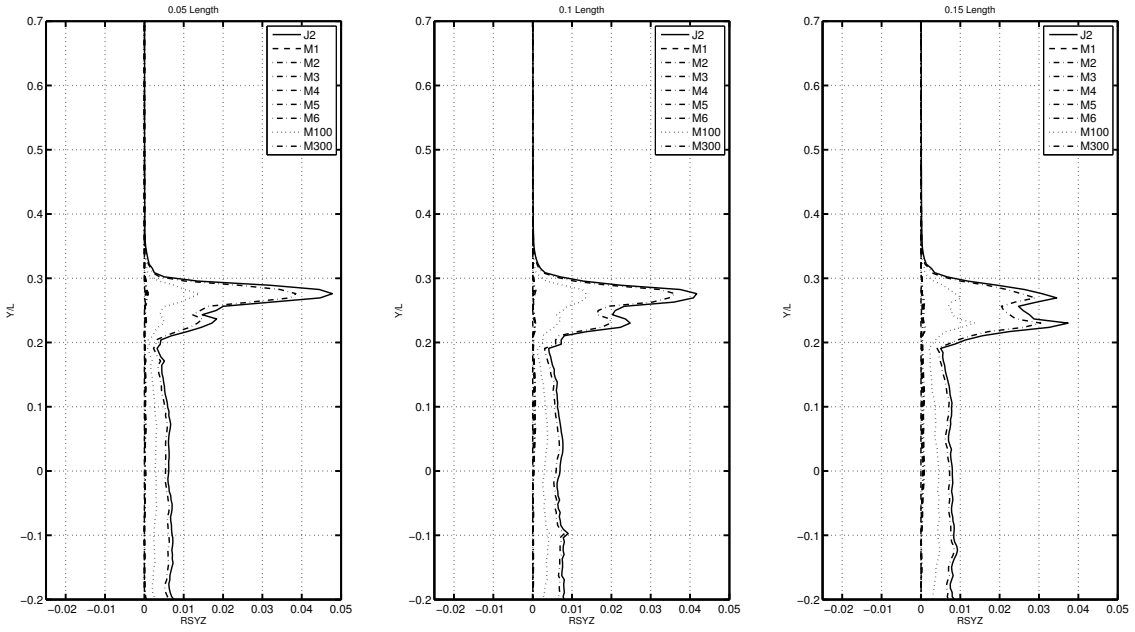

Figure 3.90: Jet2 mirror mean POD reconstructed $\frac{\overline{v'v'}}{U^2}$ Reynolds Stress profiles in the vertical symmetry plane of the wake. V= 30 m/s Re = 2.55x10^5.

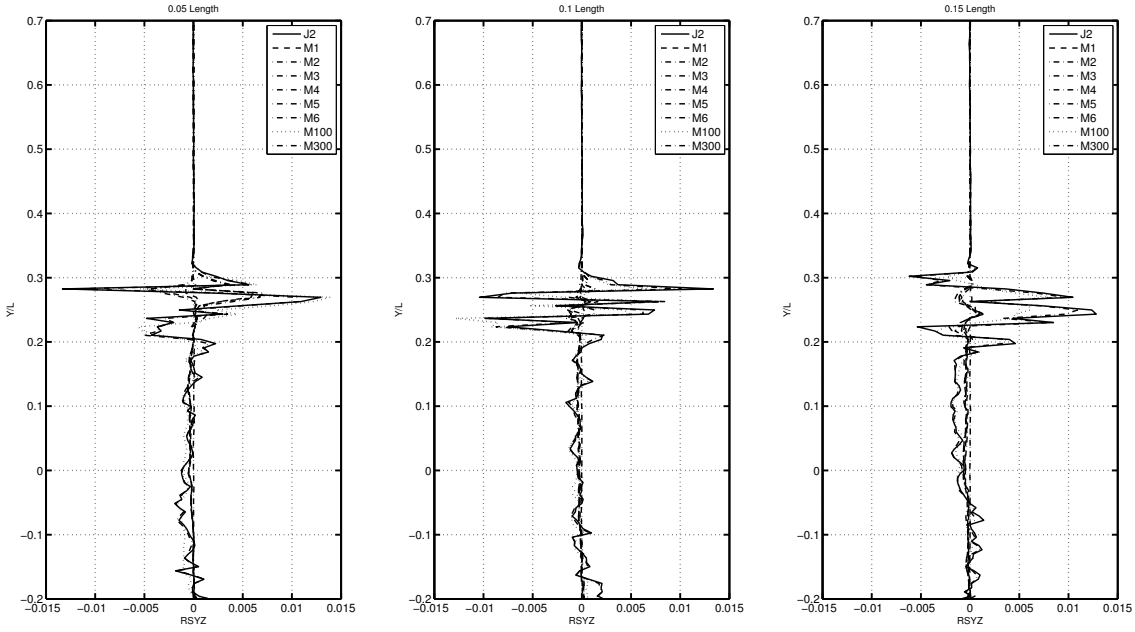

Figure 3.91: Jet2 mirror mean POD reconstructed $\frac{\overline{v'w'}}{U^2}$ Reynolds Stress profiles in the vertical symmetry plane of the wake. V= 30 m/s Re = 2.55x10^5.

.

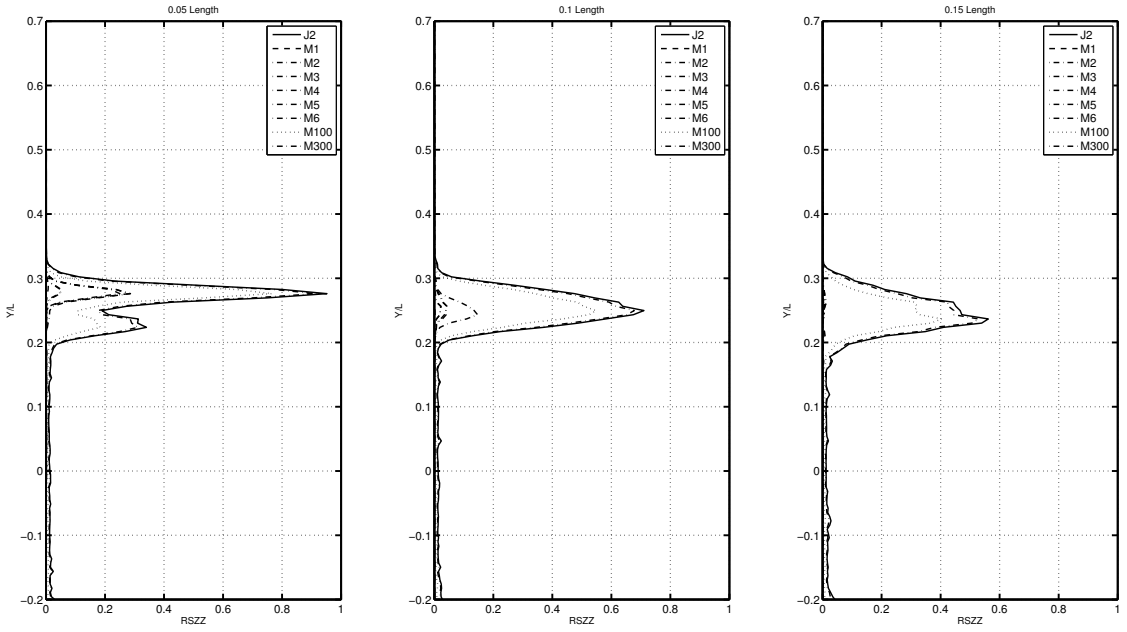

Figure 3.92: Jet2 mirror mean POD reconstructed $\frac{\overline{w'w'}}{U^2}$ Reynolds Stress profiles in the vertical symmetry plane of the wake. V= 30 m/s Re = 2.55x10^5.

Chapter 4

Conclusion

This research analyzed the effects of implementing passive flow control on an automotive mobile mirror in an effort to reduce of the inherent aerodynamic drag of the baseline model. The performance of the three models tested were examined using Particle Image Velocimetry in order to non-intrusively investigate the properties of the surrounding fluid. Through the implementation of the circumferential passive jet, flow separation at the trailing edge of the mirror model was reduced as the free shear layer remained attached further downstream towards the trailing edge of the passive jet models. Additionally, observed in place of the separation of the free shear layer was an immediate contraction by the wake in the recirculation region of the mirror. Although both mirror models have distinct differences in their passive jet design, results from the performance of the Jet1 model suggest that having a small circumferential slot can produce similar wake area reductions to that observed by the performance of the Jet2 model. This is believed to be due the enhanced entrainment initiated from the jet mixing that occurs close the trailing edge of the Jet1 mirror. Evidence of this was observed in the increased thickness of the mixing layer and in the coherent structures created with the free stream shear layer. Additional indications of the increased mixing efficiency of the Jet1 model can be observed in the POD analysis in which the data suggests both the Jet1 and Jet2 models can be seen to reduce the energy captured at 50 modes when compared to the baseline model by approximately 2%. This indicates a

higher order and more complex flow structure in the immediate wake region associated with the design the JBT mirror designs. The flow control methods demonstrated in this study were able to display improvements in the reduction of the recirculation region for both models in addition to the recirculation region velocity and energy distribution captured by the spatial eigenmodes. Applying these aerodynamic gains to automotive geometries susceptible to similar flow conditions could reduce overall fuel consumption associated with numerous automotive applications. Utilizing the aerodynamic enhancements associated with the passive flow control design, the augmented mirror model has the potential to greatly reduce the consumption of valuable resources and increase fleet fuel economy across multiple platforms.

References

[1] W. H. Hucho. “Areodynamics of Road Vehicles.” Annual Reviews Fluid Mechanics, vol. 25, pp.485-537, 1993.

[2] Al-Garni, A.M, “Fundamental Investigations of Road Vehicle Aerodynamics” Ph.D. thesis, Aerospace Engineering, University of Michigan, Ann Arbor, 2003.

[3] Ha, J., Jeong,S., Obayashi,S., “Drag Reduction of a Pickup Truck by a Rear Downward Flap” International Journal of Automotive Technology 12(3):369-374, 2011, doi:10.1007/s12239-011-0043-7.

[4] Beaudoin, J.F., Aider, J.L., “Drag and Lift reduction of a 3D Bluff Body Using Flaps.” Experimental Fluids, 44:491-501, 2008, doi 10.10007/s00348-007-0392-1.

[5] Tovey, M., “Design for Transport: A User-Centered Approach to Vehicle Design and Travel” Ashgate Publishing Ltd, Vermont, ISBN 9781409433255, 2012.

[6] U.S. Energy Information Administration, “Annual Energy Outlook 2014 with projections to 2040.” http://www.eia.gov/forecasts/aeo/MT_transportation.cfm #transp_declines?src=Consumption-b1, May 2014.

[7] Environmental Protection Agency, Department of Transportation. National Highway Traffic Saftey Administration. “Light-Duty Vehicle Greenhouse Gas Emissions Standards and Corporate Average Fuel Economy Standards.” Federal Register, Vol. 75, No 88, May. 2010.

[8] White House.gov, **“**Opportunity For All: Improving the Fuel Efficiency of American Trucks – Bolstering Energy Security, Cutting Carbon Pollution, Saving Money and Supporting Manufacturing Innovation,” http://www.whitehouse.gov/the-press-office/2014/02/18/fact-sheet-opportunity-all-improving-fuel-efficiency-american-trucks-bol, Feb. 2014.

[9] Anderson,J.D., “Fundamentals of Aerodynamics,” McGraw-Hill, Boston, ISBN 0-07-339810-1, 2001.

[10] Roshko, A. “Perspectives on Bluff Body Aerodynamics.” Journal of Wind Engineering and Industrial Aerodynamics” (49):79-100, 1993.

[11] Wilcox, D.C., "Basic Fluid Mechanics," DCW Industries Inc., California, ISDN1-928729-03-7, 2003.

[12] Kozlov, A.V., "Plasma Actuators for Bluff Body Flow Control," Ph.D. thesis, Aerospace and Mechanical Engineering Department, University of Notre Dame, Notre Dame, 2000.

[13] Zha, G.C., Paxton, C. "A Novel Airfoil Circulation Augment Flow Control Method Using Co-Flow Jet", AIAA 2208, 2004.

[14] Kirk, D., "Experimental and Numerical Investigations of a High Performance Co-Flow Jet Airfoil," Masters Thesis, Mechanical Engineering Department, University of Miami, Coral Gables, 2009.

[15] G.-C. Zha and D. C. Paxton, "A Novel Flow Control Method for Airfoil Performance Enhancement Using Co-Flow Jet." Applications of Circulation Control Technologies, Chapter 10, p. 293-314, Vol.214, Progress in Astronautics and Aeronautics, AIAA Book Series, Editors: Joslin, R. D. andJones, G.S., 2006.

[16] Adrian, R.J., and Westerweel, J., "Particle Image Velocimetry," Cambridge University Press, 2011, New York,NY.

[17] International Towing Tank Conference Recommended Procedures and Guidelines, "Uncertainty Analysis Particle Imaging Velocimetry," Sept. 2008.

[18] Wu, J.Z., Ma, H.Y., Zhou, M.D., "Vorticity and Vortex Dynamics," Springer, 2006, Berlin.

[19] Zha, G.-C., "Low Noise and Low Drag Automobile Mirrors Using Jet Flow Control", UMM-115, University of Miami Invention Disclosure, Sept. 7,2012.ref.

[20] Zha, G.-C., "Low Noise Low Drag Automobile Mirrors," *Provisional Patent filed to USPTO,61/765,219, 02/15/2013*.

[21] Zha, G.-C., "Low Drag Low Noise Automobile Mirrors Using Jet Flow Control," *Patent Coorperation Treaty, PCT/US2013/053191, filed to USPTO, 08/01/2013*, 2013.

[22] Wang, J., Bartow, W., Moreyra, A., Woyczynski, G. et al., "Low Drag Automotive Mirrors Using Passive Jet Flow Control," *SAE Int. J. Passeng. Cars - Mech. Syst.* 7(2):2014, doi:10.4271/2014-01-0584.